Detailed Balance Modeling of Monochromatic Photovoltaic Power Conversion

By

Daixi Xia

Thesis submitted to the
University of Ottawa
In partial fulfillment of the requirements
for the degree of
Master of Science in Physics

Ottawa-Carleton Institute of Physics
Department of Physics
University of Ottawa

Abstract

I present detailed balance modeling of photonic power converters, which are photovoltaic devices designed to convert monochromatic light. The detailed balance formalism is standard in finding limiting efficiencies of photovoltaic devices. In this thesis, I discuss both existing theories and original work. I start by discussing optical processes in semiconductors. I reproduce a monochromatic detailed balance model by Martin A. Green, which has stated that monochromatic photovoltaic energy conversion is 100% efficient at infinite input intensity with input photon energy matched to the absorption bandgap. I discuss effects that are not included in this standard model and the existing theories to treat these effects: (1) non-radiative recombination loss, (2) luminescent coupling in multi-layer devices, and (3) light trapping. These background materials are followed by original work, which is divided into three chapters. In these chapters, I present extensions of Green's theory to (1) a single-layer model that includes the effect of incomplete absorption, non-radiative recombination and input photon energy offset from absorption bandgap, and (2) a multi-layer model that includes luminescent coupling and light trapping effects, in addition to the effects already included in the single-layer extension. I show material quality and efficiency improvement predicted for a record-efficiency GaAs PPC. I also predict efficiency for a InAlGaAs device under development that targets conversion at telecommunication wavelength of 1310 nm.

Acknowledgment

I would like to thank my thesis supervisor, Prof. Jacob J. Krich, for his generous support and guidance throughout this study. Jacob has been extremely patient and understanding, and has given me plenty of valuable advices on both research-general and project-specific topics. Throughout the course of my study, I have greatly appreciated the opportunities provided by Jacob to attend and present at international conferences, for which, Jacob has spent a lot of time with me on polishing the slides and honing my presentation skills. Jacob has taught me - almost from scratch - the vital skills of scientific communication, from presentations to manuscript writing. I have, since the start of this degree, learned a great amount from Jacob on not only physics, but also research in general.

I would also like to extend my gratitude to Prof. Karin Hinzer, Dr. Christopher E. Valdivia and Dr. Mathew M. Wilkins, who have been extremely supportive and have taught me a great deal on photovoltaics. I would like to thank Meghan N. Beattie for many helpful and inspiring conversations. Meghan has been very generous in sharing experimental information with me. I would like to thank all colleagues in the project of PowerCom.

I would like to thank my colleagues and friends in the Krich group and SUNLAB, as well as in the Advanced Research Complex for all the personal and research-related support. I have enjoyed my Masters study because of the time spent with them.

At last, I very much thank my parents for their continuous support.

Statement of Original Contributions

In this thesis, Chapters 1 to 4 provide background materials and discuss previous theories, while Chapters 5 to 7 are original contributions to the field. Chapters 5 and 7 are conference proceedings, and Chapter 6 is a manuscript submitted to *Journal of Applied Physics*. Here I specify my contribution to each of these articles. In all cases, I am the main author, I developed the models and performed the calculations.

Chapter 5 models a GaAs photonic power converter using detailed balance formalism and predicts material quality and possible efficiency improvement of the record-setting device. Jacob J. Krich initiated the theoretical work and provided guidance. I did the detailed balance modeling. The device mentioned in the article was designed and fabricated by coauthors. I generated all figures, except for Figure 5.2.1, which was generated by Mathew M. Wilkins. Sanmeet S. Chahal calculated the series resistance loss of the device. The text was written by me; Jacob J. Krich and other coauthors provided editings. It is published as: D. Xia, M. M. Wilkins, S. S. Chahal, C. E. Valdivia, K. Hinzer, and J. J. Krich, "Opportunities for Increased Efficiency in Monochromatic Photovoltaic Light Conversion", in 2018 IEEE 7th World Conference on Photovoltaic Energy Conversion (WCPEC), 2018, pp. 3688--3692.

Chapter 6 discusses a multi-layer detailed balance model and provides an example of applying the model to multi-layer photonic power converters. Jacob J. Krich initiated the work and provided guidance. I developed the model and generated the results. All text and figures were generated by me. Jacob J. Krich provided editings.

Chapter 7 uses the model, which is discussed in Chapter 6, to predict the efficiency of multi-layer InAlGaAs photonic power converters. Jacob J. Krich initiated the theoretical work and provided guidance. I developed the model and generated the modeling results. Meghan N. Beattie did the ellipsometry and quantum efficiency measurements of the sample and generated Figure 7.2.2. The sample is designed and fabricated by coauthors. I generated all text and figures, except for Figure 7.2.2. Jacob J. Krich and coauthors provided editings. The article is published as: D. Xia, M. N. Beattie, M. C. Tam, M. M. Wilkins, C. E. Valdivia, Z. R. Wasilewski, K. Hinzer, and J. J. Krich, “Opportunities for High Efficiency Monochromatic Photovoltaic Power Conversion at 1310 nm,” in 2019 IEEE 46th

Photovoltaic Specialists Conference (PVSC), 2019, pp. 2303–2306.

To my mother

Contents

Chapter 1

Introduction

1.1 Monochromatic Photovoltaic Devices: Photonic Power Converters

A photonic power converter (PPC) is a photovoltaic (PV) device that converts monochromatic light into electricity. A PPC is an important component in an optical power transmission system. Such a system can deliver power in the form of light either through free space or in an optical fiber. The source of the power supply is narrow-band and can be a laser or an LED. At the receiving end of this power delivery system, a PPC converts photonic energy to electricity to supply power for an electronic element. An optical power transmission system allows power and bidirectional data transmission in one single optical fiber [1]. Power delivery in the form of light is intrinsically immune to electromagnetic noise, is spark-free and can be wireless. On top of that, one can boost the output voltage using a laser-PPC arrangement, instead of a DC-DC converter. Reference [2] showed that this boost-mode power supply is also ripple free [2].

PPCs have potential applications in a wide range of industries, such as utility, telecommunication, automotive, aerospace, biomedical engineering, etc., thanks to the many benefits of optical power transmission. Reference [1] demonstrated an optical network, in which remote subscriber operation does not require a local power supply. References [3], [4] and [5] demonstrated a current probe using photonic power conversion for monitoring high-voltage transmission lines. On the other hand, fuel gauges in an aircraft and sensors in an electric vehicle benefit from an optical power supply, because this power source is electromagnetically isolated and prevents sparks and shorts that could appear in conventional copper wiring [3]. Besides, a biomedical implant can use a photonic power source, thanks to the combined advantages of immunity to electromagnetic disturbance and capability of wireless

Table 1.1: State-of-the-art PPC devices

Reference	Efficiency (%)	Input Wavelength (nm)	Absorbing Material	Number of Segments	Interconnection Type	Voltage (V)	Light Intensity (W/cm^2)	Year
[11]	55	820	GaAs	6	horizontal	$V_{oc} = 6.7$	250 mW/ (unknown area)	1996
[10]	50.1	810	GaAs	2×2	hybrid	$V_{mp} = 4.11$	51.6	2009
[10]	55.1	810	GaAs	2×2	hybrid	$V_{mp} = 4.03$	8.5	2009
[9]	70	830	GaAs	5	vertical	$V_{mp} > 5$	8	2016
[12]	60.3	850	GaAs	20	vertical	$V_{mp} > 23$	36	2016
[13]	56.3	809	GaAs	4	horizontal	$V_{oc} = 4.7$	2.4	2016
[14]	38.7	1550	GaSb	1	N/A	$V_{oc} \simeq 0.5$	11.5	2016
[15]	34.5	1064	GaInAsP	1	N/A	$V_{oc} \simeq 0.8$	9.8	2018
[16]	40	1064	InGaAs	1	N/A	$V_{oc} \simeq 0.8$	7	2017
[17]	40.7	1070	InAlGaAs	1	N/A	$V_{oc} = 0.8$	0.16	2016

charging [6, 7].

Now I summarize the common architecture and performance of the state-of-the-art PPCs. I list these devices in Table 1.1. Most devices are made of III-V materials, which appear in the highest-efficiency PV devices - both PPCs and solar cells. A device's target conversion wavelength dictates the choice of alloy composition of the absorbing material. Existing PPCs using GaAs as the absorbing material adopt an architecture, in which a number of segments, ranging from 4 to 20, are interconnected and fabricated on the same chip. This design is not limited to be used with GaAs. The multi-segment architecture enables high-voltage power supply using one single chip. The segments are arranged in three ways: monolithic interconnected modules (MIM) [8], vertically stacked segments [9], or in a hybrid of these two structures [10]. Figure 1.1.1a is the cross section of two segments on a MIM device. These segments in MIM are either rectangular and arranged in an array [8], or they are pie-shaped and arranged on a circular chip, which matches the shape of the laser beam [11]. Another architecture for series-connected segments is to vertically stack each segment, with each segment series connected by tunnel diodes, shown in Figure 1.1.1b. The world-record-efficiency PPC uses a 5-segment vertical stack design, achieving a power conversion efficiency of 70% [9].

The operation wavelength of the state-of-the-art devices ranges from 810 to 1550 nm. 6 out of the 10 devices in Table 1.1 are made of GaAs and operate at 810-850 nm. GaAs is one of the most well-studied and well-characterized materials among the choices for PV devices. In fact, the device in [9], which keeps the world-record efficiency, is made of GaAs.

There is a reason why other operation wavelengths using different materials are also of interests: the system efficiency of optical power delivery includes not only the efficiency of the PPC, but also the source efficiency and the transmission efficiency. The transmission efficiency of an optical fiber favours a longer wavelength, or lower photon energy, than what GaAs is able to convert. In telecommunication,

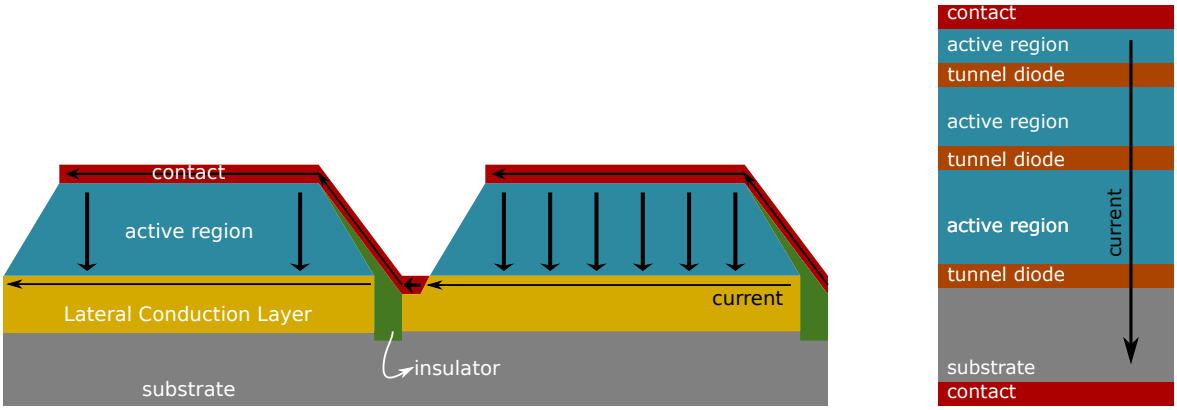

Figure 1.1.1: Schematics of (a) MIM and (b) vertical-stack devices (not to scale).

1310 nm and 1550 nm are the standard wavelengths for long-distance transmission[18]. For PPCs to be adopted in any application that requires the current telecommunication infrastructure, one must develop devices that convert efficiently at telecommunication wavelengths, hence the necessary research on designing and fabricating PPCs with other materials than GaAs, such as InGaAs, GaSb, InAlGaAs, etc..

The ability to integrate more than one segment on a chip is especially beneficial for telecom-wavelength devices, because the operating voltage of a single-junction device is limited by the bandgap of the absorbing material, which is in turn dictated by the operating wavelength. Hence, a longer-conversion wavelength results in lower per-segment voltage. A device targeting 1310 nm, for example, is limited to a voltage of less than 1 V per segment. For a device to output a usable voltage higher than this limit, one must adopt a multi-segment design. Current state-of-the-art PPCs that operate at a wavelength > 1 μm have only one segment. The lack of an existing multi-segment, telecom-wavelength device, which is optimized for monochromatic PV conversion, motivates a research project, PowerCom, with collaboration between the University of Ottawa and the University of Waterloo. This project aims to develop a high-efficiency, high-voltage, multi-segment device, using a quaternary alloy of InAlGaAs to operate at 1310 nm. This device will adopt the vertical-stack design similar to the world-record-efficiency device.

In 2001, Green showed that monochromatic PV conversion is 100% efficient at infinite input intensity [19] using a detailed balance model. However, this model does not include the real-world effects such as finite device thickness, non-radiative recombinaiton loss, and the offset between input photon energy and absorption bandgap. Futhermore, Green's model does not capture the low-current high-voltage characteristics of the vertical multi-segment design. The lack of a model that includes these effects has motivated the work presented in this thesis. Detailed balance modeling is standard in

benchmarking the performance of PV devices. A detailed-balance model that is able to describe the real-world device is needed for not only benchmarking purposes, but also future efficiency improvement strategies. In this thesis, I extend Green's model to include the important effects listed above and predict limiting efficiency in a set of device parameters and architectures.

1.2 Organization of Thesis

The thesis is divided into 7 Chapters. After the introduction, Chapter 2 discusses the photon absorption and emission process in semiconductor, and derive important results used in Chapter 3. Chapter 3 introduces the standard detailed balance theory for monochromatic PV conversion. This chapter provides information on Green's detailed balance theory for monochromatic conversion. Chapter 4 discusses effects that are not included in standard, single-layer detailed balance theory: non-radiative recombination loss, luminescent coupling, and light trapping. Chapter 5 is comprised of a conference proceeding, presented at the 7th World Conference On Photovoltaic Energy Conversion. In this chapter, I discuss the extension to Green's theory to include effects on input power density, non-radiative recombination, and offset between laser line and material absorption edge. This chapter also makes predictions for potential efficiency improvements and external radiative efficiency of the world-record-efficiency device in GaAs. Chapter 6 is a paper, which has been submitted to *Journal of Applied Physics*. In this chapter, I construct a detailed-balance-based theory to model vertically-stacked multi-segment photovoltaic devices. In Chapter 7, which is a conference proceeding, presented at the 46th IEEE Photovoltaic Specialists Conference, I discuss the potential efficiency achievable of the future InAlGaAs device, targeting operation at 1310 nm.

Chapter 2

Photon Absorption and Emission in Semiconductor

2.1 Microscopic Description of Optical Processes

In this section, I provide a microscopic description of optical processes, following the discussion in Reference [20]. The optical transition between valence and conduction band can be described by Fermi's Golden Rule. For the purpose of this discussion, we assume an isotropic medium. We consider the case, in which the perturbation is due to a plane wave with frequency ω, or equivalently, photon energy $E = \hbar\omega$. Consider an initial state $|i\rangle$ at energy E_i and a final state $|f\rangle$ at energy E_f. According to Fermi's Golden Rule, the probability of transition per unit time from a filled $|i\rangle$ state to an empty $|f\rangle$ state is

$$p_{i\to f} = \frac{2\pi}{\hbar}\left|\langle i|\,\hat{H}\,|f\rangle\right|^2 \delta\left(E_f - E_i - E\right) \tag{2.1.1}$$

where $\hat{H}$ is the perturbing Hamiltonian, representing the coupling between the initial and final state due to the optical field. The Dirac-Delta function ensures conservation of energy: the energy of the photon is converted into the energy of the electron. For simplicity of notation, we define the modulus square of matrix element as M:

$$M = \frac{2\pi}{\hbar}\left|\langle i|\,\hat{H}\,|f\rangle\right|^2 \tag{2.1.2}$$

By symmetry, the reverse process has the same matrix element:

$$\frac{2\pi}{\hbar}\left|\langle f|\,\hat{H}\,|i\rangle\right|^2 = \frac{2\pi}{\hbar}\left|\langle i|\,\hat{H}\,|f\rangle\right|^2 = M \tag{2.1.3}$$

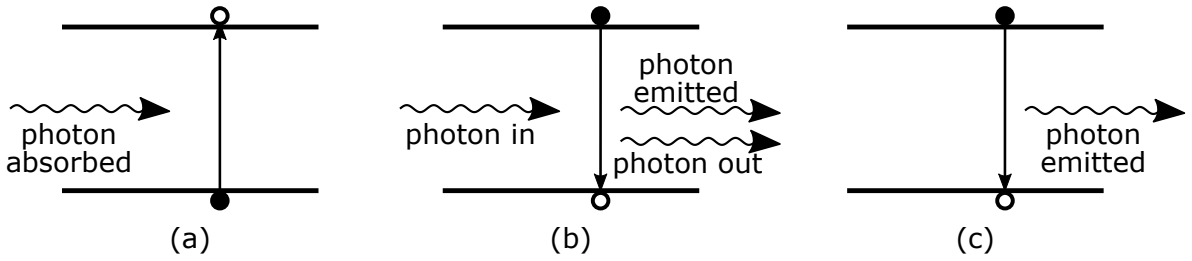

Figure 2.1.1: Transition of an electron between valence band and conduction band states: (a) absorption of a photon causes an electron to be excited from a valence band state to a conduction band state; (b) stimulated emission: a photon causes an electron in the conduction band to relax to the valence band and emit a photon; (c) spontaneous emission: an electron in the conduction band relaxes to the valence band while emitting a photon.

Three optical processes can occur, as demonstrated in Figure 2.1.1. Relating to electrons in a semiconductor, they are:

1. absorption of a photon promotes an electron from valence band to conduction band (absorption)
2. a photon stimulates an emission of a photon while an electron in the conduction band relaxes to the valence band (stimulated emission)
3. spontaneous emission of a photon when an electron in the conduction band relaxes to the valence band.

For Process 1, the rate is obtained from summing over the transition probability between all occupied valence band states with energy E_i and all empty conduction band states with energy E_f that is higher than E_i by E ; this sum is then weighted by the available density of photon states, $n_\gamma(E)$. In the continuous limit, we transform the sum into an integral. Then the rate of number of photons absorbed per time per volume per energy is:

$$r_{\text{abs}}(E) = n_\gamma(E) \int\int \mathrm{d}^3\vec{k}_i \mathrm{d}^3\vec{k}_f M g_v\left(\vec{k}_i\right) g_c\left(\vec{k}_f\right) f_v\left[E_i\left(\vec{k}_i\right)\right]\left\{1 - f_c\left[E_f\left(\vec{k}_f\right)\right]\right\}\delta\left(E_f - E_i - E\right) \tag{2.1.4}$$

where $g_v\left(\vec{k}_i\right)$ and $g_c\left(\vec{k}_f\right)$ are the density of states in the valence and conduction band, respectively; $f_v\left[E_i\left(\vec{k}_i\right)\right]$ and $f_c\left[E_f\left(\vec{k}_f\right)\right]$ are the Fermi probability in the valence and conduction band, respectively. Now we consider the case when the perturbing Hamiltonian causes a stimulated emission (Process 2). The rate of this transition is calculated by summing over all occupied states in conduction band and all empty states in valence band:

$$r_{\text{st}}(E) = n_\gamma(E) \int\int \mathrm{d}^3\vec{k}_i \mathrm{d}^3\vec{k}_f M g_v\left(\vec{k}_i\right) g_c\left(\vec{k}_f\right) f_c\left[E_i\left(\vec{k}_i\right)\right]\left\{1 - f_v\left[E_f\left(\vec{k}_f\right)\right]\right\}\delta\left(E_f - E_i - E\right) \tag{2.1.5}$$

Since a photon interacting with the system can lead to either Process 1 or Process 2, the net absorption rate r_{a} is the difference between the rate of Process 1 and Process 2:

$$\begin{aligned} r_{\mathrm{a}}(E) &= r_{\mathrm{abs}}(E) - r_{\mathrm{st}}(E) \\ r_{\mathrm{a}}(E) &= n_{\gamma}(E) \int\int \mathrm{d}^3\vec{k}_i \mathrm{d}^3\vec{k}_f M g_v\left(\vec{k}_i\right) g_c\left(\vec{k}_f\right) \left\{ f_v\left[E_i\left(\vec{k}_i\right)\right] - f_c\left[E_i\left(\vec{k}_i\right)\right] \right\} \delta\left(E_f - E_i - E\right) \end{aligned} \tag{2.1.6}$$

This expression for net absorption rate is later used to express absorption coefficient in Section 2.2. The probability of a spontaneous emission event (Process 3) is governed by the same set of density of occupied and unoccupied states as in stimulated emission. The rate of spontaneous emission is this probability multiplied by the density of states of photons in the medium of refractive index n:

$$r_{\mathrm{sp}}(E) = D_{\gamma}(E) \int\int \mathrm{d}^3\vec{k}_i \mathrm{d}^3\vec{k}_f M g_v\left(\vec{k}_i\right) g_c\left(\vec{k}_f\right) f_c\left[E_i\left(\vec{k}_i\right)\right] \left\{ 1 - f_v\left[E_i\left(\vec{k}_i\right)\right] \right\} \delta\left(E_f - E_i - E\right) \tag{2.1.7}$$

and

$$D_{\gamma}(E) = \frac{n^3 E^2}{\pi^2 \hbar^3 c^3}. \tag{2.1.8}$$

2.2 Beer-Lambert Absorption

Beer-Lambert law describes the attenuation of light intensity as it travels through a medium [20]. We consider a uniform medium and an optical field described by a superposition of plane waves; each plane wave has a frequency ω, or, equivalently, photon energy $E = \hbar\omega$. Due to linearity of the optical field, we can consider the intensity individually in each bin of energy E with bin width $\mathrm{d}E$. We assume that the wavelength is much smaller than the length scale of the medium. The Beer-Lambert law states that the attenuation of the intensity at energy E through a differential of the geometrical path length, $\mathrm{d}x$, is proportional to the intensity itself:

$$\mathrm{d}I(E,x) = -\alpha(E)\, I(E,x)\, \mathrm{d}x \tag{2.2.1}$$

The proportionality constant, α, is called the absorption coefficient. In general, α is a function of E. For the purpose of this thesis, our interest lies in the photon flux $\phi(E)$, which is related to intensity by:

$$\phi(E) = \frac{I(E)}{E} \tag{2.2.2}$$

ϕ is proportional to I, so ϕ is also described by the differential equation:

$$\mathrm{d}\phi\left(E,x\right)=-\alpha\left(E\right)\phi\left(E,x\right)\mathrm{d}x. \tag{2.2.3}$$

Solving this equation, we obtain the photon flux as a function of the geometrical path length x:

$$\phi\left(E,x\right)=\phi_0 e^{-\alpha(E)x}. \tag{2.2.4}$$

Here, ϕ_0 is the photon flux at $x=0$. The photons that are not transmitted are absorbed:

$$\phi_{\mathrm{abs}}\left(E,x\right)=\phi_0\left(1-e^{-\alpha(E)x}\right) \tag{2.2.5}$$

Hence, we define transmittance and absorbance:

$$\begin{aligned} t\left(E,x\right)&=e^{-\alpha(E)x}\\ a\left(E,x\right)&=1-t\left(E,x\right). \end{aligned} \tag{2.2.6}$$

Absorption coefficient is related to the complex refractive index $\tilde{n}$, defined as:

$$\tilde{n}=n+i\kappa. \tag{2.2.7}$$

According to basic electromagnetism theory, the absorption coefficient is [21]:

$$\alpha=\frac{2\omega}{c}\kappa. \tag{2.2.8}$$

where c is the speed of light. This relation between absorption coefficient and the complex part of the refractive index allows for experimental measurement of absorption coefficient using ellipsometry, which measures both the real and complex part of refractive index [22]. For the calculations that involve α in this work, I use experimentally measured values from either Reference [23] or ellipsometry experiments done by Meghan Beattie at the University of Ottawa.

Although, I use α as an empirical quantity in this thesis, I still give a theoretical description of α in a two-band pure crystal. This description is used to derive the emission rate under bias in Section 2.3.

Throughout this thesis, I neglect nonlinear effects. The two-photon absorption coefficients, β, for GaAs, InP, GaInAs, InAsP, and AlGaAs are on the order of 10 cm/GW [24, 25, 26]. In PPCs, the laser power density is $\lesssim 10^2$ W/cm^2. The linear absorption coefficient α is on the order of 10^4/cm. Therefore, we can ignore nonlinear absorptions in these materials in the context of PPCs.

According to Equation 2.2.1,

$$\alpha = -\frac{1}{I}\frac{\mathrm{d}I}{\mathrm{d}x} \tag{2.2.9}$$

For a plane wave, the intensity is related to the cycle-averaged power density using the wave velocity, v:

$$\begin{aligned} I &= \langle u \rangle v \\ &= \langle u \rangle \frac{c}{n} \end{aligned} \tag{2.2.10}$$

The intensity attenuation per distance is equal to the loss of cycle-averaged energy density per time:

$$\frac{\mathrm{d}I}{\mathrm{d}x} = \frac{\mathrm{d}\langle u \rangle}{\mathrm{d}t} \tag{2.2.11}$$

The loss of cycle-averaged energy density per time is equal to the rate of photon absorption multiplied by the energy of this photon:

$$\frac{\mathrm{d}\langle u \rangle}{\mathrm{d}t} = -E r_{\mathrm{a}}(E) \tag{2.2.12}$$

Combining Equations 2.2.102.2.92.2.11 and 2.2.12, we express the absorption coefficient as:

$$\alpha = \frac{n}{c}\frac{E r_{\mathrm{a}}(E)}{\langle u \rangle} \tag{2.2.13}$$

Energy density divided by photon energy gives the density of photons:

$$n_{\gamma}(E) = \frac{\langle u \rangle}{E} \tag{2.2.14}$$

Hence,

$$\alpha = \frac{n}{c}\frac{r_{\mathrm{a}}(E)}{n_{\gamma}(E)} \tag{2.2.15}$$

Substituting the expression for $r_{\mathrm{a}}(E)$ in Equation 2.1.6 to 2.2.15, we obtain a microscopic description for absorption coefficient:

$$\alpha(E) = \frac{n}{c}\int\int \mathrm{d}^3\vec{k}_i \mathrm{d}^3\vec{k}_f M g_v\left(\vec{k}_i\right) g_c\left(\vec{k}_f\right)\left\{f_v\left[E_i\left(\vec{k}_i\right)\right] - f_c\left[E_i\left(\vec{k}_i\right)\right]\right\}\delta\left(E_f - E_i - E\right) \tag{2.2.16}$$

In a pure crystal, the bandgap of the material, E_{g}, is defined as the smallest energy difference between a valence band state and a conduction band state. For all energy $E < E_{\mathrm{g}}$, no absorption or

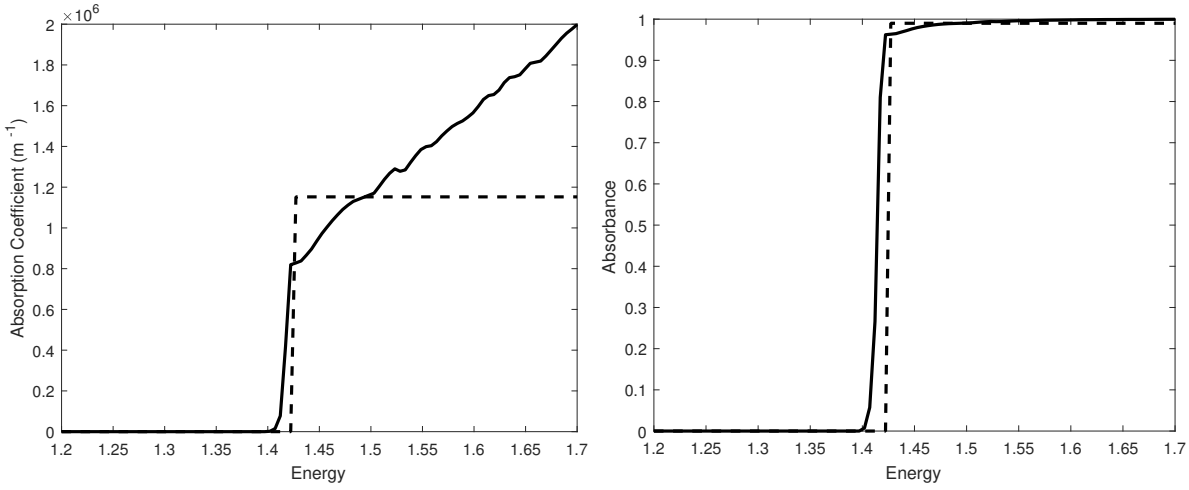

(a) (b)

Figure 2.2.1: (a) measured absorption coefficient of GaAs using data from Reference [23] (solid), and using an approximated step function (dashed). (b) Beer-Lambert absorbance with measured absorption coefficient (solid) and step-function absorption coefficient (dashed). The thickness is chosen so that, at $E = 1.494$ eV, the Beer-Lambert absorbance is 0.99.

emission occurs, and absorption coefficient is zero:

$$\alpha\left(E < E_{\mathrm{g}}\right) = 0 \tag{2.2.17}$$

In a direct bandgap semiconductor, where we conserve momentum in the optical transitions, the absorption coefficient rises as

$$\alpha_{\mathrm{d}}\left(E\right) \propto \left(E - E_{\mathrm{g}}\right)^{1/2}, \tag{2.2.18}$$

whereas in an indirect bandgap material, the absorption coefficient is

$$\alpha_{\mathrm{id}}\left(E\right) \propto \left(E - E_{g}\right)^{2}. \tag{2.2.19}$$

A two-band theory can only capture some features of the measured absorption coefficient. The solid line in Figure 2.2.1(a) is the measured absorption coefficient of GaAs, data obtained from Reference [23]. Emipirically, the bandgap is extracted in measured absorption coefficient by fitting the region of the measured data that is described by 2.2.18 and extrapolating the fit to obtain the energy where the fitted absorption coefficient is zero. This energy is then defined as E_{g}.

It is common to approximate absorption coefficient as a Heaviside step function of energy in detailed balance calculations, which are discussed in Chapter 3. Now I demonstrate the difference in absorbance using measured $\alpha\left(E\right)$ and the step-function approximation. In Figure 2.2.1(a), I plot $\alpha\left(E\right)$ of GaAs as a function E, obtained from Reference [23] and with step function approximation choosing a value of α

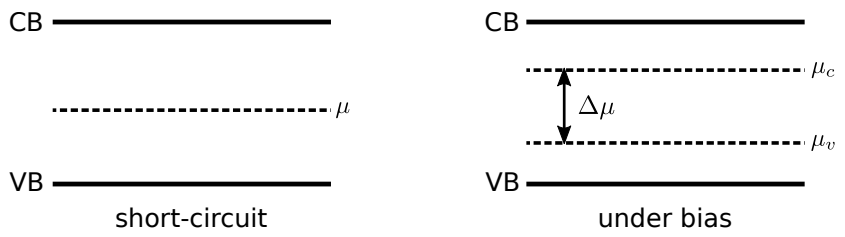

Figure 2.3.1: Energy diagrams for electrons in the valence and conduction band (VB and CB). At short circuit, the device is not under bias, and there is only one Fermi level for the valence and conduction band. Under bias, each band has a different quasi-Fermi level. The difference in quasi-Fermi level equals the applied voltage, when the carriers have infinite mobility.

above bandgap equal to the measured α at $E = 1.494$ eV. In Figure 2.2.1(b), I plot the corresponding absorbance using both measured α and step-function approximation. In both cases, I choose a thickness so the absorbance at $E = 1.494$ eV is 0.99. The step-function approximation of absorption coefficient is useful in some models because of its simplicity. In Chapter 5, I use two types of $\alpha(E)$: (i) from Reference [23], and (ii) step-function absorbance. We see in Figure 5.3.3 that the device efficiency predicted with these two $\alpha(E)$ does not differ much from each other. This small difference justifies using step-function $\alpha(E)$ in Chapter 6 and 7.

2.3 Spontaneous Emission Under Bias

In this section, I derive the rate of spontaneous emission $r_{\mathrm{sp}}(E)$ in a semiconductor under bias in dark, i.e., with no external optical input. I follow the derivation in Reference [27]. When the system is under bias, the conduction band electrons and the valence band holes are not in thermal equilibrium with each other. However, we assume that the inter-band transitions are much slower than intra-band transitions. Therefore, in steady state, the carriers in each band are in equilibrium with the carriers in the same band. We call this state quasi-equilibrium [23]. In this quasi-equilibrium, the Fermi levels of valence and conduction band separate, as demonstrated in Figure 2.3.1. These Fermi levels are called quasi-Fermi levels. We define μ_v and μ_c as the quasi-Fermi level of valence band and conduction band, respectively. Then the occupation probability of electrons in each band according to Fermi-Dirac statistics is

$$f_v(\epsilon) = \frac{1}{e^{(\epsilon-\mu_v)/kT}+1} \tag{2.3.1a}$$

$$f_c(\epsilon) = \frac{1}{e^{(\epsilon-\mu_c)/kT}+1} \tag{2.3.1b}$$

where k is Boltzmann constant, and T is the temperature. For simplicity of notation, we define the density of occupied and unoccupied states in valence and conduction band:

$$n_o^{v,c}(\epsilon) = D_{v,c}(\epsilon) f_{v,c}(\epsilon) \tag{2.3.2a}$$

$$n_u^{v,c}(\epsilon) = D_{v,c}(\epsilon) [1 - f_{v,c}(\epsilon)], \tag{2.3.2b}$$

where $D_{v,c}$ are the density of states of valence and conduction band.

At equilibrium, the detailed balance condition requires that the rate of net absorption is equal to the rate of spontaneous emission at every E:

$$r_{\mathrm{sp}}(E) = r_{\mathrm{a}}(E) = r_{\mathrm{abs}}(E) - r_{\mathrm{st}}(E). \tag{2.3.3}$$

Using the definition of absorption coefficient in terms of $r_{\mathrm{a}}(E)$ in Equation 2.2.15. The rate of spontaneous emission is:

$$r_{\mathrm{sp}}(E) = \alpha \frac{c}{n} n_\gamma(E). \tag{2.3.4}$$

Hence, in order to calculate $r_{\mathrm{sp}}(E)$, we need to obtain an expression for $n_\gamma(E)$, which is the photon density in the medium at equilibrium. Recall from Section 2.2 that the rates of absorption, stimulated emission and spontaneous emission are:

$$\begin{aligned} r_{\mathrm{abs}}(E) &= n_\gamma(E) \int \mathrm{d}E_i M n_o^v(E_i) n_u^c(E_i + E) \\ r_{\mathrm{st}}(E) &= n_\gamma(E) \int \mathrm{d}E_i M n_u^v(E_i) n_o^c(E_i + E) \\ r_{\mathrm{sp}}(E) &= D_\gamma(E) \int \mathrm{d}E_i M n_u^v(E_i) n_o^c(E_i + E) \end{aligned}$$

The density of photon states in a cavity, $D_\gamma(E)$, is discussed previously, in Equation 2.1.8. We obtain an expression for $n_\gamma(E)$ in terms of $D_\gamma(E)$ by substituting Equation (2.3.5) into the detailed balance condition in Equation2.3.3:

$$n_\gamma(E) \int \mathrm{d}E_i M n_o^v(E_i) n_u^c(E_i + E) - n_\gamma(E) \int \mathrm{d}E_i M n_u^v(E_i) n_o^c(E_i + E) = D_\gamma(E) \int \mathrm{d}E_i M n_o^v(E_i) n_u^c(E_i + E) \tag{2.3.6}$$

Isolating $n_\gamma(E)$, we get

$$n_\gamma(E) = \frac{D_\gamma(E) \int \mathrm{d}E_i M n_u^v(E_i) n_o^c(E_i + E)}{\int \mathrm{d}E_i M n_u^v(E_i) n_o^c(E_i + E) \left[\frac{n_o^v(E_i) n_u^c(E_i + E)}{n_u^v(E_i) n_o^c(E_i + E)} - 1 \right]}. \tag{2.3.7}$$

We can simplify the quantity inside the square bracket on the denominator of Equation 2.3.7 us-

ing Equations (2.3.1) and (2.3.2) :

$$\frac{n_o^v\left(E_i\right)n_u^c\left(E_i+E\right)}{n_u^v\left(E_i\right)n_o^c\left(E_i+E\right)}-1=e^{(E-\mu)/kT}-1 \tag{2.3.8}$$

where μ is the difference between conduction and valence band quasi-Fermi levels:

$$\mu=\mu_c-\mu_v. \tag{2.3.9}$$

When carriers have infinite mobility, this quasi-Fermi level splitting is related to the applied voltage across the semiconductor by elementary charge q:

$$\mu=qV. \tag{2.3.10}$$

The quantity inside the square bracket on the denominator of Equation 2.3.7 does not depend on the integration variable E_i, so we can cancel out the integrals on the numerator and the denominator. Then, Equation 2.3.7 becomes:

$$n_\gamma\left(E\right)=\frac{D_\gamma\left(E\right)}{e^{(E-\mu)/kT}-1}. \tag{2.3.11}$$

Substituting the expression for the density of states of photons in Equation 2.1.8 into Equation 2.3.11, we obtain the explicit expression for $n_\gamma\left(E\right)$:

$$n_\gamma\left(E\right)=\frac{8\pi n^3}{h^3c^3}\frac{E^2}{e^{(E-\mu)/kT}-1}. \tag{2.3.12}$$

Substituting this expression of $n_\gamma\left(E\right)$ into Equation 2.3.4, we arrive at an expression for spontaneous emission rate in terms of μ and α:

$$r_{\mathrm{sp}}\left(E\right)=\alpha n^2\frac{8\pi}{h^3c^2}\frac{E^2}{e^{(E-\mu)/kT}-1}. \tag{2.3.13}$$

With the assumptions in this derivation, the emission is isotropic in all angles. Then we can divide $r_{\mathrm{sp}}\left(E\right)$ by the solid angle of an entire sphere to obtain the emission rate per solid angle, in the dimension of number per volume per time per energy per solid angle:

$$S\left(E\right)=\frac{r_{\mathrm{sp}}\left(E\right)}{4\pi}=\alpha n^2\frac{2}{h^3c^2}\frac{E^2}{e^{(E-\mu)/kT}-1}. \tag{2.3.14}$$

The importance of this result is that, if we take α and n as empirical values, the emission rate only depends on the applied voltage of the device, and does not depend on the band structure or the individual quasi-Fermi Levels.

2.4 Generalized Planck Spectrum

In this section, I follow Reference [27] to discuss a generalized Kirchhoff's Law of non-thermal radiation, which gives an expression for an energy-resolved photon flux emitted out of a slab under bias. This concept is an important part of the detailed balance theory for PV devices, discussed in Chapter 3. Consider a slab of material with infinite area and finite thickness of L, as shown in Figure 2.4.1. The slab has a refractive index of n. On both sides of the slab is air, with a refractive index of n_e. We first derive the solid-angle-integrated photon current density inside this slab in the x-direction, which is the direction normal to the surface of the slab. We consider $x = 0$ on one side of the slab and $x = L$ on the other side. We define θ as the angle between the direction of photon propagation and $\hat{x}$ inside the slab. The system is isotropic in the azimuthal angle, φ. From Equation 2.3.14, we have the knowledge of the rate of photon emission per solid angle:

$$S(E) = \frac{r_{sp}(E)}{4\pi}. \tag{2.4.1}$$

As shown in Figure 2.4.1, we consider photon current density at energy E and location x, $j_\gamma(E, x)$, traveling in the $\hat{x}$-direction. This photon current is due to internal radiation. We start by considering radiation due to a differential volume $\mathrm{d}V = \mathrm{d}A\mathrm{d}x$ inside the slab. $\mathrm{d}A$ is the surface parallel to the surface of the slab. Spontaneous emission from $\mathrm{d}V$ contributes to the photon current at an amount of

$$\mathrm{d}\Omega \mathrm{d}A_0 \mathrm{d}x \frac{r_{sp}(E)}{4\pi} \tag{2.4.2}$$

where $\mathrm{d}\Omega = \sin\theta \mathrm{d}\theta \mathrm{d}\varphi$ is the solid angle. According to Lambert's Cosine Law, the effective area of emission $\mathrm{d}A_0$ at an angle of θ is weighted by $\cos\theta$ as:

$$\mathrm{d}A_0 = \mathrm{d}A\cos\theta \tag{2.4.3}$$

This cosine weighting is to ensure that the number of photons emitted from this area per solid angle is the same in all θ. We integrate Equation 2.4.2 over the solid angle of the hemisphere facing x-direction. Then we divide the result with $\mathrm{d}A$ to obtain the contribution to photon current density due

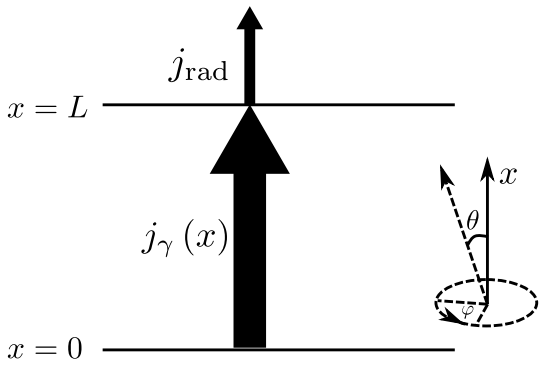

Figure 2.4.1: A slab of material in dark. $\hat{x}$ is the direction normal to the surface of the slab. θ is the angle between the direction of propagation and $\hat{x}$ inside the slab. φ is the azimuthal angle. $j_\gamma(x)$ is the solid-angle-integrated photon current density in the direction of $\hat{x}$ and j_{rad} is the photon current density emitted out of the device.

to spontaneous emission in $\mathrm{d}V$:

$$\begin{aligned}
\mathrm{d}j_\gamma^{\mathrm{sp}}(E,x) &= \int_{\mathrm{hemisphere}} \cos\theta \mathrm{d}\Omega \mathrm{d}x \frac{r_{\mathrm{sp}}(E)}{4\pi} \\
\mathrm{d}j_\gamma^{\mathrm{sp}}(E,x) &= 2\pi \int_0^{\pi/2} \cos\theta \sin\theta \mathrm{d}\theta \mathrm{d}x \frac{r_{\mathrm{sp}}(E)}{4\pi} \\
\frac{\mathrm{d}j_\gamma^{\mathrm{sp}}(E,x)}{\mathrm{d}x} &= \frac{1}{4} r_{\mathrm{sp}}(E)
\end{aligned}$$

Other than contributing to photon current, the differential volume $\mathrm{d}V$ also absorbs photon at a rate of $r_{\mathrm{a}}(E)$. We know from Equation 2.2.15:

$$r_{\mathrm{a}}(E,x) = \alpha(E) j_\gamma(E,x)$$

Therefore, the loss of photon current density due to absorption in $\mathrm{d}V$ is

$$\frac{\mathrm{d}j_\gamma^{\mathrm{a}}(E,x)}{\mathrm{d}x} = -\alpha j_\gamma(E,x) \tag{2.4.4}$$

The continuity equation of $j_\gamma(E)$ is then:

$$\begin{aligned}
\frac{\mathrm{d}j_\gamma(E,x)}{\mathrm{d}x} &= \frac{\mathrm{d}j_\gamma^{\mathrm{sp}}(E,x)}{\mathrm{d}x} + \frac{\mathrm{d}j_\gamma^{\mathrm{a}}(E,x)}{\mathrm{d}x} \\
\frac{\mathrm{d}j_\gamma(E,x)}{\mathrm{d}x} &= \frac{1}{4} r_{\mathrm{sp}}(E) - \alpha(E) j_\gamma(E,x)
\end{aligned} \tag{2.4.5}$$

It is necessary to know the initial condition to solve Equation 2.4.5. The initial condition depends on the the internal reflectance at the left and the right surface. We define the internal reflectance at both surface to be R'. Using symmetry, the initial condition is $j_\gamma(E,0) = R' j_\gamma(E,L)$. With this

initial condition, the solution to Equation 2.4.5 is:

$$j_\gamma(E,x) = \frac{r_{\mathrm{sp}}(E)}{4\alpha(E)} \frac{1 - e^{-\alpha(E)x} - R'\left(e^{-\alpha L} - e^{\alpha x}\right)}{1 - R'e^{-\alpha(E)L}}. \tag{2.4.6}$$

Evaluating at $x = L$, we obtain:

$$j_\gamma(E,L) = \frac{r_{\mathrm{sp}}(E)}{4\alpha(E)} \frac{1 - e^{-\alpha(E)L}}{1 - R'e^{-\alpha(E)L}}. \tag{2.4.7}$$

Out of all photons reaching the right surface, only $(1 - R')$ of them are transmitted to the outside. Here we define external transmittance, $(1 - R)$, which describes photon transmission from the external into the slab. The internal transmittance is related to the external transmittance by the refractive index contrast:

$$(1 - R') = \frac{n_e^2}{n^2}(1 - R) \tag{2.4.8}$$

where n_e is the refractive index of the external and n is the refractive index of the slab. Combining Equations (2.3.13), (2.4.7) and (2.4.8), the photon current density emitted to the outside of the slab is:

$$j_{\mathrm{rad}}(E) = a(E) \frac{2\pi}{h^3c^2} \frac{E^2}{e^{(E-\mu)/kT} - 1} \tag{2.4.9}$$

where the absorbance is defined as:

$$a(E) = \frac{(1 - R)\left(1 - e^{-\alpha(E)L}\right)}{1 - R'e^{-\alpha(E)L}} \tag{2.4.10}$$

Note that at $\mu = 0$, i.e., when the device is not under bias, then we recover the Planck spectrum for black body radiation. Therefore, Equation 2.4.9 is called the generalized Planck spectrum. This result allows us to obtain the photon emission rate from the surface of a slab of material, without needing to take care of the internal details. This convenience is then exploited in detailed balance theories for PV, as discussed in Chapters 3 and 5. Sometimes, the internal structures are of concerns, then one uses the local emission rate in Equation 2.3.14 and model the internal structure separately, for example in Reference [28]. Chapters 6 and 7 use this approach.

Chapter 3

Detailed Balance Theory of Monochromatic PV Conversion

The detailed balance formalism allows calculation of the limiting efficiency of PV devices. The theory was first developed by Shockley and Quisser for solar cells [29]. This chapter discusses an analogous formalism for monochromatic PV conversion. This monochromatic theory was developed by Green [19]. I follow Green's derivation in this chapter for an expression for efficiency using dimensionless, figure-of-merit-like quantities. In Reference [19], the author gives an expression of limiting efficiency in the case of a Dirac-Delta absorbance at the bandgap. The author claims that with both Delta absorbance and step-function absorbance, the efficiency is 100% when the incident intensity approaches infinity. Step-function absorption is a more general case and is used in the extension of Reference [19], in Chapter 5. Therefore, in this chapter, I give derivations only with step-function absorbance, and verify the claim in Reference [19] that the limiting efficiency is indeed 100%.

3.1 Detailed Balance Condition

The detailed balance condition states that the rate of carriers extracted per area is equal to the rate of carriers created per area minus the rate of carriers lost per area:

$$J = J_{\text{in}} - J_{\text{loss}} \tag{3.1.1}$$

We assume that one photon excites only one electron-hole pair, and one electron-hole pair recombines to produce only one photon. In principle, recombination event can be radiative or non-radiative. In this chapter, we assume all recombination is radiative. In Chapter 4.1, we discuss a method to incorporate

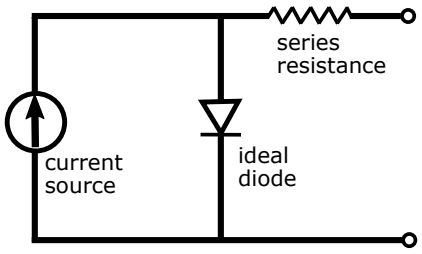

Figure 3.2.1: One-diode equivalent circuit of a photovoltaic device.

non-radiative effects. We further assume that all carriers have infinite mobility leading to spatially uniform quasi-Fermi level splitting throughout the device. With these assumptions and conditions, we can relate current density and photon fluxes using Equation 3.1.1. In particular, collected current density is equal to the photon flux absorbed in the device minus the photon flux emitted out of the device:

$$\frac{J}{q} = \dot{N}_{\text{abs}} - \dot{N}_{\text{out}} \tag{3.1.2}$$

where q is the elementary charge. Both the absorption and emission of photon flux depends on the absorbance of the device. The number of photons that enter the cell is the sum of the incident photon flux from the narrow-band source, $\dot{n}\left(E\right)$, and thermal radiation from the ambient at room temperature, $\dot{n}_{\text{amb}}\left(E\right)$. So the number of photons absorbed in the cell is

$$\dot{N}_{\text{abs}} = \int_{E_{\text{g}}}^{\infty} \mathrm{d}E \int_{0}^{2\pi} \mathrm{d}\varphi \int_{0}^{\pi/2} \sin\theta\cos\theta \mathrm{d}\theta \left(\dot{n}\left(E\right) + \dot{n}_{\text{amb}}\left(E\right)\right) \tag{3.1.3}$$

We assume that the ambient shares the same temperature as the cell, and it follows the black body spectrum, i.e.,

$$\dot{n}_{\text{amb}} = \frac{2}{h^3c^2} \frac{E^2}{e^{E/kT} - 1} \tag{3.1.4}$$

We know $\dot{N}_{\text{out}}$ from Equation 2.4.9. Hence, the current density is:

$$\frac{J\left(V\right)}{q} = \int_{E_{\text{g}}}^{\infty} \mathrm{d}E \int_{0}^{2\pi} \mathrm{d}\varphi \int_{0}^{\pi/2} \sin\theta\cos\theta \mathrm{d}\theta \left[\dot{n}\left(E\right) + \frac{2}{h^3c^2} \frac{E^2}{e^{E/kT} - 1} - \frac{2}{h^3c^2} \frac{E^2}{e^{(E-qV)/kT} - 1}\right] a\left(E\right) \tag{3.1.5}$$

where $a\left(E\right)$ is the absorbance. By integrating $\mathrm{d}E$ from E_{g} to infinity, we assume no sub-bandgap absorption, i.e., $a\left(E\right) = 0$ for all $E < E_{\text{g}}$.

3.2 Boltzmann Approximation

Under Boltzmann approximation, Equation 3.1.5 gives the ideal diode equation. At room temperature, $kT \simeq 0.025$ eV, and in common PV materials, $E_{\text{g}} \simeq 1$ eV, so $E_{\text{g}} \gg kT$. In Equation 3.1.5, since we

integrate energy from E_g to infinity, the second term is then approximately:

$$\frac{2}{h^3c^2}\frac{E^2}{e^{E/kT}-1} \simeq \frac{2}{h^3c^2}\frac{E^2}{e^{E/kT}}. \tag{3.2.1}$$

Similarly, in the case where the operating voltage is well below the bandgap, i.e., $E_g - qV \gg kT$, the third term becomes:

$$\frac{2}{h^3c^2}\frac{E^2}{e^{(E-qV)/kT}-1} = \frac{2}{h^3c^2}\frac{E^2}{e^{E/kT}}e^{qV/kT}. \tag{3.2.2}$$

Hence, Equation 3.1.5 can be written as:

$$J(V) = J_{in} - J_0\left(e^{qV/kT}-1\right) \tag{3.2.3}$$

where we define the reverse-saturation current J_0 as

$$J_0 = \frac{2}{h^3c^2}\int_{E_g}^{\infty}\frac{a(E)\,E^2\mathrm{d}E}{e^{E/kT}}. \tag{3.2.4}$$

For a device in dark, i.e., $J_{in} = 0$, Equation 3.1.5 recovers the ideal-diode equation. We can consider the current-voltage characteristics of a PV device in an equivalent circuit, as demonstrated in Figure 3.1.5. J_{in} is the equivalent current source, while the PV device acts as a diode. In fact, it is common to use the ideality factor, n_d, for the diode equation to better describe the device. With n_d, the dark current is:

$$J_{dark} = J_0\left(e^{qn_dV/kT}-1\right). \tag{3.2.5}$$

An ideal diode has an ideality factor of $n_d = 1$. It is also common to use more than one diodes with different n_d for describing voltage-dependent effects.

The equivalent-circuit model is not accurate when $E_g - qV$ is comparable to kT. In this case, we have to work in the full degenerate limit as in Equation 3.1.5. As shown in Section 3.3, the optimal operating voltage increases as the incident flux increases. Hence, the full detailed balance formalism in the degenerate case is needed at high input intensity.

3.3 Limiting Efficiency of Monochromatic Conversion

In this section, we work in the opposite limit of Boltzmann approximation. For large incident flux from the source, the photon flux due to thermo-radiation from the ambient at room temperature is negligible. Then we can omit the second term in Equation 3.1.5, and the detailed balance condition

becomes:

$$\frac{J(V)}{q} = \int_{E_g}^{\infty} \mathrm{d}E \int_0^{2\pi} \mathrm{d}\varphi \int_0^{\pi/2} \sin\theta\cos\theta \mathrm{d}\theta \left[\dot{n}(E) + \frac{2}{h^3c^2} \frac{E^2}{e^{(E-qV)/kT} - 1}\right] a(E) \tag{3.3.1}$$

The efficiency of the device can be written as a function of voltage:

$$\eta(V) = \frac{J(V)V}{\dot{N}E_s} \tag{3.3.2}$$

where we define the total incident flux:

$$\dot{N} = \int_{E_g}^{\infty} \mathrm{d}E \int_0^{2\pi} \mathrm{d}\varphi \int_0^{\pi/2} \sin\theta\cos\theta \mathrm{d}\theta \dot{n}(E). \tag{3.3.3}$$

Here, we work in the monochromatic limit, i.e., all incident photons have the same energy E_s. The current density $J(V)$ decreases with increasing V. Hence, there exists a maximum η with respect to V. The optimized voltage, V_{mp}, is commonly known as the voltage at maximum power.

We work in the scenario that gives the highest efficiency. We consider a slab of material with infinite thickness, so all incident photons with energy above the bandgap are absorbed, i.e., $a(E)$ is a Heaviside step function in energy. All absorbed photons that have an energy larger than E_g suffers from thermalization loss. Hence, for minimal loss, we require $E_s = E_g$. Furthermore, if the device can only emit into angles less than θ_r from the surface normal, the emission solid angle is:

$$\Delta\Omega = \int_0^{2\pi} \mathrm{d}\varphi \int_0^{\theta_r} \sin\theta\cos\theta \mathrm{d}\theta \tag{3.3.4}$$

The emission solid angle has a range of $\Delta\Omega \in [0, \pi]$. Any value smaller than π can be obtained using a concentrator. Under the above conditions, Equation 3.3.1 reduces to

$$\frac{J(V)}{q} = \dot{N} - \frac{2\Delta\Omega}{h^3c^2} \int_{E_g}^{\infty} \frac{E^2 \mathrm{d}E}{e^{(E-qV)/kT} - 1} \tag{3.3.5}$$

We can expand the Bose integral using polylogarithms to bracket the value of this integral [30]. Generally, we can expand a Bose-Einstein integral with a finite lower limit into $j+1$ terms. We consider the integral of the form:

$$I_j(\epsilon, \mu) = \frac{1}{\Gamma(j+1)} \int_{\epsilon}^{\infty} \frac{E^j \mathrm{d}E}{e^{E-\mu} - 1} \tag{3.3.6}$$

where $\Gamma(z)$ is the Gamma function, defined as:

$$\Gamma(z) = \int_0^{\infty} x^{z-1} e^x \mathrm{d}x. \tag{3.3.7}$$

We expand $I_j(\epsilon,\mu)$ in terms of $I_j(0,\mu-\epsilon)$, which, by definition, is the Bose integral with integration limit of 0 to infinity:

$$I_j(\epsilon,\mu)=\sum_{k=0}^{j}\frac{\epsilon^{j-k}}{(j-k)!}I_j(0,\mu-\epsilon). \tag{3.3.8}$$

For negative μ, $I_j(0,\mu)$ can be expanded in an infinite series, which converge to polylogarithm functions, $\mathrm{Li}_j(x)$:

$$I_j(0,\mu)=\mathrm{Li}_{j+1}(e^{\mu}) \tag{3.3.9}$$

where $\mathrm{Li}_j(x)$ are defined as:

$$\mathrm{Li}_j(x)=\sum_{k=1}^{\infty}\frac{x^k}{k^j}. \tag{3.3.10}$$

Combining Equations (3.3.6), (3.3.8) and (3.3.9), we have

$$I_j(\epsilon,\mu)=\sum_{k=0}^{j}\frac{\epsilon^{j-k}}{(j-k)!}\mathrm{Li}_{j+1}\left(e^{\mu-\epsilon}\right). \tag{3.3.11}$$

Here, we are interested in the second order, i.e., $j=2$. Using Equation 3.3.11, we pull out $\frac{\epsilon^2}{2}\mathrm{Li}_1(e^{\mu-\epsilon})$, and we have:

$$I_2(\epsilon,\mu)=\frac{\epsilon^2}{2}\mathrm{Li}_1\left(e^{\mu-\epsilon}\right)\left[1+\frac{2}{\epsilon}\frac{\mathrm{Li}_2(e^{\mu-\epsilon})}{\mathrm{Li}_1(e^{\mu-\epsilon})}+\frac{2}{\epsilon^2}\frac{\mathrm{Li}_2(e^{\mu-\epsilon})}{\mathrm{Li}_1(e^{\mu-\epsilon})}\right]. \tag{3.3.12}$$

We observe the following:

$$\mathrm{Li}_1\left(e^{\mu-\epsilon}\right)=\ln\left[\frac{1}{1-e^{\mu-\epsilon}}\right], \tag{3.3.13}$$

and for $\mu-\epsilon<0$,

$$0<\frac{\mathrm{Li}_2(e^{\mu-\epsilon})}{\mathrm{Li}_1(e^{\mu-\epsilon})}<1$$
$$0<\frac{\mathrm{Li}_3(e^{\mu-\epsilon})}{\mathrm{Li}_1(e^{\mu-\epsilon})}<1.$$

Therefore, we can define an f factor:

$$f=\left[1+\frac{2}{\epsilon}\frac{\mathrm{Li}_2(e^{\mu-\epsilon})}{\mathrm{Li}_1(e^{\mu-\epsilon})}+\frac{2}{\epsilon^2}\frac{\mathrm{Li}_2(e^{\mu-\epsilon})}{\mathrm{Li}_1(e^{\mu-\epsilon})}\right]. \tag{3.3.14}$$

f is constrained:

$$1\le f\le\left[1+\frac{2}{\epsilon}+\frac{2}{\epsilon^2}\right]. \tag{3.3.15}$$

Using this result, the second term in Equation 3.3.5 becomes:

$$\frac{2\Delta\Omega}{h^3c^2}\int_{E_g}^{\infty}\frac{E^2\mathrm{d}E}{e^{(E-qV)/kT}-1}=\frac{2\Delta\Omega}{h^3c^2}(kT)E_g^2\ln\left[\frac{1}{1-e^{(qV-E_g)/kT}}\right]f. \tag{3.3.16}$$

where we have $\epsilon = \frac{E_g}{kT}$. Since kT at room temperature is 0.024 eV, for semiconductors with bandgap $E_g \simeq 1$eV, f must be quite close to 1. We further define normalized intensity i and normalized voltage y:

$$i = \left(\frac{h^3c^2}{2}\right)\frac{\dot{N}}{E_g^2\Delta\Omega\,(kT)} \tag{3.3.17}$$

$$y = e^{(E_g - qV)/kT} - 1, \tag{3.3.18}$$

which are both dimensionless. Then, using Equations (3.3.2), (3.3.5) and (3.3.16) to (3.3.18), we obtain a compact expression for efficiency:

$$\eta = \left[1 - \frac{kT}{E_g}\ln\left(y+1\right)\right]\left[1 - \frac{f}{i}\ln\frac{y+1}{y}\right] \tag{3.3.19}$$

Following the strategy in Reference [19], I find the limiting efficiency by setting the derivative of $\eta\,(y)$ with respect to y to zero. Here, we consider the limit where the incident photon flux is very large. In this limit, and the optimum voltage is very close to the bandgap, i.e., $E - qV \ll kT$, which is equivalent to $y \ll 1$. We expand η and $\frac{\mathrm{d}\eta}{\mathrm{d}y}$ in Maclaurin series of y and keep only the first term. Then, the optimal η is

$$\eta_{\mathrm{mp}} = 1 - \frac{f}{i}\ln\left[\frac{kT}{E_g}W\left(\frac{E_g}{kT}e^{1+i/f}\right)\right] \tag{3.3.20}$$

where $W\,(z)$ is the Lambert W function, defined as

$$x = W\left(xe^x\right). \tag{3.3.21}$$

In the limit of $i \to \infty$, η_{mp} is 1.

This result indicates that the limiting efficiency for monochromatic energy conversion is 100%, and the efficiency only depends on the the normalized intensity i, when $E_s = E_g$, mobilities are infinite, and the device has no non-radiative recombination. As in Equation 3.3.17, reducing $\dot{N}$ is equivalent to increasing $\Delta\Omega$ by the same amount. Hence, an efficiency of 100% is achievable at infinite input intensity or at zero emission angle.

Note a few of assumptions we make to ensure maximum efficiency: (i) the energy of the incident photon aligns with the bandgap of the material, i.e., $E_s = E_g$, (ii) all recombination is radiative, and (iii) the device is infinitely thick so all incident photons are absorbed. None of these assumptions holds true in real devices. First of all, real devices suffer from non-radiative recombination loss. To study this loss, one can modify this detailed balance theory by including radiative efficiency. This technique is discussed in Chapter 4.1. In Chapter 5, which is an extension of this chapter, I will demonstrate the

effect of non-radiative reocombination loss on efficiency. Secondly, real devices are usually designed to absorb 98%-99% of the incident photons, which are at an energy slightly larger than the bandgap. This design principle is to limit device thickness, because absorption coefficient at the bandgap is smaller than that at energy larger than the bandgap, as demonstrated in Figure 2.2.1, so for the same device thickness, fewer photons with energy at the bandgap are absorbed compared to those with higher energy. The efficiency loss due to incomplete absorption is called transparency loss. On the other hand, all photons with $E_s > E_g$ suffer from thermalization loss. Therefore, there is a trade-off between transparency and thermalization loss. I study this trade-off in Chapter 5.

Chapter 4

Beyond Radiative Single-Layer Detailed Balance Theory

In this chapter, I discuss some of the important effects in PV that are not included in a radiative, single-layer detailed balance theory, as discussed in Chapter 3. I also discuss the existing methods for incorporating such effects into the theory.

4.1 Non-Radiative Recombination Loss

Non-radiative recombination loss constitutes a large part of efficiency loss in PV devices. The detailed balance theory discussed in Chapter 3 considers only loss due to radiative recombination. In this section, I discuss the strategy of using internal and external radiative efficiency in the detailed balance formalism.

We can modify Equation 3.1.2 to include carrier loss due to non-radiative recombination. The modified detailed balance condition is then:

$$\frac{J}{q} = \dot{N}_{\mathrm{abs}} - \dot{N}_{\mathrm{out}} - \dot{N}_{\mathrm{nr}}. \tag{4.1.1}$$

The first two terms are the same as in Equation 3.1.2, and $\dot{N}_{\mathrm{nr}}$ is the number of carriers lost due to non-radiative recombination per time per area. Note that $\dot{N}_{\mathrm{nr}}$ has the same dimension as the photon flux emitted out of the device, $\dot{N}_{\mathrm{out}}$. We know the functional form of $\dot{N}_{\mathrm{out}}$ in terms of voltage. To obtain information on $\dot{N}_{\mathrm{nr}}$, we have two options. The first option involves modeling the rate for each non-radiative recombination process. The second option is to use an experimentally-measurable quantity, external radiative efficiency, η_{ext}. For the purpose of a detailed-balance formalism, we use

the second approach to evaluate non-radiative loss. η_{ext} describes the ratio of the number of photons emitted out of the device to the number of all carriers lost:

$$\eta_{\text{ext}} = \frac{\dot{N}_{\text{out}}}{\dot{N}_{\text{out}} + \dot{N}_{\text{nr}}}. \tag{4.1.2}$$

Hence, Equation 4.1.1 can be rewritten as

$$\frac{J}{q} = \dot{N}_{\text{abs}} - \frac{1}{\eta_{\text{ext}}}\dot{N}_{\text{out}}. \tag{4.1.3}$$

With this expression, we can take η_{ext} as an independent parameter in a detailed-balance model, and proceed to calculate the maximum efficiency using the approach discussed in Chapter 3. In Chapter 5, I discuss this modification.

In principle, η_{ext} depends on both voltage and current density. However, it is common to treat η_{ext} as a voltage-independent material property. The value of η_{ext} is often measured at open-circuit [31]. Reference [31] reports the state-of-the-art η_{ext} values for solar cells. The best η_{ext} reported is over 20% for a GaAs cell.

η_{ext} gives a convenient way to evaluate open-circuit voltage drop due to non-radiative recombination loss. From Equation 2.4.9, recall that

$$\dot{N}_{\text{out}} = \frac{2}{h^3c^2}\int \mathrm{d}E \int \mathrm{d}\Omega \frac{a\left(E\right)E^2}{e^{(E-qV)/kT}-1} \tag{4.1.4}$$

Assuming $E \gg qV$, we use Boltzmann approximation and express $\dot{N}_{\text{out}}$ as

$$\dot{N}_{\text{out}} = J_0 e^{qV/kT} \tag{4.1.5}$$

where

$$J_0 = \frac{2}{h^3c^2}\int \mathrm{d}E \int \mathrm{d}\Omega a\left(E\right)E^2 e^{E/kT}. \tag{4.1.6}$$

With this definition, we rewrite Equation 4.1.3 as

$$\frac{J}{q} = \dot{N}_{\text{abs}} - \frac{1}{\eta_{\text{ext}}}J_0 e^{qV/kT}. \tag{4.1.7}$$

At open-circuit, $J = 0$, and we have

$$V_{\text{oc}} = V_{\text{oc}}^{\text{rad}} - \frac{kT}{q}\ln\frac{1}{\eta_{\text{ext}}} \tag{4.1.8}$$

where

$$V_{\mathrm{oc}}^{\mathrm{rad}} = \frac{kT}{q}\ln\frac{\dot{N}_{\mathrm{abs}}}{J_0} \tag{4.1.9}$$

is the open-circuit voltage in the radiative limit. We see from Equation 4.1.8 that V_{oc} decreases logarithmically with η_{ext}. Hence, η_{ext} gives a direct and simple way of quantifying material quality in a PV device.

However, η_{ext} does not only depend on material quality. Device geometry also determines the value of η_{ext}. I explain the reason after defining the internal radiative efficiency, which expresses the local probability of a radiative recombination occurring:

$$\eta_{\mathrm{int}} = \frac{r_{\mathrm{rad}}}{r_{\mathrm{rad}} + r_{\mathrm{nr}}} \tag{4.1.10}$$

where r_{rad} is the radiative recombination rate and r_{nr} is the non-radiative recombination rate. η_{int} only depends on material quality. In general, η_{int} can also depend on voltage and current-density, just like η_{ext} does. However, in the virtue of simplicity for detailed-balance theories, it is common to take η_{int} as an independent parameter. In the definition of η_{int}, at a given radiative-recombination rate, the total non-radiative recombination loss of current density scales as $\left(\frac{1}{\eta_{\mathrm{int}}} - 1\right) L$, where L is the thickness of the device.

Now we connect the concepts of η_{int} and η_{ext}. First, we consider the radiative limit where $\eta_{\mathrm{int}} = 1$ and the device has an ideal back reflector. In this case, we have to have $\eta_{\mathrm{ext}} = \eta_{\mathrm{int}} = 1$, because the current loss is equal to the number of photons emitted out of the cell. It is, however, possible that $\eta_{\mathrm{ext}} < 1$ even in the radiative limit. An example is a device with an absorbing substrate. All photons emitted into the substrate are loss. The number of photons emitted out of the cell from the top surface is therefore smaller than the current density loss. Hence, in this case, $\eta_{\mathrm{ext}} < 1$ even in the radiative limit. Now we consider the case with $\eta_{\mathrm{int}} < 1$. A photon emitted at one location inside a cell can be reabsorbed and reemitted many times before this photon reaches out of the cell. Every time the photon is reabsorbed, it has only a probability of η_{int} to be reemitted. The number of reabsorption and reemission events before the photon reaches out of the cell depends on the optical thickness as well as internal reflectivity of the device. Therefore, η_{int} is usually many times larger than η_{ext} [31]. Hence, we conclude that while η_{int} only depends on material quality, η_{ext} depends on both material quality and device geometry. Reference [28] describes an η_{int}-to-η_{ext} mapping using a statistical ray-optic method, that is able to consider device geometry.

The value of using η_{int} instead of η_{ext} is precisely because η_{int} is independent of device geometry. Hence, we are free to devise a model that incorporates a specific device geometry into our detailed-balance theory. This freedom is especially important when we consider a multi-layer device where

internally emitted photons are emitted and reabsorberd in different layers, and hence contributing to current loss or current gains in different layers. The challenges regarding a multi-layer detailed-balance model is discussed in Section 4.2. I use η_{ext} in Chapter 5, where η_{ext} is sufficient in a single-layer model. In Chapters 6 and 7, which involve multi-layer modeling, I use η_{int}.

4.2 Luminescent Coupling in Multi-Layer PV

Luminescent coupling (LC) arises in series-connected multi-layer devices. A multi-layer device is made up of vertically stacked layers, and each layer is typically a pn junction. These layers are series connected by tunnel diodes, which behave like ohmic contacts between the layers. Ideal tunnel diodes are transparent to both incident and internally emitted photons. In a multi-layer device, each layer obeys the detailed balance condition, similarly to the single-layer case as in Equation 3.1.1. The difference is that a layer in a multi-layer stack not only absorbs photons from the external incidence, but also absorbs photons from other layers, as demonstrated in Figure 4.2.1. This effect of reabsorbing photons at a layer different to where the photons are emitted is called LC. With LC, the detailed balance condition in layer i is

$$J_i = J_i^{\text{in}} - J_i^{\text{loss}} + \sum_j J_{ij}^{\text{lc}} \tag{4.2.1}$$

where J_i is the current density extracted, J_i^{in} is the incident photon flux density that are absorbed in layer i, and J_{ij}^{lc} is the LC flux density from layer j to layer i. When the layers are series connected, the current density extracted from each layer has to be equal:

$$J_i = J \quad \forall i. \tag{4.2.2}$$

Each layer's optimum operating voltage is determined by the absorbed photon flux density, which includes both J_i^{in} and J_{ij}^{lc}, where J_{ij}^{lc} is determined by the voltage of other layers. With the constraint of current matching, we therefore consider that the voltages of all layers are coupled through internal luminescence, hence we have the name, luminescent coupling.

The effect of LC is first observed as an "artifact" in quantum efficiency measurements in multi-layer solar cells [32, 33, 34, 35]. Besides, Reference [36] identifies signatures of LC in fill factor measurements at varying bias light intensities for each subcell. The presence of LC indicates that radiative recombination dominates over non-radiative recombination loss. Hence, one can gain insights to material quality by quantifying the LC effects.

There are many benefits related to LC. Reference [37] shows that LC can improve efficiency of solar cells by a significant amount, with optimized thickness of each layer. It has also been demonstrated

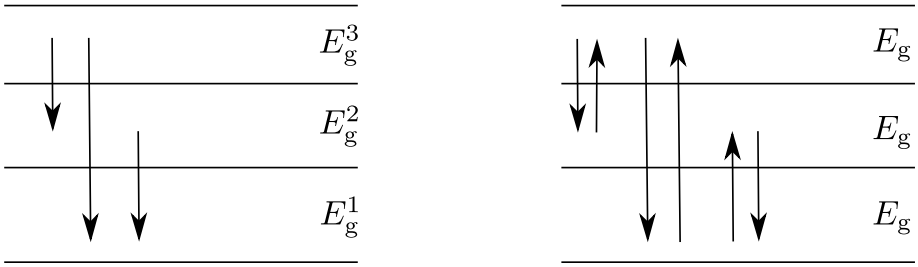

Figure 4.2.1: Luminescent coupling in (a) solar cells, (b) PPC's. The arrows represent LC fluxes. In solar cells, LC flux only goes from high bandgap layers to low bandgap layers; in PPC's, all layers have the same bandgap, and LC flux is bi-directional.

that LC mitigates efficiency loss due to absorption mismatch between layers in solar cells [36]. In PPCs, Reference [38] has shown that LC increases the bandwidth of the device. Layer thicknesses in PPCs are designed to match absorption in each layer at a particular wavelength of incident light. Due to dispersion in absorption coefficient, illuminating a PPC with photons that are not at the design wavelength causes absorption mismatch. Hence, widening the operation bandwidth is equivalent to reducing loss due to absorption mismatch in PPCs.

It is important to note the difference of LC between solar cells and PPCs. In a solar cell, LC is one-directional, as demonstrated in Figure 4.2.1(a). The reason is that each junction has a different bandgap in order to partition the solar spectrum; specifically, layers with higher bandgaps are placed on top of those with lower badgaps. Therefore, a layer in a solar cell can only absorb photons that are emitted from layers with higher bandgaps, but the layers with higher bandgaps absorb very little, if any, photons emitted from lower-bandgap layers. However, as demonstrated in Figure 4.2.1(b), in multi-layer PPCs, each layer is made of the same absorbing material. Hence, each layer in a PPC can absorb photons from all other layers. In this case, LC is bi-directional.

In Chapter 6, I present a multi-layer detailed balance model that includes bi-directional LC. This model is accurate on the level of ray-optics and allows for fast optimization in the space of layer thicknesses. No previous theory is able to treat bi-directional LC in PPC's on the detailed balance level. Only one model - Reference [38] - treats bi-directional LC in PPC's, but at a large computational costs. Other theories are designed to treat solar cells with only one-directional LC.

Here I discuss existing theories for LC. An LC model is typically divided into two parts: an optical part to trace photon absorption, and an electrical part to calculate current-voltage characteristics. These two parts are coupled and are required to be self-consistent. All optical models but one for LC are ray optics [39] [37] [40]. Reference [38] uses transfer matrix method (TMM) to map point-to-point LC efficiency in the device. For current-voltage characteristics, References [41, 35, 37] uses equivalent

circuits. Reference [40] is fundamentally a detailed balance theory. However, the calculations are performed using Boltzmann approximation, which, as discussed in Chapter 3, effectively turns the model into an equivalent-circuit model. Reference [38] uses a drift-diffusion-based device simulator (Synopsys Sentaurus). These methods include the effect of non-radiative recombination in a different manner. References [41, 35, 37] use different ideality factors in the diode equation to represent radiative and non-radiative recombination mechanisms, while Reference [40] uses internal radiative efficiency. In a drift-diffusion solver, as in Reference [38], non-radiative recombination is encoded in carrier diffusion length.

The models listed above have different computational costs, and each has its own strengths. The model in Reference [38] that includes wave-optics and drift-diffusion solver gives accurate result. However, it is hard to use this model to numerically optimize in the large space of design parameters, due to computational costs. Both equivalent-circuit and detailed-balance models use less computational resource than a drift-diffusion solver, allowing for optimizing design parameters. Detailed-balance models do not have the option to capture the effects related to reverse-bias breakdown in pn-junctions, which, for example, is modeled in Reference [41]. Equivalent circuits assume Boltzmann approximation intrinsically, while a detailed balance model can treat the degenerate limit. Nonetheless, Reference [40] uses the Boltzmann approximation in the detailed balance model. In fact, solar cells do not normally operate at a high input intensity to reach the degeneracy limit due to the available solar resource and the limiting concentration technologies. However, for studying the fundamental limiting efficiency, we desire a model that can treat the degenerate limit.

To study the fundamental conversion mechanism of PPC's, we require a fast detailed balance model on a similar level to Reference [40] that is capable of bi-directional luminescent coupling. Chapter 6 presents such a model that has the following features: (i) accuracy on the level of ray-optics, (ii) detailed-balance based theory in the degenerate limit, (iii) ability to treat non-radiative recombination loss using internal radiative efficiency.

4.3 Light Trapping

Light trapping (LT) techniques increase optical absorption path length, so a thin device with LT can absorb the same amount of incident light as a thick device without LT. Two benefits of a thin active layer that are relevant to PPCs are high efficiency and cost reduction. As discussed in Section 4.1, bulk non-radiative recombination loss scales as device thickness. Hence, a thin device benefits from LT in low bulk recombination loss, leading to a high efficiency. Also, when the absorbing material constitutes a large portion of the costs in a device, reducing thickness of the expensive material can

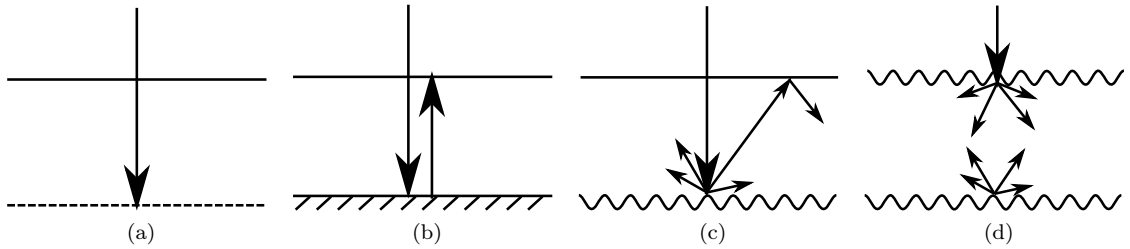

Figure 4.3.1: (a) Absorbing substrate. (b) Ideal specular back mirror. (c) Ideal Lambertian back mirror. (d) Ideal Lambertian top surface and ideal Lambertian back mirror.

help reducing costs. It is common to include one or more LT techniques in solar cells. However, no PPC has adopted any LT technique. Nonetheless, we expect PPCs to benefit from LT in the same way as solar cells do. In this section, I first discuss LT limit on absorption enhancement in bulk materials, followed by a brief overview of common LT techniques. I conclude this section by motivating an LT model tailored for multi-layer PPCs, which is presented in Chapter 6.

For the purpose of this thesis, I limit the discussion of LT to ray optics in bulk material, which is homogeneous and thick compared to the wavelength in interests. Ray optics do not consider the effects of coherent propagation of light. In PPC's, the wavelength of interests is the wavelength of the incident photons or the internally emitted photons. These two wavelengths are similar. In a solar cell, the wavelength of interests is determined by the band of photons that need absorption enhancement. Nevertheless, in the context of this thesis, we consider only monochromatic conversion at a wavelength of $\sim 1\,\mu$m. The definition of 'thick' is relative to $1\,\mu$m.

We roughly divide LT techniques into three types: (1) specular back reflector, (2) textured back reflector, and (3) textured top surface. These techniques are demonstrated in Figure 4.3.1. We consider a device without LT to be a device having an optically thick absorbing substrate, and a planar top surface with an ideal anti-reflection coating that admits all incident photons. From Section 2.2, for a device of thickness L, if the incident photons are normal to the surface of the device, and there is no LT, the absorbance of the device is:

$$a = 1 - e^{-\alpha L}. \tag{4.3.1}$$

For a material that absorbs weakly, for example, in an indirect bandgap material such as silicon, we can work in the weak-absorption limit, where $\alpha L \ll 1$. In this case, the absorbance is

$$a = \alpha L. \tag{4.3.2}$$

In this context, we can define effective absorption path length, L_{eff}, when LT is present, such that the

total absorbance of the device is

$$a_{\text{eff}} = \alpha L_{\text{eff}}. \tag{4.3.3}$$

Then, in the case without LT, $L_{\text{eff}} = L$ for normal incident photons. For oblique incidence, we have $L_{\text{eff}} = \frac{L}{\cos\theta}$, where θ is the internal angle between the propagation direction and the surface normal. The internal angle is related to the angle of incidence by Snell's law. When the incidence is normal, $\theta = 0$. Using LT, we aim to increase L_{eff} while keeping L constant. We start by considering a case when a specular back reflector is the only LT technique, as in Figure 4.3.1(b). A specular back reflector, for example, a metallic mirror, reflects photons back into the cell at the same angle of incidence. Ideally, the reflectivity is 1. A specular back reflector allows the incident photon flux to pass through the device twice. Hence, we consider that L_{eff} is doubled compared to the no-LT case. We can further improve L_{eff} by replacing the specular back reflector with a textured back reflector, as shown in Figure 4.3.1(c). A textured reflector that completely randomizes the angle of the reflected photons is called a Lambertian reflector, where the distribution of the reflected angle follows Lambert's Cosine Law. The photon flux reflected at an ideal Lambertian back reflector is expressed in θ as:

$$\phi_L = \frac{2\pi\Phi_0 \cos\theta}{2\pi \int_0^{\pi/2} \cos\theta \sin\theta \mathrm{d}\theta} = 2\Phi_0 \cos\theta \tag{4.3.4}$$

where Φ_0 is the angle-integrated reflected photon flux. As shown in Figure 4.3.1(c), when a photon is reflected at the textured back reflector with an angle larger than the angle of total internal reflection at the top surface, this photon is trapped inside the device and is absorbed eventually. Therefore, with a Lambertian back reflector, the enhancement of L_{eff} is significantly larger than 2. One can also texture the top surface to achieve LT. Here, we consider an ideal Lambertian top surface, as demonstrated in Figure 4.3.1(d). An ideal Lambertian top surface admits all incident photons into the cell at a random angle. Inside the cell, a photon reaches an ideal Lambertian top surface has a probability of $\frac{1}{n^2}$ of being transmitted to the outside, and $1 - \frac{1}{n^2}$ probability of being reflected back into the cell at a random angle. Here, n is the refractive index of the cell, and we assume that the outside of the cell is air and has a refractive index of 1. At any direction other than the vertical propagation, i.e., $\theta > 0$, L_{eff} of this direction is increased by a factor of $\frac{1}{\cos\theta}$. Therefore, a Lambertian top surface alone can achieve a large L_{eff} due to the random angle of propagation of the incident photons. Reference [42] showed, using statistical ray optics, that, when combining an ideal Lambertian top surface with an ideal Lambertian back reflector, we can achieve a maximum absorbance is

$$a_{\max} = \frac{4n^2\alpha L}{4n^2\alpha L + 1}. \tag{4.3.5}$$

In the weak-absorption limit,

$$a_{\max} = 4n^2 \alpha L. \tag{4.3.6}$$

Therefore, we have an enhancement of absorption path length of:

$$L_{\text{eff}}^{\max} = 4n^2 L. \tag{4.3.7}$$

For common PV materials, the enhancement is $4n^2 \simeq 50$. This means that we can reduce the thickness of a device by 50-folds and still absorb the same amount of incident photons compared to a device without LT. This $4n^2$ limit of absorption enhancement is known as the statistical-ray limit. To exceed this limit, one can exploit coherent optics in ultra-thin devices by using nanostructures, as discussed in Reference [43]. Again, in our context of PPC's, which are optically thick devices, we limit our discussion to ray-optics in this thesis.

In Chapter 6, I model a range of LT techniques in multi-layer PPCs in the framework of detailed balance and ray optics. Then, I demonstrate the improved efficiency and reduced cell thickness due to LT. I model LT using a semi-analytic ray-optic approach for a range of LT configurations, involving both specular and Lambertian surfaces. This ray-optic approach is similar to existing ray-optic based methods.

The model presented in Chapter 6 is distinct from existing models for LT in that most previous methods consider only the total number of photons absorbed in a single-layer device [44, 45, 46]. We are, however, also interested in where the photons are absorbed in a device. This information is crucial in a multi-layer detailed balance model. Reference [28], which presents a multi-layer model, considers only a metallic back reflector. The existing methods can be roughly divided into two categories: (1) semi-analytic, and (2) numerical. Semi-analytic models are developed using ray-optics for completely incoherent propagation. To model Lambertian surfaces in wave optics, Reference [47] modifies transfer matrix method (TMM) to include incoherent reflections at the surfaces. Semi-analytic LT models usually use Lambertian surface as an analogy to textured surfaces. To treat ordered structures at the surfaces, for example, ordered pyramids, numerical methods such as ray-tracing and finite-difference time-domain method (FDTD) are used [44, 43].

Real-world implementation of light-trapping involves surface texturing and back reflectors. Commercially mass-produced crystalline silicon solar cells use random pyramids on the top surface, that works in tendem with an anti-reflection coating to reduce reflection of the incoming light [48]. These random pyramids are commonly achieved using anisotropic etching that prefers certain crystal planes [20]. Reference [44] showed that random pyramids can achieve a similar level of light trapping compared to an ideal Lambertian surface. Another commonly used technique is a metallic back mirror or

a distributed Bragg reflector (DBR). A metallic back mirror can achieve reflectivities over 95% [20]. A DBR can achieve a higher reflectivity at a smaller band of wavelengths compared to metallic mirrors [20]. The record efficiency single-junction solar cell has a metallic back reflector that doubles as a back contact [49].

Light trapping is an important route to high efficiency PV. Although there have been numerous excellent LT models, it is still non-trivial to include both specular and Lambertian reflections in a multi-layer detailed balance model. Chapter 6 presents a multi-layer detailed balance model that includes specular and Lambertian surfaces using a ray-optics formalism.

Chapter 5

Extension of Green's Detailed Balance Theory in Single Layer

Daixi Xia, Matthew M. Wilkins, Sanmeet S. Chahal, Christopher E. Valdivia, Karin Hinzer, and Jacob J. Krich

This is a reproduction of an article presented at 7th World Conference On Photovoltaic Energy Conversion, June 2018, Waikoloa, Hawaii [50]. The original title is "Opportunities for Increased Efficiency in Monochromatic Photovoltaic Light Conversion". This chapter extends Green's single-layer theory, which is discussed in Chapter 3, and shows the efficiency effects due to: (1) non-radiative recombination loss parametrized by external radiative efficiency, (2) laser energy offset from the absorption bandgap of the device (detuning), (3) laser linewidth, (4) measured absorption coefficient instead of step-function approximation. Then, based on the experimental setup of the record-efficiency PPC, we predict the external radiative efficiency of the device. We then show the possible efficiency improevment from increasing laser intensity and decreasing laser energy offset from the bandgap. I used a different symbol for external radiative efficiency: ERE is used in this chapter and η_{ext} in all other chapters in this thesis.

5.1 Introduction

A monochromatic photovoltaic light converter – a phototransducer – converts narrow-band photonic energy into electricity. A high efficiency phototransducer enables several applications, including powering electronics through optical fiber. Inherently, an optical power transfer system is electrically isolated and protected from electromagnetic disturbances in the surroundings. As well, an optical source in the near infrared has small losses over long distance (4.5% over 100 m at 830 nm) in a silica fiber[18].

Hence, monochromatic photovoltaics are useful for many systems of telecommunication, biomedical engineering, electric vehicles and utilities, which sometimes require circuits immune to electromagnetic noise.

The detailed balance limit for monochromatic photovoltaic light conversion efficiency was shown by Green to be 100%, with the highest efficiencies requiring high input light intensity [19]. In previous architectures, an experimental monochromatic phototransducer showed conversion efficiency up to 58% with single junction cells in a series-connected architecture [11].

In 2016, our collaborators demonstrated a breakthrough in phototransducer efficiency with a 70% light-to-electricity conversion efficiency in a vertically-stacked multi-junction GaAs system [9]. In order to determine the best path forward to improve on this efficiency, we conduct a detailed study of the loss mechanisms of the record-setting device and incorporate them into a detailed-balance model of an equivalent single-junction device. We extend Green's detailed balance theory to include non-unity external radiative efficiency (ERE), allowing the detailed balance model to include non-radiative recombination.

5.2 Losses in Record-Setting Device

We introduce the 70% efficient phototransducer and describe its known sources of inefficiency due to thermalization, reflection, transmission, and series resistance. It is comprised of five GaAs p-n junctions separated by tunnel junctions, as illustrated in Figure 5.2.1 [9]. The phototransducer has a

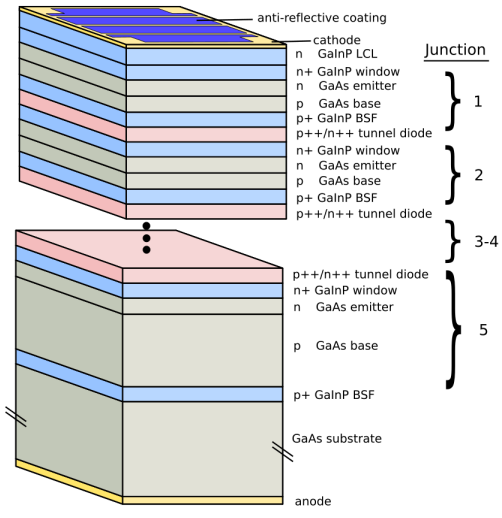

Figure 5.2.1: Layer structure of a monochromatic phototransducer with five series-connected GaAs p-n junctions. Each junction is capped with a window layer at the front and a back surface field (BSF) layer at the back. A thick lateral conduction layer (LCL) enables current to spread to the gridlines.

p-doped GaAs substrate, with a full coverage bottom contact. Each junction includes (from bottom to top) GaInP back surface field, p-doped GaAs base, thin n-doped GaAs emitter and n^+ GaInP front surface field (window). The lateral conduction layer of the top segment is designed to be extra-thick in order to allow carriers to reach the top contact with little loss. The top of the device has a gridline patterned contact. The voltage output of a single-junction cell is limited by the material's band gap, while a multi-junction design allows high voltage output from a single cell, eliminating fabrication complexities of a multi-cell array.

The segment thicknesses must be chosen to ensure current-matching at the operating wavelength, and the device is designed for an 830 nm (1.49 eV) input light source, which operated at 8 W/cm^2 with a FWHM of $\delta\epsilon = 1.8$ meV (i.e., FWHM of 1 nm). The GaAs band gap is at 870.7 nm (1.424 eV), so the device immediately loses 4% efficiency due to thermalization of the carriers to the GaAs band edge. This effect is included in the detailed balance model (see Section 5.3).

We measure the reflectance loss at 830 nm to be 2%. Light transmitted to the substrate is considered lost and is estimated to be approximately 1% of the input light using a transfer matrix method calculation of the device transmission [38]. We include these losses due to transmission and reflectance in the detailed balance calculation of Section 5.3 as a reduced absorbance.

Resistive losses, on the other hand, are not directly included in the detailed balance model. We have made a detailed SPICE model of the 5-junction device and estimate the resistive loss due to conduction in the semiconductor to be 1% [51, 52, 53]. Resistive losses in the grid fingers, the metalized coating on the busbars or back contacts are estimated to be similar, for total resistance losses of 2%. We therefore estimate that an equivalent device without series resistance would be over 72% efficient. We call this estimate the *internal efficiency*, which we can compare to detailed balance calculations. This internal efficiency allows us to determine a lower limit on the external radiative efficiency of the device and thus to determine the prospects for increasing efficiency by improving material quality.

5.3 Detailed Balance Model

5.3.1 Detailed Balance Condition

The detailed balance formalism allows determination of the thermodynamic limiting efficiency of photovoltaic devices. If each photon absorbed produces one excited electron-hole pair, then in steady-state operation, the collected current from a device must equal the difference between the number of photons it absorbs and the number of excited electrons that recombine[29]. If the device has infinite carrier mobility, then the electron and hole quasi-Fermi levels are uniform through the device and the radiative recombination can be expressed in terms of the applied voltage [27]. We begin with the simplest case

where all recombination is radiative, in which the current J can be expressed in terms of the applied voltage V as

$$\begin{aligned} J/q = &\int_0^\infty a(E) n_s(E) \mathrm{d}E \\ &- \frac{2\Delta\Omega}{h^3 c^2} \int_0^\infty \frac{a(E) E^2}{e^{(E-qV)/kT} - 1} \mathrm{d}E \end{aligned} \tag{5.3.1}$$

where the first term is the absorbed photon flux and the second term is the emitted photon flux, with $a(E)$ the photon-energy-dependent absorbance, $n_s(E)$ the input photon flux density, which in the case of a phototransducer has a small bandwidth, q the electric charge, h Planck's constant, c the speed of light, T the temperature, k Boltzmann's constant, and $\Delta\Omega$ the solid angle into which photons are emitted.

The experimental device has a multi-junction architecture, while our detailed balance model is for an analogous single-junction device. Our extended detailed-balance model captures the physics of incomplete absorption, thermalization, and radiative and nonradiative recombination (see Sec. 5.3.3), but predicts a high-current low-voltage output, where the experimental device has a low-current high-voltage output. We believe that the fundamental limiting efficiencies of the multi-junction device are well captured by the single-junction detailed balance model, but development of a multi-junction detailed balance model is required for confirmation.

5.3.2 Absorbance and Input Spectrum

Transparency and thermalization losses can be understood with models for $a(E)$ and $n_s(E)$. We extend Green's formalism to incorporate such loss mechanisms into the detailed balance model. We consider $n_s(E)$ to be Gaussian with central photon energy E_s and FWHM $\delta\epsilon$. The central energy can be represented in terms of the detuning from the band gap: $\delta E = E_\mathrm{s} - E_\mathrm{g}$. We consider two models for $a(E)$, as illustrated in Figure 5.3.1: first, a step function equal to 0 for $E \leq E_g$ and a_0 for $E \geq E_g$; second, a Beer-Lambert absorption model with experimentally measured GaAs absorptivity with thickness chosen so $a(E) = a_0$ at 830 nm [23]. In the step-function model, $a(E) = a_0 \Theta(E - E_\mathrm{g})$, where $a_0 = 0.97$ and Θ is the unit step function. With the step function absorbance model, Eq. (5.3.1) can be simplified to

$$\begin{aligned} J/q = &\frac{1}{2} a_0 \dot{N} \left[1 - \mathrm{erf}\left(2\sqrt{\ln 2} \frac{\delta E}{\delta\epsilon}\right)\right] \\ &- \frac{2 a_0 \Delta\Omega}{h^3 c^2} \int_{E_\mathrm{g}}^\infty \frac{E^2}{e^{(E-qV)/kT} - 1} dE \end{aligned} \tag{5.3.2}$$

where $\dot{N}$ is the total (energy integrated) input photon flux and erf is the standard error function.

Incident power is $P_{in} = \dot{N}(E_g + \delta E)$ and output power is $P_{out} = J(V)V$ which must be optimized over V. The maximum efficiency is $\eta = \frac{P_{out}}{P_{in}}$ at the optimum V. To illustrate the dependence of thermalization and transparency on δE and $\delta\epsilon$, Figure 5.3.2 shows optimum efficiency as a function of δE for different input linewidths $\delta\epsilon$. When the input radiation has a significant bandwidth $\delta\epsilon$, the optimal choice of detuning δE balances between the thermalization losses, which increase with δE, and transparency losses, which increase as δE becomes smaller than $\delta\epsilon$. For each $\delta\epsilon$, the maximum efficiency occurs when the transparency loss and thermalization loss are approximately equal, which requires $\delta E \approx \delta\epsilon$. This behavior is demonstrated in Figure 5.3.2 where narrower inputs give rise to higher maximum efficiencies at smaller detuning. As $\delta\epsilon \to 0$, the thermalization and transparency losses can be reduced to zero by choosing $\delta E \to 0$. In this fully monochromatic limit, the system would reach its highest efficiency. In contrast, the real absorbance model is less susceptible to transparency loss as $\delta E \to 0$, since the absorbance does not decrease to zero so abruptly (dashed lines).

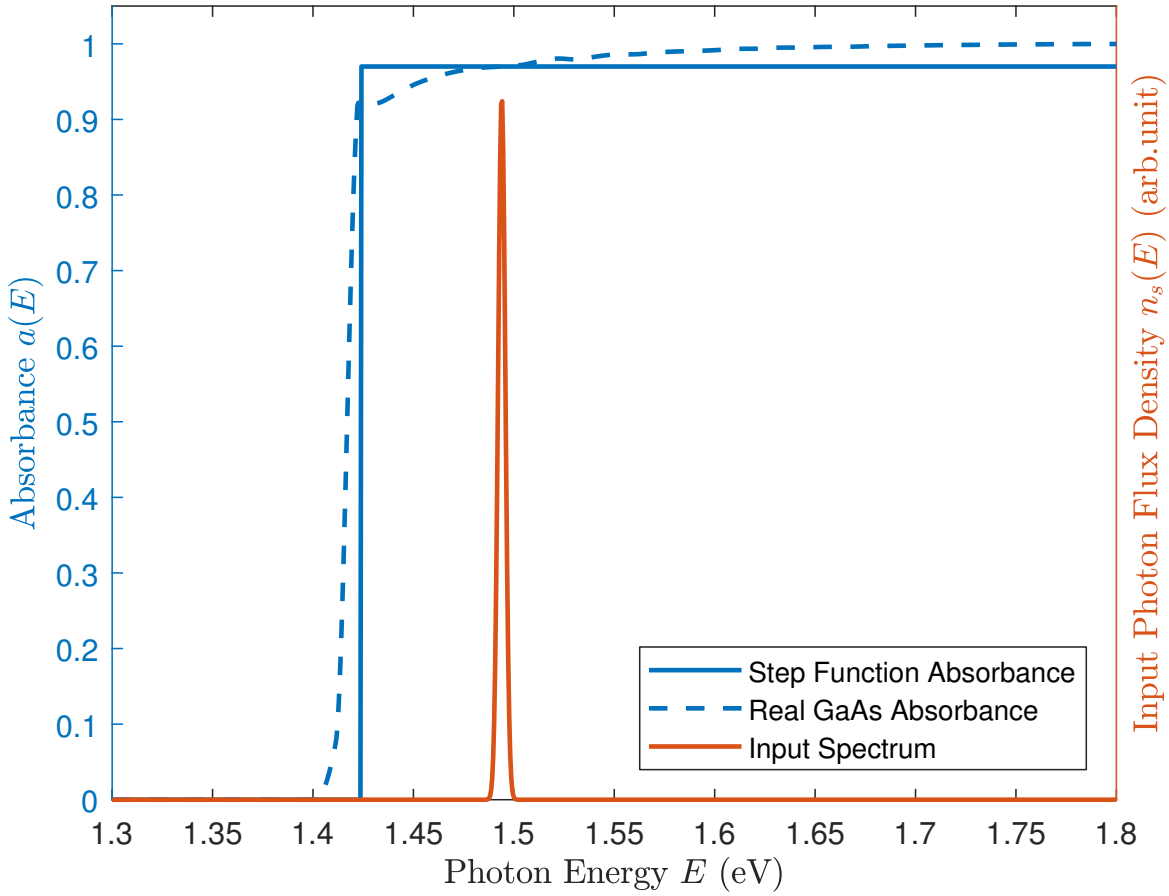

Figure 5.3.1: Two models of device absorbance (blue lines, left axis). The solid line shows the step function absorbance, and the dashed line shows Beer-Lambert absorbance calculated from experimentally measured GaAs absorption coefficient[23]. The device thickness is chosen so that at the design wavelength of 830 nm, the absorbance is 97%. Right axis: Gaussian input photon flux density $n_s(E)$ for the considered device. The central frequency is detuned by $\delta E = 0.07$ eV from the band gap. The FWHM $\delta\epsilon = 1.8$ meV.

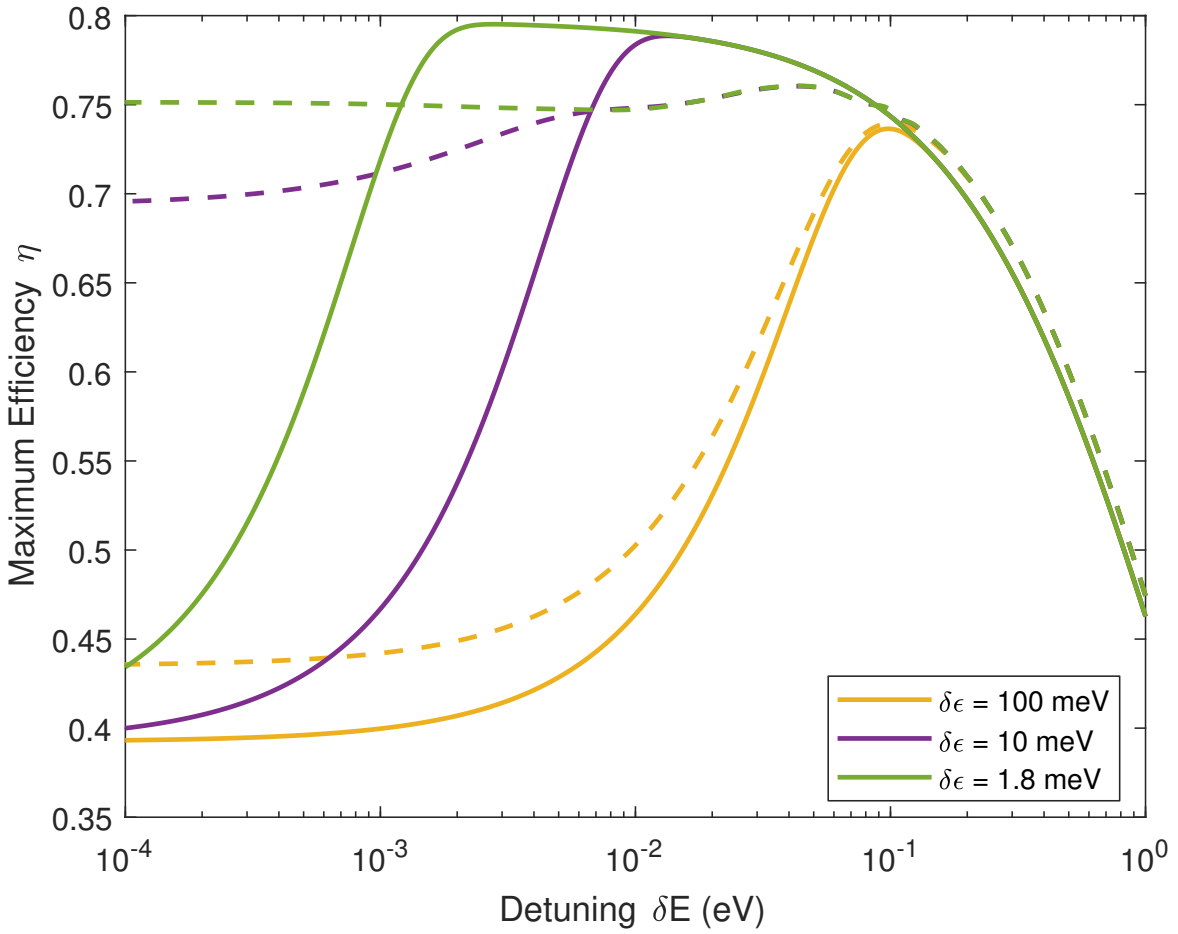

Figure 5.3.2: Detailed balance efficiency as a function of input light detuning δE for different input linewidths $\delta\epsilon$, $\Delta\Omega = \pi$ and laser power density 8 W/cm^2. The solid lines are for the step function absorbance model and the dashed lines are for the real absorbance model. The experimental device has $\delta\epsilon = 1.8$ meV and $\delta E = 0.07$ eV. Note that in the real absorbance model, device thickness is set to absorb 97% of the photons at 830 nm, so transmission loss increases as δE is reduced. The peak efficiency of 76% could be improved by increasing device thickness.

5.3.3 Non-Radiative Recombination

We extend the results of [19] to include nonradiative processes by means of the external radiative efficiency, ERE. In the detailed-balance formalism, radiative recombination is a loss mechanism only if the photons exit the device and thus cannot be reabsorbed, whereas nonradiative recombination is always a loss mechansim. The ERE is the fraction of all losses (including both nonradiative recombination and photon emission) that are due to photon emission from the device. The ERE of a cell is experimentally measurable and is associated with both material quality and device architecture [31]. Still in the step-function absorbance model, the current density is modified from Eq. (5.3.2) with the

inclusion of ERE as

$$\begin{aligned} J/q =& \frac{1}{2} a_0 \dot{N} \left[1 - \mathrm{erf}\left(2\sqrt{\ln 2} \frac{\delta E}{\delta \epsilon} \right) \right] \\ & - \frac{2\pi a_0}{h^3 c^2} \frac{\Delta\Omega}{ERE} \int_{E_\mathrm{g}}^{\infty} \frac{E^2}{e^{(E-qV)/kT} - 1} dE \end{aligned} \tag{5.3.3}$$

5.3.4 Normalized Intensity

Including the ERE does not significantly change the derivation of Green, nor does the presence of detuning δE. In the step-function absorbance case, the resulting efficiency depends on E_g/kT, δE, and the normalized input light intensity i,

$$i = \frac{h^3 c^2}{2} \frac{\dot{N} \cdot ERE}{\Delta\Omega E_\mathrm{g}^2 kT} \frac{1}{2} \left[1 - \mathrm{erf}\left(2\sqrt{\ln 2} \frac{\delta E}{\delta \epsilon} \right) \right]. \tag{5.3.4}$$

Then the (voltage dependent) efficiency can be written as

$$\eta = m a_0 \left[1 - \frac{1}{i} \ln\left(\frac{y+1}{y} \right) f \right] \left[1 - \frac{kT}{E_\mathrm{g}} \ln(y+1) \right], \tag{5.3.5}$$

where $y = \exp[(E_\mathrm{g} - qV)/kT] - 1$, $m = \frac{1}{2} \frac{1 - \mathrm{erf}\left(2\sqrt{\ln 2} \frac{\delta E}{\delta \epsilon}\right)}{1 + \frac{\delta E}{E_\mathrm{g}}}$ and f is a number close to 1, $1 \leq f \leq \left[1 + 2\frac{kT}{E_\mathrm{g}} + 2\left(\frac{kT}{E_\mathrm{g}}\right)^2\right]$.

The experiment, with emission angle $\Delta\Omega = \pi$, $\delta E = 70$ meV, $\delta\epsilon = 1.8$ meV and laser intensity of 8 W/cm^2 [9], corresponds to a normalized intensity of $i = 0.0065 \cdot ERE$.

Device efficiency increases with i until saturating near unity, as shown in Figure 5.3.3. This normalized intensity shows that the same improvement in efficiency can be achieved by increasing the input photon flux, increasing the material quality (i.e., ERE), or restricting $\Delta\Omega$. The upper axis shows how this normalized intensity corresponds to laser intensities, assuming that $\Delta\Omega = \pi$ and that δE and $\delta\epsilon$ are fixed to their values from the considered device. At the experimental intensity, with no nonradiative processes, the detailed balance calculation would predict $\eta = 76\%$, which is higher than the estimated internal efficiency of 72%, indicating that the ERE of the device is in fact less than 1, as expected. The normalized intensity corresponding to 72% efficiency is $i = 0.0006$. The device is thus estimated to have an ERE of 10%.

Even with realistic absorption profiles, where Eq. 5.3.5 does not strictly apply, i gives a very good estimate of a device's efficiency. In Figure 5.3.3, the detailed balance efficiency is also calculated based on the real GaAs absorbance model with varying intensities, using a_0, δE, $\delta\epsilon$ and ERE as for the step-function model. Both curves show the same increase of efficiency with i and nearly the same absolute efficiency. The step-function absorbance model overestimates the efficiency by about 1%, due

to an underestimate of sub-bandgap photon emission. Due to this sub-bandgap absorbance, we do not extend the real absorbance model to input intensity higher than 10^4 W/cm^2. High intensity results in an operating voltage very close to the band gap, where in the real absorbance model, the absorbance is non-zero. Such lasing behavior is not captured in the current formalism. A generalized cell analysis including such effects is possible [30], and we expect it to give results similar to our step-function analysis with an asymptote at a slightly lower maximum η. Nevertheless, in the moderate-intensity regime, the step function model and i provide accurate and intuitive information on the relative efficiency improvements possible with changes to the physical parameters.

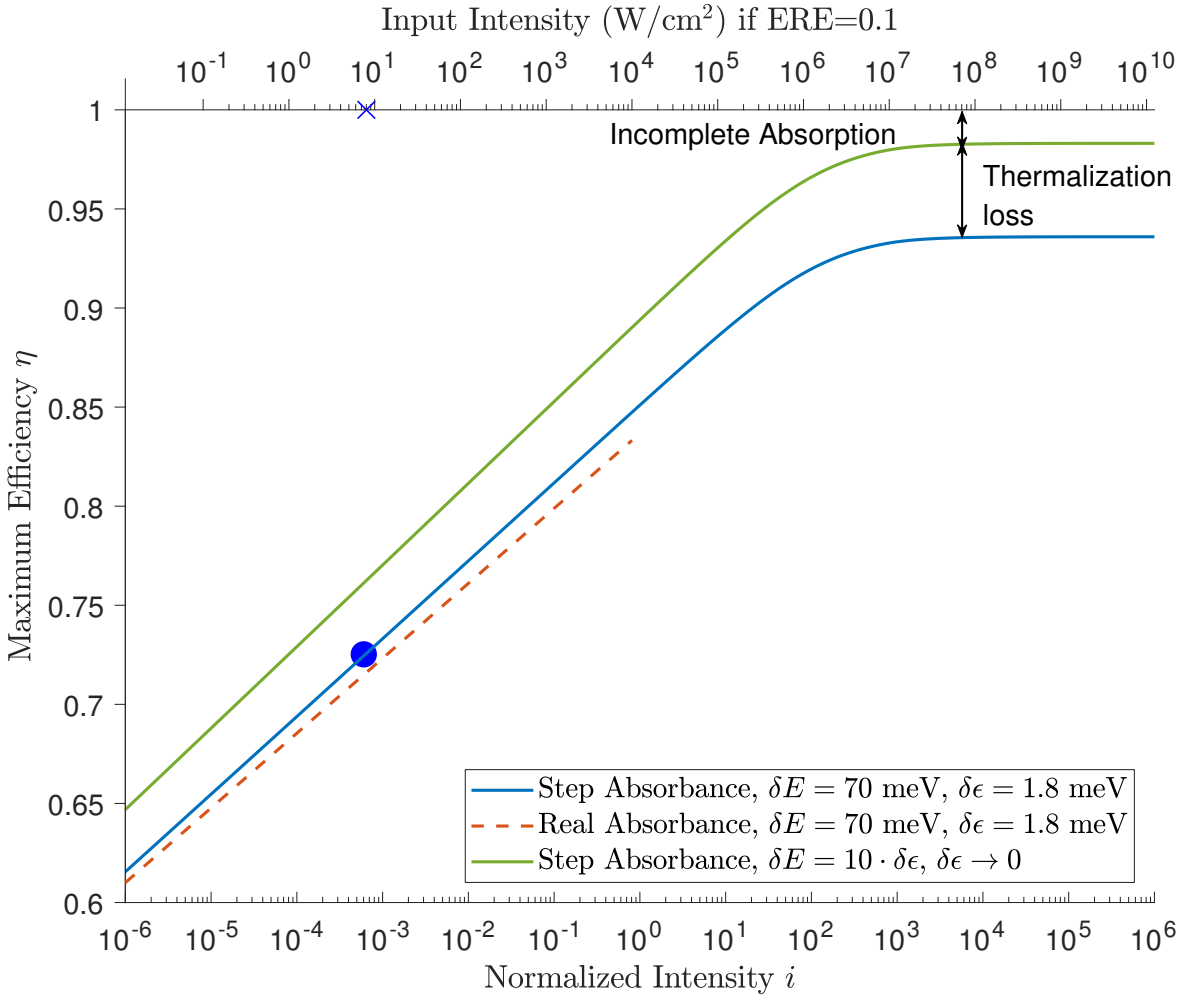

Figure 5.3.3: Efficiency as a function of normalized intensity i (bottom axis), first calculated using the definition in Eq. 5.3.4, for a material with $E_g = 1.424$ eV and step function $a(E)$ with $a_0 = 0.97$ with detuning $\delta E = 0.07$ meV (blue curve). The line asymptotes at 92% due to finite detuning and incomplete absorption. The point with $\eta = 0.72$ shows the estimate of the internal efficiency of the 70% efficient device when series resistance is removed. The green curve is the efficiency in the monochromatic limit, where $\delta E = 10\delta\epsilon$ and $\delta\epsilon \to 0$. The line asymptotes at 97% due to incomplete absorption. The top axis shows the input intensity with $\delta\epsilon = 1.8$ meV, detuning $\delta E = 0.07$ eV, emission angle $\Delta\Omega = \pi$ and ERE= 10%. The device operates at 8 W/cm^2[9], which is marked on the top axis. Efficiency is also calculated based on the real GaAs absorbance model illustrated in Figure 5.3.1, with δE, $\delta\epsilon$, ERE and $\Delta\Omega$ as above.

5.4 Implications for High Efficiency

There are two important parameters that determine the efficiency of a phototransducer - the detuning to linewidth ratio $\frac{\delta E}{\delta \epsilon}$ and the normalized intensity i. In this section, we discuss possible improvement of efficiency based on these two parameters.

The current device was not designed at its theoretical optimal δE, as shown in Figure 5.3.2. If the input wavelength can be adjusted without changing its bandwidth, the efficiency can be improved by 2% absolute by decreasing the detuning to 0.03 eV. However, at a smaller detuning, more material is needed in order to achieve the same 97% effective absorbance, due to smaller GaAs absorptivity. For a detuning of 0.03 eV, the device would be 20% thicker than the present one to achieve the same absorbance. It is also worth noting that an LED light source with $\delta\epsilon$ 1 to 2 orders of magnitude larger gives a smaller window of optimum detuning as well as lower optimal efficiency. Yet a device with the current thickness, $\delta\epsilon$ increased by 2 orders of magnitude and carefully tuned central wavelength could have an efficiency similar to the current record-setting device, without requiring a laser input.

Increasing normalized intensity i also significantly improves the efficiency. As shown in Figure 5.3.3, increasing i by an order of magnitude would improve the efficiency by approximately 4%. This increase can be achieved by increasing input power density to 100 W/cm^2, restricting the emission angle $\Delta\Omega$ using a lens, or improving material quality (ERE), with each having a similar effect. The ERE of 10% predicted here is already very high among III-V devices, with the highest measured ERE= 22.5% for thin film GaAs [31]. Since further increases in material quality are difficult, improved efficiency from increased input power density seems to be the easiest method.

In summary, with 2% improvement from smaller detuning and 4% from increasing input intensity, combined with improvements in series resistance, reflection, and transmission, a device efficiency of over 80% appears reachable at an operating wavelength of 850 nm.

Chapter 6

Multi-Layer Detailed Balance Model

Daixi Xia and Jacob J. Krich

This article discusses a multi-layer detailed balance model, which includes the effects of (1) luminescent coupling, (2) photon recycling, (3) non-radiative recombination loss parametrized by internal radiative efficiency, in additon to the effects studied in Chapter 5. We show layer-thickness-optimized efficiency of multi-layer monochromatic conversion, with a range of material quality and light-trapping schemes. This article has not yet been accepted for publication.

6.1 Introduction

In both solar and monochromatic photovoltaics, it is well-known that a multijunction device reduces series-resistance loss compared to a single-junction equivalent, because of the low-current, high-voltage operation. High efficiency devices also rely on both photon recycling within a layer and luminescent coupling (LC) between layers, effects that are essential to accurate prediction of device performance. Monochromatic photovoltaics, also called photonic power converters (PPC's), are increasingly important components of optical power transmission systems. LC has been well studied in solar cells [40, 36, 41, 32, 37] and has been implemented in a drift-diffusion solver for PPC's [38]. There is, however, no previous detailed-balance model including LC in multijunction PPC's. Though these photovoltaic technologies are similar, there is a crucial difference between LC in solar cells and in PPC's: in solar cells, internally emitted photons can only be absorbed in the layers with lower bandgaps, so LC is one-directional; in PPC's, because all layers have the same band gap, LC is bi-directional. Previous LC models also treat only specular reflections.

High-efficiency PPC's enable wireless power transmission isolated from electromagnetic disturbance, with applications in electric vehicles, biomedical implants, telecommunications, drones, and satellites

[54, 2, 3, 1]. The record-efficiency PPC is a vertical multijunction structure with 5 GaAs pn junctions coupled with tunnel diodes; it obtained an efficiency of 70% and operating voltage of greater than 5 V at an input power density of 8 W/cm^2 [9]. Even without consideration of series resistance, increased voltage is desirable in applications because of the removal of the need to boost the voltage. In this work, we use the term "layers" to refer to the active absorbing pn junctions, to avoid confusing these absorbing junctions with tunnel diodes, which are often called tunnel junctions.

In 2001, Green used the detailed-balance formalism to show that monochromatic photovoltaic conversion can be 100% efficient at infinite incident intensity [19]. Green's theory is a single-layer model, which does not capture the low current, high voltage of multi-layer operation and does not consider LC in a multi-layer device. In this work, we extend Green's theory to a multi-layer detailed-balance model and include bidirectional LC. Our model treats both specular and Lambertian top and bottom surfaces, variable incident light bandwidth, energy offset between incident light and material band gap, and nonradiative recombination by parametrizing with an internal radiative efficiency η_{int}. We use this model to study a range of devices based on the record-efficiency PPC [9], showing the efficiency potential for future device architectures. We show that PPC efficiency increases with the number of layers, even without series-resistance loss, when the device has an absorbing substrate. This effect is not present for devices with a back reflector. We explain the origin of this effect using a simple analytic 2-layer model. This model also enables study of multijunction solar cells, with flexible application to include light trapping top and bottom surfaces.

Section 6.2 introduces the detailed balance model for a 1-layer device, including treatment of reflections from top and bottom surfaces. Section 6.3 extends this theory to the multi-layer case. Section 6.4 shows how to transform the nonlinear equations for current J as a function of voltage V into a set of linear equations that allow computationally efficient extraction of $V(J)$. Section 6.5 applies the multi-layer theory to PPC's with a range of η_{int} values and light-trapping configurations, showing the intrinsic efficiency increase with number of layers when the device has an absorbing substrate. Section 6.6 explains the intrinsic efficiency increase using an analytic 2-layer model.

6.2 Single-layer Detailed Balance

We model a planar cell with infinite area and finite thickness L of the active region, as shown in Fig. 6.2.1. The detailed balance condition in this cell is

$$J = J^{\text{in}} - J^{\text{loss}}, \tag{6.2.1}$$

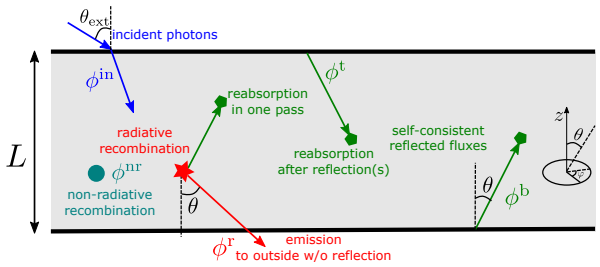

Figure 6.2.1: Absorption and recombination events in a single-layer cell.

where J is the extracted current density, J^{in} is the number of incident photons absorbed per area per time, J^{loss} is the net loss of current density due to electron-hole recombination, and we set the electric charge $q = 1$. J^{loss} is a function of the quasi-Fermi level separation μ, described further below. We make standard detailed balance assumptions that carrier mobilities are infinite so μ equals the applied voltage and that one photon generates one electron-hole pair [29]. The efficiency of the device is:

$$\eta(\mu) = \frac{J(\mu)\,\mu}{P_{\text{in}}} \tag{6.2.2}$$

where P_{in} is the incident power density. The maximum efficiency is obtained by optimizing η with respect to μ.

To model both J^{in} and J^{loss}, we trace the absorption and emission of photons using ray optics. We use an angle-resolved 2D model, isotropic in the azimuth, suitable for layered structures. As shown in Fig. 6.2.1, θ is the angle between the direction of propagation of the photons and the normal of the cell, defined from 0 to $\pi/2$. When the top or bottom surfaces have specular reflections, photons with angle θ are coupled to those with angle $\pi - \theta$, and we label these populations with $\theta \in [0, \pi/2]$. Alternatively, a Lambertian surface couples photon populations of all angles to each other.

The only challenging part of evaluating Eq. 6.2.1 lies in keeping track of the reflections off the top and bottom surfaces, both from incident and radiatively produced radiation. Both of these processes share the same algebraic form, and we now describe the resulting self-consistency condition including reflections.

6.2.1 Self-Consistency Condition for Reflections

Consider the inward-directed photon fluxes from the top and bottom surfaces with angle θ and energy E, $\phi^{t}(\theta, E)$, and $\phi^{b}(\theta, E)$, respectively. A self-consistency relation connects these quantities; it was used to model photon recycling – reabsorption of internally emitted photons in a single-layer device – in Ref. [45] with specular reflection. Here, we exploit this self-consistency relation to model both photon recycling in single-layer structures and luminescent coupling in multi-layer structures and extend it to

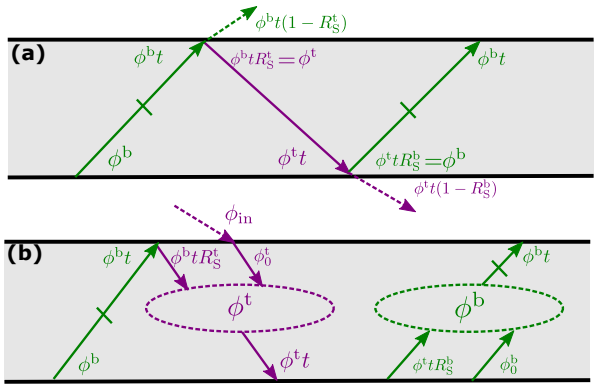

Figure 6.2.2: Self-consistency relation between top and bottom inward photon fluxes, $\phi^{\mathrm{t}}(\theta, E)$, and $\phi^{\mathrm{b}}(\theta, E)$, (a) without source terms and (b) with source terms $\phi_0^{\mathrm{t}}(\theta, E)$ and $\phi_0^{\mathrm{b}}(\theta, E)$. Figure shows specular top and bottom surfaces. In the case where the source is from external radiation ϕ_{in}, $\phi_0^{\mathrm{t}} = \phi_{\mathrm{in}}(1 - R_{\mathrm{ext}})$.

include Lambertian reflections.

Consider first specular reflections from top and bottom surfaces. As shown in Fig. 6.2.2, the inward photon flux at one surface must be equal to the flux at the opposite surface that is transmitted through the entire cell and reflects at the considered surface. This relation is expressed as:

$$\phi^{\mathrm{t}}(\theta, E) = \phi^{\mathrm{b}}(\theta, E)\, t(\theta, E)\, R_{\mathrm{S}}^{\mathrm{t}}(\theta, E) \tag{6.2.3}$$

$$\phi^{\mathrm{b}}(\theta, E) = \phi^{\mathrm{t}}(\theta, E)\, t(\theta, E)\, R_{\mathrm{S}}^{\mathrm{b}}(\theta, E) \tag{6.2.4}$$

where $R_{\mathrm{S}}^{\mathrm{t}}(\theta, E)$ and $R_{\mathrm{S}}^{\mathrm{b}}(\theta, E)$ are internal specular reflectivity at the top and bottom surface, respectively. We also define θ- and E-resolved transmittance and absorbance:

$$t(\theta, E) = e^{-\frac{\alpha(E)L}{\cos\theta}} \tag{6.2.5}$$

$$a(\theta, E) = 1 - t(\theta, E) \tag{6.2.6}$$

where $\alpha(E)$ is the absorption coefficient, which we assume to be uniform in space inside the cell. Eqs. (6.2.3), (6.2.4) can be read from Fig. 6.2.2(a). As written, they have only the trivial solution $\phi^{\mathrm{t}} = \phi^{\mathrm{b}} = 0$, but they express the self-consistency condition that still applies when sources such as external radiation or radiative recombination are included. See below, Eqs. 6.2.11 , 6.2.12. We also construct this self-consistency relation with one or two Lambertian surfaces present. A Lambertian surface is an ideal diffuse scatterer that randomizes the angle of reflected and transmitted rays [46, 55]. Because all photons travel at random angles, the important quantity is the θ-averaged flux, $\Phi^{\mathrm{t}}(E)$,

Table 6.1: Solution of ϕ^{t} and ϕ^{b} from Equations (6.2.11) and (6.2.12). Depending on the source terms, these solutions appear in the text as $\phi_{\mathrm{in}}^{\mathrm{t/b}}$ for incident photons or as $\phi_{\mathrm{lc}}^{\mathrm{t/b}}$ for reflected luminescent coupling. The solution for Lambertian top and specular bottom is symmetric to the solution of specular top and Lambertian bottom, with t↔b exchanged

	Surface Types	$\phi^{\mathrm{t}}(\theta,E)$	$\phi^{\mathrm{b}}(\theta,E)$
Eq. 6.2.11a, 6.2.12a	Specular top Specular bottom	$\frac{\phi_0^{\mathrm{b}} t R_{\mathrm{S}}^{\mathrm{t}}+\phi_0^{\mathrm{t}}}{1-t^2 R_{\mathrm{S}}^{\mathrm{t}} R_{\mathrm{S}}^{\mathrm{b}}}$	$\frac{\phi_0^{\mathrm{t}} t R_{\mathrm{S}}^{\mathrm{b}}+\phi_0^{\mathrm{b}}}{1-t^2 R_{\mathrm{S}}^{\mathrm{t}} R_{\mathrm{S}}^{\mathrm{b}}}$
Eq. 6.2.11b, 6.2.12b	Lambertian top Lambertian bottom	$2\cos\theta \frac{\Phi_0^{\mathrm{b}} \mathcal{T} R_{\mathrm{L}}^{\mathrm{t}}+\Phi_0^{\mathrm{t}}}{1-\mathcal{T}^2 R_{\mathrm{L}}^{\mathrm{t}} R_{\mathrm{L}}^{\mathrm{b}}}$	$2\cos\theta \frac{\Phi_0^{\mathrm{t}} \mathcal{T} R_{\mathrm{L}}^{\mathrm{b}}+\Phi_0^{\mathrm{b}}}{1-\mathcal{T}^2 R_{\mathrm{L}}^{\mathrm{t}} R_{\mathrm{L}}^{\mathrm{b}}}$
Eq. 6.2.11a, 6.2.12b	Specular top Lambertian bottom	$2\cos\theta \frac{\int_0^{\pi/2} \sin\theta' \mathrm{d}\theta' \left(\phi_0^{\mathrm{t}} t R_{\mathrm{L}}^{\mathrm{b}}+\phi_0^{\mathrm{b}}\right)}{1-\int_0^{\pi/2} \sin\theta' \mathrm{d}\theta' \cos\theta' t^2 R_{\mathrm{S}}^{\mathrm{t}} R_{\mathrm{L}}^{\mathrm{b}}} t R_{\mathrm{S}}^{\mathrm{t}} + \phi_0^{\mathrm{t}}$	$2\cos\theta \frac{\int_0^{\pi/2} \sin\theta' \mathrm{d}\theta' \left(\phi_0^{\mathrm{t}} t R_{\mathrm{L}}^{\mathrm{b}}+\phi_0^{\mathrm{b}}\right)}{1-\int_0^{\pi/2} \sin\theta' \mathrm{d}\theta' \cos\theta' t^2 R_{\mathrm{S}}^{\mathrm{t}} R_{\mathrm{L}}^{\mathrm{b}}}$

and $\Phi^{\mathrm{b}}(E)$:

$$\Phi^{\mathrm{t}}(E) = \int_0^{\pi/2} \sin\theta' \mathrm{d}\theta' \phi^{\mathrm{t}}(\theta', E) \tag{6.2.7}$$

$$\Phi^{\mathrm{b}}(E) = \int_0^{\pi/2} \sin\theta' \mathrm{d}\theta' \phi^{\mathrm{b}}(\theta', E) \tag{6.2.8}$$

From the Lambert cosine law, the θ-resolved fluxes are related to the θ-averaged fluxes as [55]:

$$\phi^{\mathrm{t}}(\theta, E) = 2\cos\theta \Phi^{\mathrm{t}}(E) \tag{6.2.9}$$

$$\phi^{\mathrm{b}}(\theta, E) = 2\cos\theta \Phi^{\mathrm{b}}(E) \tag{6.2.10}$$

Therefore, combining Equations (6.2.3), (6.2.4) and (6.2.7) to (6.2.10),

$$\phi^{\mathrm{t}}(\theta, E) = 2\cos\theta \int_0^{\pi/2} \sin\theta' \mathrm{d}\theta' \phi^{\mathrm{b}}(\theta', E)\, t(\theta', E)\, R_{\mathrm{L}}^{\mathrm{t}}(E)$$

$$\phi^{\mathrm{b}}(\theta, E) = 2\cos\theta \int_0^{\pi/2} \sin\theta' \mathrm{d}\theta' \phi^{\mathrm{t}}(\theta', E)\, t(\theta', E)\, R_{\mathrm{L}}^{\mathrm{b}}(E)$$

where $R_{\mathrm{L}}^{\mathrm{t}}(E)$ and $R_{\mathrm{L}}^{\mathrm{b}}(E)$ are E-resolved Lambertian reflectivities of the top and bottom surfaces, respectively.

Internal and external sources of photons add to these self-consistent fluxes, as shown in Fig. 6.2.2(b). We express the inward-directed source at the top and bottom surfaces as $\phi_0^{\mathrm{t}}(\theta, E)$ and $\phi_0^{\mathrm{b}}(\theta, E)$, respectively. With these sources, the self-consistency conditions at top and bottom are:

$$\text{Specular: } \phi^{\mathrm{t}} = \phi^{\mathrm{b}} t R_{\mathrm{S}}^{\mathrm{t}} + \phi_0^{\mathrm{t}} \tag{6.2.11a}$$

$$\text{Lambertian: } \phi^{\mathrm{t}} = 2\cos\theta \int_0^{\pi/2} \sin\theta' \mathrm{d}\theta' \left(\phi^{\mathrm{b}} t R_{\mathrm{L}}^{\mathrm{t}} + \phi_0^{\mathrm{t}}\right) \tag{6.2.11b}$$

$$\text{Specular: } \phi^{\mathrm{b}} = \phi^{\mathrm{t}} t R_{\mathrm{S}}^{\mathrm{b}} + \phi_0^{\mathrm{b}} \tag{6.2.12a}$$

$$\text{Lambertian: } \phi^{\mathrm{b}} = 2\cos\theta \int_0^{\pi/2} \sin\theta' \mathrm{d}\theta' \left(\phi^{\mathrm{t}} t R_{\mathrm{L}}^{\mathrm{b}} + \phi_0^{\mathrm{b}}\right) \tag{6.2.12b}$$

where the θ, E dependence of all variables has been suppressed. We solve for $\phi^{\mathrm{t}}(\theta, E)$ and $\phi^{\mathrm{b}}(\theta, E)$ in terms of the source terms, for all four combinations of specular and Lambertian cases. The results are listed in Table 6.1, where for simplicity of notation, we define angle-averaged transmittance with a Lambertian surface and angle averaged source fluxes:

$$\mathcal{T} = \int_0^{\pi/2} \sin\theta' \mathrm{d}\theta' 2\cos\theta' t(\theta') \tag{6.2.13}$$

$$\Phi_0^{\mathrm{t/b}} = \int_0^{\pi/2} \sin\theta' \mathrm{d}\theta' \phi_0^{\mathrm{t/b}}. \tag{6.2.14}$$

6.2.2 Current Due To Incident Photons

With the multiple-reflection problem solved, we can express J^{in} from Eq. 6.2.1. We consider illumination arriving at only the top surface, hence we take the source terms in Table 6.1 to be:

$$\phi_0^{\mathrm{t}}(\theta, E) = \phi_{\mathrm{in}}(\theta, E)\left[1 - R_{\mathrm{ext}}^{\mathrm{t}}(\theta, E)\right] \tag{6.2.15a}$$

$$\phi_0^{\mathrm{b}}(\theta, E) = 0 \tag{6.2.15b}$$

where $\phi_{\mathrm{in}}(\theta, E)$ is the number of incident photons hitting the top surface of the cell per area per time per angle per energy, $R_{\mathrm{ext}}^{\mathrm{t}}(\theta, E)$ is the external top surface reflectivity. In experiments, the incident flux and external reflectivity is measured in external angles, which are related to the internal angle θ through Snell's law with a specular surface or the Lambert cosine law with a Lambertian surface. We express the incident flux and external reflectivity using internal angle for simplicity of notation, and connection to experiment requires adjusting angles accordingly. We substitute Eq. 6.2.15 into Table 6.1 and obtain the current due to incident photon absorption:

$$J^{\mathrm{in}} = \int_{\mathrm{hemisphere}} \mathrm{d}\Omega \int_0^{\infty} \mathrm{d}E \left[\phi_{\mathrm{in}}^{\mathrm{t}} + \phi_{\mathrm{in}}^{\mathrm{b}}\right] a \tag{6.2.16}$$

where the subscript denotes that these fluxes are due only to the incident photons and their reflections, not to any internal radiative process, which will be counted in J^{loss}.

6.2.3 Current Due To Recombination and Photon Recycling

We calculate J^{loss} using the internal per volume emission rate and our ray-optics model to trace the reabsorption events. We calculate the θ- and E-resolved net loss of current and integrate over solid angles and energy to obtain the total loss of current, J^{loss}. Note that for the single-layer case, this explicit ray tracing of internally emitted photons is not required, as the formulation of Green showed [19]. When we move to the multi-layer case, however, we must be able to track internally emitted photons and determine where they are absorbed, which requires the formalism presented here.

The θ- and E-resolved net loss of current is divided into three parts: (1) photon flux emitted out of the cell in either up or down direction, $\phi^r(\theta, E, \mu)$, not including any reflections, (2) carriers lost through nonradiative recombination, $\phi^{\text{nr}}(E, \mu)$, and (3) recycled photons absorbed after internal reflections, which enter as a negative loss, $\phi^{\text{lc}}(E, \mu)$. In the multi-layer case, this term will represent luminescent coupling between layers. Then, J^{loss} is

$$J^{\text{loss}}(\mu) = \int_{\text{hemisphere}} \mathrm{d}\Omega \int_0^\infty \mathrm{d}E \Big[2\phi^{\text{r}}(\theta, E, \mu) + 2\phi^{\text{nr}}(E, \mu) - \phi^{\text{lc}}(\theta, E, \mu) \Big] \tag{6.2.17}$$

Note that the factors of 2 in Eq. 6.2.17 account for both up and down propagation of photons at angle θ, since we only integrate the solid angle over a hemisphere. From here, angular integrations are always over only a hemisphere. The three terms in Eq. 6.2.17 all depend on the internal radiative emission rate S^{r}, which has dimensions of number per time per volume per energy per solid angle [27]:

$$S^{\text{r}}(E, \mu) = \alpha(E)\, n^2(E)\, \frac{2}{h^3 c^2} \frac{E^2}{e^{(E-\mu)/kT} - 1} \tag{6.2.18}$$

where $n(E)$ is the refractive index, h is Planck's constant, c is the speed of light, k is Boltzmann's constant, T is the temperature of the cell, and μ is the quasi-Fermi level splitting in the cell. We assume that μ, T, n, and α are spatially uniform inside the cell, leading to spatial uniformity of S^{r}. Eq. 6.2.18 implies that emission events produce photons isotropically in the cell. A photon emitted upwards at angle θ and at position $L - z$ has a probability of $e^{-\frac{\alpha(E) z}{\cos\theta}}$ to escape the cell, if there are no internal reflections. On integrating z from 0 to L, we obtain ϕ^{r} in Eq. 6.2.17:

$$\phi^{\text{r}}(\theta, E, \mu) = \int_0^{L_i} e^{-\frac{\alpha(E) z}{\cos\theta}} S^r(E, \mu)\, \mathrm{d}z \tag{6.2.19}$$

$$= \frac{\cos\theta}{\alpha(E)} a(E, \theta)\, S^r(E, \mu). \tag{6.2.20}$$

We define the geometry factor, g^{r}:

$$g^{\mathrm{r}}(E,\theta) = \frac{\cos\theta}{\alpha(E)} a(E,\theta), \tag{6.2.21}$$

so $\phi^{\mathrm{r}}(\theta,E,\mu) = g^{\mathrm{r}}(E,\theta) S^{r}(E,\mu)$.

We include nonradiative recombination using η_{int}, internal radiative efficiency, which is defined as the fraction of recombination events that are radiative. In principle, η_{int} can depend on position and voltage, but we assume uniform and constant η_{int} in the cell. Then, the total nonradiative loss is proportional to L and S^{r}. Similar to Eq. 6.2.21, we express ϕ^{nr} in Eq. 6.2.17 as $\phi^{\mathrm{nr}}(E,\mu) = g^{\mathrm{nr}}(E,\theta) S^{r}(E,\mu)$ where

$$g^{\mathrm{nr}}(E,\theta) = \left(\frac{1}{\eta_{\mathrm{int}}} - 1\right) L. \tag{6.2.22}$$

The flux of photons that are internally emitted then reflected satisfies the self-consistency relation as discussed in Section 6.2.1. We use Table 6.1 to calculate $\phi^{\mathrm{t}}_{\mathrm{lc}}$ and $\phi^{\mathrm{b}}_{\mathrm{lc}}$, where the subscript indicates that the source originates from the internally emitted photons. We write the source terms as

$$\phi_0^{\mathrm{bdy}}(\theta,E) = g^{\mathrm{r}}(E,\theta) S^{\mathrm{r}}(E,\mu) R^{\mathrm{bdy}}(\theta,E) \tag{6.2.23}$$

where bdy is either t or b and R^{bdy} is specular or Lambertian reflectivity, depending on the boundary conditions chosen. Then ϕ^{lc} in Eq. 6.2.17 is

$$\phi^{\mathrm{lc}} = a\left(\phi^{\mathrm{t}}_{\mathrm{lc}} + \phi^{\mathrm{b}}_{\mathrm{lc}}\right). \tag{6.2.24}$$

We observe from Table 6.1 and Eq. 6.2.23 that both $\phi^{\mathrm{t}}_{\mathrm{lc}}$ and $\phi^{\mathrm{b}}_{\mathrm{lc}}$ are linear in $S^{\mathrm{r}}(E,\mu)$, allowing writing ϕ_{lc} as $\phi_{\mathrm{lc}} = g^{\mathrm{lc}}(E,\theta) S^{\mathrm{r}}(E,\mu)$.

Putting these results together, we express J_{loss} using the total geometry factor, $g(E,\theta)$:

$$J_{\mathrm{loss}} = \int \mathrm{d}\Omega \int_0^{\infty} \mathrm{d}E\, g(E,\theta) S^{\mathrm{r}}(E,\mu) \tag{6.2.25}$$

where $g(E,\theta) = 2g^{\mathrm{r}}(E,\theta) + 2g^{\mathrm{nr}}(E,\theta) + g^{\mathrm{lc}}(E,\theta)$, and we can now evaluate all terms in Eq. 6.2.17 for $J^{\mathrm{loss}}(\mu)$.With these ideas and notation established, we now extend this formalism to a multi-layer model.

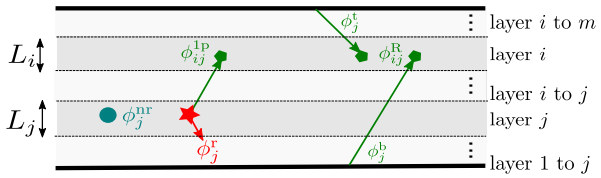

Figure 6.3.1: Reabsorption and recombination events in a multi-layer cell.

6.3 Multi-layer Detailed Balance

As shown in Fig. 6.3.1, we consider a device with m vertically stacked layers, series connected to each other. We continue to assume infinite carrier mobility and allow each layer to have a different quasi-Fermi level splitting, μ_i. Each layer has thickness L_i, absorption coefficient $\alpha_i(E)$ and refractive index $n_i(E)$, assumed to be constant within a layer. The total device thickness is $L = \sum L_i$. In most III-V devices, refractive index does not vary significantly between layers, so in this work we do not include reflection or refraction between layers.

The detailed balance condition is satisfied in every layer:

$$J_i = J_i^{\mathrm{in}} - J_i^{\mathrm{loss}} \tag{6.3.1}$$

where J_i is the extracted current density from layer i, J_i^{in} is the rate of absorption of incident photons per area in layer i and J_i^{loss} is the net loss of current density due to recombinations in layer i. J_i^{loss} includes LC as a negative loss.

We start with J_i^{in}. The incident photon flux in each layer is calculated similarly to the single layer case:

$$J_i^{\mathrm{in}} = \int \mathrm{d}\Omega \int_0^\infty \mathrm{d}E \left[\phi_{\mathrm{in}}^{\mathrm{t}} t_{ti} + \phi_{\mathrm{in}}^{\mathrm{b}} t_{\mathrm{b}i}\right] a_i \tag{6.3.2}$$

where we define the absorbance of each layer:

$$a_i(E,\theta) = 1 - e^{-\frac{\alpha_i(E) L_i}{\cos\theta}} \tag{6.3.3}$$

and the transmittance through all layers between but not including i and j as:

$$t_{ij}(\theta, E) = e^{-\frac{\sum_{k=i+1}^{j-1} \alpha_k(E) L_k}{\cos\theta}} \tag{6.3.4}$$

for $i > j+1$, and $t_{ji} = t_{ij}$. Note that for $|i-j| \leq 1$, $t_{ij} = 1$. For convenience, we define t_{ti} as transmittance through all layers above layer i, $t_{\mathrm{b}i}$ as transmittance through all layers below i, and t_{tb} as the transmittance through the whole stack. In Eq. 6.3.2, $\phi_{\mathrm{in}}^{\mathrm{t}}$ and $\phi_{\mathrm{in}}^{\mathrm{b}}$ are calculated using Table 6.1, with the same source terms as in Eq. 6.2.15, where we replace t with t_{tb}.

We now calculate J_i^{loss} in Eq. 6.3.1. J_i^{loss} includes three terms: (1) radiative loss, $\phi_i^{\text{r}}(\theta, E, \mu_i)$, (2) nonradiative loss, $\phi_i^{\text{nr}}(\theta, E, \mu_i)$, (3) luminescent coupling (LC) from layer j to layer i, $\phi_{ij}^{\text{lc}}(\theta, E, \mu_j)$. Similarly to the single-layer case in Eq. 6.2.25, we express J_i^{loss} using a geometry tensor:

$$J_i^{\text{loss}} = \int \mathrm{d}\Omega \int_0^\infty \mathrm{d}E \sum_{j=1}^{m} g_{ij}(\theta, E)\, S_j^{\text{r}}(E, \mu_j) \tag{6.3.5}$$

where $S_j^{\text{r}}(E, \mu_j)$ is given by Eq. 6.2.18 with the layer-specific $\alpha_i(E)$, $n_i(E)$, and μ_i. In PPC's, all α_i and n_i are the same in every layer, but we include the possibility of varying α and n to to include the case of solar cells, in which each layer can have different material properties.

We proceed to calculate the geometry tensor. Similarly to the single layer model,

$$g_{ij}(E, \theta) = 2\delta_{ij} g_{ij}^{\text{r}}(E, \theta) + 2\delta_{ij} g_{ij}^{\text{nr}}(E, \theta) - g_{ij}^{\text{lc}}(E, \theta) \tag{6.3.6}$$

where δ_{ij} is the Kronecker delta. Analogous to Equations (6.2.21) and (6.2.22), the radiative and nonradiative geometry factors in each layer are:

$$g_i^{\text{r}}(E, \theta) = \frac{\cos\theta}{\alpha_i(E)} a_i(E, \theta) \tag{6.3.7}$$

$$g_i^{\text{nr}}(E, \theta) = \left(\frac{1}{\eta_{\text{int}}^i} - 1\right) L_i \tag{6.3.8}$$

We divide the LC term, $g^{\text{lc}}(\theta, E)$, into one-pass and after-reflection contributions:

$$g_{ij}^{\text{lc}} = g_{ij}^{\text{1p}} + g_{ij}^{\text{R}}. \tag{6.3.9}$$

Without reflection, the geometry factor is

$$g_{ij}^{\text{1p}} = (1 - \delta_{ij})\, a_i t_{ij} g_j^r, \tag{6.3.10}$$

where we use $(1 - \delta_{ij})$ because one-pass reabsorption within the same layer is already included in g_i^r. We obtain $\phi_{ij}^{\text{R}} = g_{ij}^R S_j^r$ from the self-consistent reflected fluxes at the top and bottom surfaces from Table 6.1. For radiative events occurring in layer j, we take the source terms to be:

$$\phi_0^{\text{bdy}} = g_j^{\text{r}} S_j^{\text{r}} t_{j\text{bdy}} R^{\text{bdy}}, \tag{6.3.11}$$

where bdy is t or b, and find ϕ_j^{bdy} from Table 6.1. Then the absorption in layer i from radiative events in layer j is:

$$\phi_{ij}^{\text{R}} = a_i \left(\phi_j^{\text{t}} t_{\text{t}i} + \phi_j^{\text{b}} t_{\text{b}i}\right). \tag{6.3.12}$$

Using Equations (6.3.2) and (6.3.5) to (6.3.12), we obtain J_i in Eq. 6.3.1. When all layers are series connected, they share the same current density, $J_i = J$, which depends on the set of quasi-Fermi levels, μ_i. At one J value, we can solve for a set of μ_i values, the sum of which gives the voltage of the device. The efficiency is then written in terms of J:

$$\eta(J) = \frac{J \sum_i \mu_i(J)}{P_{\text{in}}} \tag{6.3.13}$$

Optimizing with respect to J gives the maximum efficiency.

6.4 Efficient Computation of $V(J)$

Finding $\eta(J)$ involves solving Eq. 6.3.1 with $J_i = J$, which is a system of m nonlinear equations in μ_i, and is computationally challenging. We can significantly reduce the computational cost by making simplifying assumptions on $\alpha(E)$ and the top and bottom reflectivities. First, we rewrite Eq. 6.3.1 using Eq. 6.3.5:

$$J_i = J_i^{\text{in}} - \int \mathrm{d}\Omega \int_0^\infty \mathrm{d}E \left[\sum_{j=1}^{m} g_{ij}(\theta, E)\, S_j^{\text{r}}(E, \mu_j) \right]. \tag{6.4.1}$$

We can simplify the calculation of $J(V)$ if (1) $\alpha_i(E)$ is zero for E less than the band gap E_{g}^i and a constant for $E > E_{\text{g}}^i$ and (2) top and bottom reflectivity are independent of E. In this case, $g_{ij}(\theta, E)$ becomes $g_{ij}(\theta)$ for all $E > E_g^i$, allowing the angular integral to be separated from the energy integral. Then we can rewrite Eq. 6.4.1 as:

$$J_i = J_i^{\text{in}} - \sum_{j=1}^{m} G_{ij} \mathcal{R}_j(\mu_j) \tag{6.4.2}$$

where

$$G_{ij} = \int \mathrm{d}\Omega g_{ij}(\theta) \tag{6.4.3}$$

$$\mathcal{R}_j(\mu_j) = \int_{E_{\text{g}}^j}^\infty \mathrm{d}E S_j^{\text{r}}(E, \mu_j). \tag{6.4.4}$$

Eq. 6.4.2 is a linear system of equations with unknowns $\mathcal{R}_j$. Thus for fixed J we can efficiently solve for $\mathcal{R}_j$. We then invert $\mathcal{R}_j$ to find μ_j, using Equations (6.2.18) and (6.4.4), which allows us to find the external bias $V = \sum_i \mu_i$. We thus calculate $V(J)$ instead of $J(V)$. Either way, the power output is JV, and the maximum power point can be found numerically.

Table 6.2: Fixed parameters for Section 6.5

Property	Value
Band gap E_g [23]	1.424 eV
Absorption Coefficient α [23]	1.151×10^6 /m
Input Intensity	8×10^4 W/m^2
Input Wavelength	830 nm (1.494 eV)
Input Linewidth	1 nm
Series Resistance	0

Table 6.3: Top and bottom reflectivity configurations considered in this section along with icons to identify each combination.

Bottom \ Top	Total internal reflection	Lambertian
Absorbing substrate	A	B
Specular mirror	C	D
Lambertian mirror	E	F

6.5 Application: Multilayer Monochromatic Conversion

In this section, we demonstrate the use of this model by considering a set of monochromatic devices inspired by the record-efficiency PPC device but with m vertically stacked layers, varied η_{int}, and top and bottom boundary conditions. The effects of input power density, wavelength, linewidth, external radiative efficiency, which is different from η_{int}, absorbance and band gap were previously studied in a single-layer model [19, 50]. Here we fix those parameters as in Table 6.2 to approximate the record-efficiency PPC [9]. We show that devices with an absorbing substrate can improve their efficiency by increasing the number of layers, even without series resistance. This effect does not exist with a back reflector, which shows no improvement with increased number of layers. In Section 6.6 we present a simple model to explain these effects.

6.5.1 Reflectivity Models

For these examples, we consider a set of simple reflectivity models to approximate different levels of light trapping. We only consider models that are angle-dependent but not E-dependent to reduce computational costs, as discussed in Section 6.4. The general model of Section 6.3 allows any reflectivity configuration with dependence on θ and E.

We consider two models for the internal reflectivity at the top interface. In the following discussion, the top surface is an interface between air ($n_{\text{air}} = 1$) and a material with index n. We consider perfect transmission of external light into the sample, but there must be total internal reflection of optical modes on the inside surface. In the "Total internal reflection" model, we consider specular reflection of all incident rays with $\theta > \theta_c$, so $R_S^t(\theta)$ is a step function that is zero for $\theta < \theta_c$, and one for all

larger angles. As usual, the critical angle is $\theta_c = \sin^{-1}(n_{air}/n)$. The second top surface we consider is an ideal Lambertian surface, which randomizes the angle of propagation for reflected and transmitted photons. An ideal Lambertian surface admits all incident photons into the cell from the exterior while reflecting internal photons with a probability of $1 - \frac{n_{air}^2}{n^2}$ [55].

At the bottom surface, we consider three surface models. In the case of an absorbing substrate, we consider all photons hitting the bottom surface to be lost, i.e., $R_S^b = 0$ for all angles. A specular mirror reflects all photons back into the cell at the same angle as incidence, i.e., $R_S^b = 1$ for all angles. A Lambertian mirror also reflects all photons back into the cell but at a random angle of reflection.

We consider all six combinations of these models for the top and bottom surface reflectivities, as listed in Table 6.3. We label the six scenarios from A to F and also include an icon for each scenario.

6.5.2 Intrinsic Efficiency Increase With Number of Layers

We first consider Configuration A in Table 6.3, which has no light trapping and best represents the device of Ref. [9]. We numerically optimize the layer thicknesses to maximize efficiency with η_{int} values of 1, 0.999, 0.9, 0.1, 0.001. These values of η_{int} represent material qualities ranging from the radiative limit to low quality. In the radiative limit ($\eta_{int} = 1$), the optimal thickness of the full device is infinity so the cell absorbs all incident photons. Since nonradiative loss scales as $\left(\frac{1}{\eta_{int}} - 1\right) L$, there is a trade-off between nonradiative recombination loss and transparency loss when $\eta_{int} < 1$, giving a finite optimal device thickness. Hence, we optimize layer thicknesses without a constraint on total thickness for all $\eta_{int} < 1$ cases, while in the case of $\eta_{int} = 1$, we constrain the total thickness to have a vertical one pass absorbance of $1 - e^{-\alpha L} = 1 - 10^{-14}$.

The key results are shown in Fig. 6.5.1, giving the optimized efficiencies and layer thicknesses for a range of η_{int} and m. As expected, efficiency decreases as η_{int} decreases. More surprisingly, for all η_{int} values, efficiency increases with the number of layers. In the radiative limit, efficiency increases by 3.4% abs. from 1 to 10 layers; at $\eta_{int} = 0.001$, efficiency increases by 1.3% abs. Efficiency is expected to improve in multi-layer devices with series resistance, as the devices increase voltage while decreasing current and its associated losses. In this case, however, we see an improvement of efficiency even without series resistance.

We show in Fig. 6.5.2 efficiency at optimal layer thicknesses for all 6 surface configurations in Table 6.3. Material quality is fixed at $\eta_{int} = 0.9$, which represents high-quality III-V materials. Among all configurations, case A has the lowest efficiency, because this configuration does not include any light trapping. Efficiency is highest in Case F with two ideal Lambertian surfaces. Only cases with absorbing substrate (A and B) show strong efficiency increase with increasing m.

A back reflector and light trapping are helpful for PPC efficiency. The record-efficiency device,

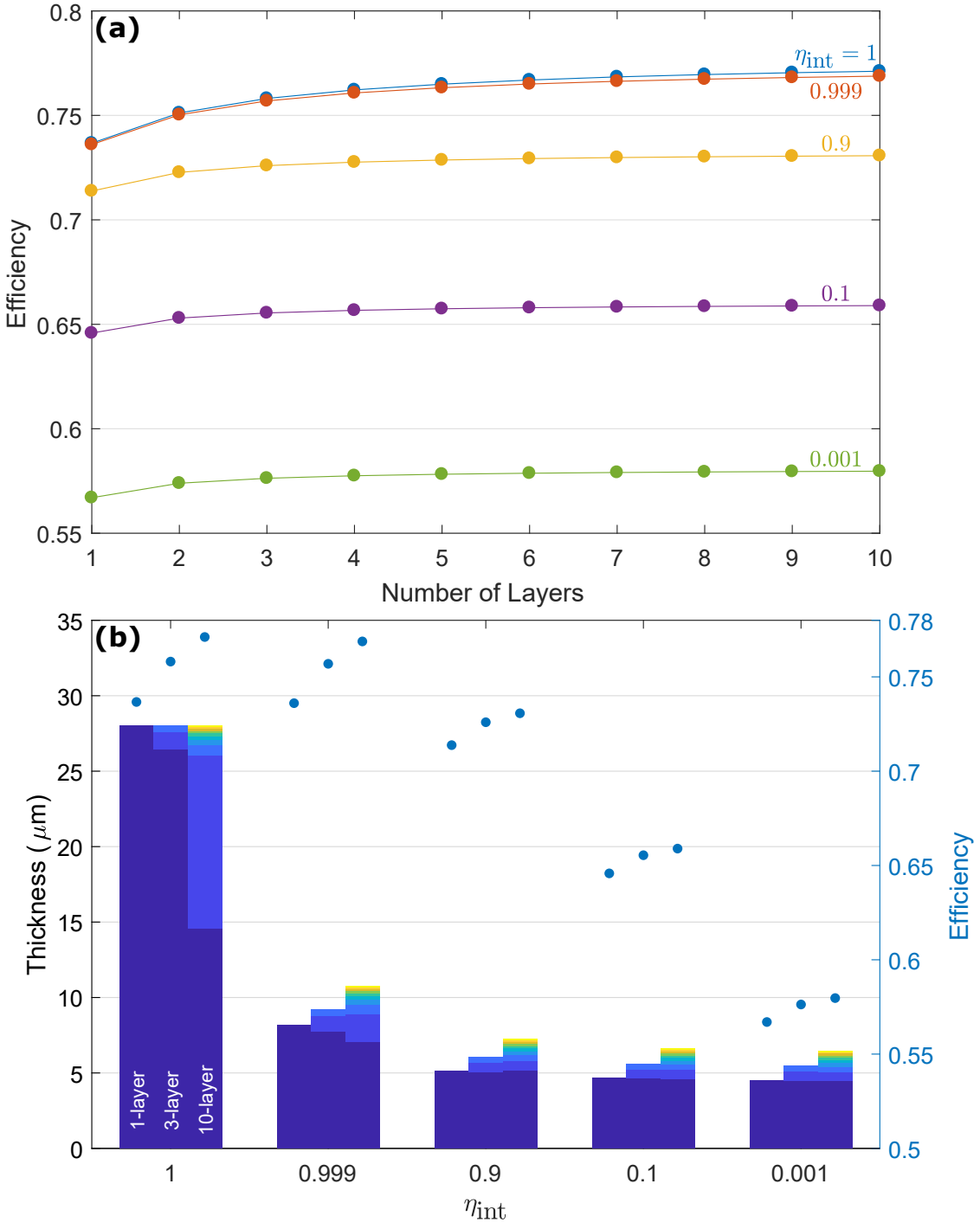

Figure 6.5.1: (a) Efficiency, optimized with respect to layer thicknesses, as a function of number of layers with Configuration A in Table 6.2 for several values of η_{int}. (b) Optimal layer thicknesses of 1-, 3- and 10-layer cells (left axis, bars) and the associated efficiencies (right axis, points).

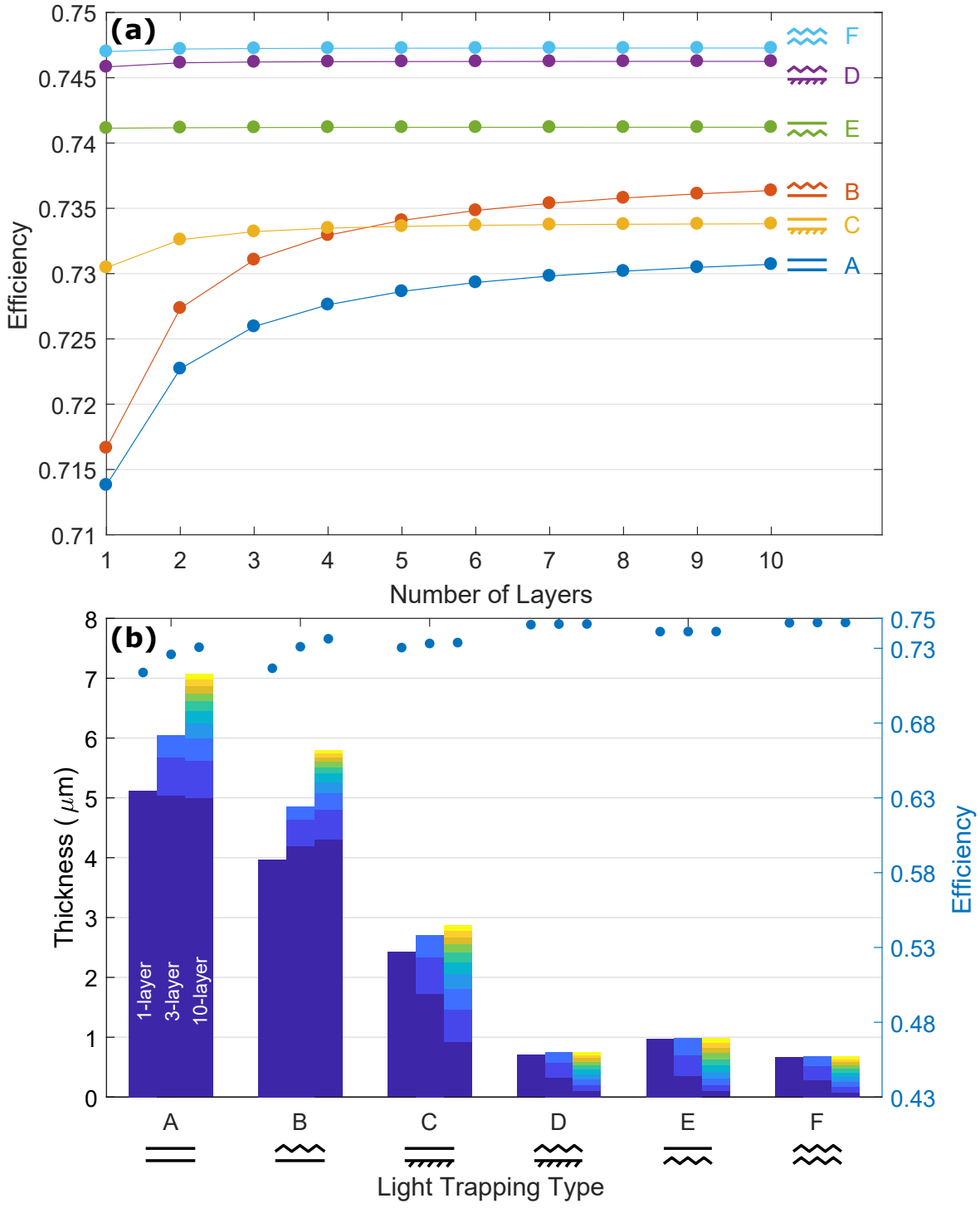

Figure 6.5.2: (a) Efficiency, optimized with respect to layer thicknesses, as a function of number of layers for all 6 surface configurations in Table 6.3. $\eta_{\text{int}} = 0.9$. Note that A, B have substrates and show the strongest intrinsic efficiency increase with m. (b) Optimal layer thicknesses of 1-, 3- and 10-layer stack.

however, is on a thick GaAs substrate with a full metal contact [9][56]. Since the GaAs substrate is absorbing and optically thick, this architecture is equivalent to an absorbing substrate without a back reflector. In such a system, this intrinsic increase of efficiency with m is an intriguing route to high efficiency, which reinforces the simpler series-resistance advantages of multi-layer devices. In order to understand the physical origin of this increased efficiency, we present a toy model of a 1- and 2-layer device, with and without a back reflector.

6.6 2-Layer Model

In this section, we reduce our full model from Section 6.3, to a semi-analytic 2-layer model. Using this simplified model, we demonstrate that the multi-layer device allows radiative losses into the substrate to be reduced, but that no equivalent improvement can be obtained when there is a back reflector. We consider Configurations B and F in Table 6.3. The simplest expectation for $m = 1$ devices is that the operating current is $J_{\rm mp}^{(1)} \simeq J^{\rm in}$, and we call the operating voltage $V_{\rm mp}^{(1)}$. With $m > 1$, one might expect that $J_{\rm mp}^{(m)} \simeq J_{\rm mp}^{(1)}/m$ and that each layer keeps the same voltage as in the one-layer device, giving a total voltage of $V_{\rm mp}^{(m)} \simeq mV_{\rm mp}^{(1)}$, which would give no change in the efficiency (in the absence of series resistance). For Configuration B in Fig. 6.5.2(a), however, we see a 1.5% (rel.) increase in efficiency on moving from $m = 1$ to $m = 2$. In these devices, $mJ_{\rm mp}^{(m)}$ changes by only 0.26%, so the more significant increase in efficiency comes from the operating voltage.

There is no analytic solution to $V_{\rm mp}^{(m)}$ and $J_{\rm mp}^{(m)}$. Hence, for qualitative understanding, we study the the short-circuit current $J_{\rm sc}^{(m)}$ and the open-circuit voltage $V_{\rm oc}^{(m)}$, as well as the product $J_{\rm sc}^{(m)}V_{\rm oc}^{(m)}$. We choose configurations with Lambertian surfaces in order to express the emission and absorption flux using the same angle-averaged absorbance. For the same reason, we assume that there is a filter between two layers that randomizes the the angle of the transmitted light. We work in the radiative limit and consider $n = 1$, so there is no reflection at cell-air or cell-substrate interfaces. We assume that absorption coefficient is 0 for energy lower than the band gap, and constant α for energy above the band gap. For simplicity, we work in the Boltzmann approximation, in which the "-1'' in the denominator of Eq. 6.2.18 is neglected, which is valid when the internal cell voltages do not get within a few kT of E_g. The detailed-balance condition, Eq. 6.4.1, for each layer is then

$$\begin{aligned} J_1 &= J^{\rm in}\left(1-A_2\right)A_1\left[1+R_{\rm L}^{\rm b}\left(1-A_1\right)\right] \\ &\quad - J_0 e^{V_1}\left(2A_1 - R_{\rm L}^{\rm b}A_1^2\right) + J_0 e^{V_2}A_2\left[A_1 + R_{\rm L}^{\rm b}\left(1-A_1\right)A_1\right] \end{aligned} \tag{6.6.1a}$$

$$\begin{aligned} J_2 &= J^{\rm in}A_2\left[1+R_{\rm L}^{\rm b}\left(1-A_2\right)\left(1-A_1\right)^2\right] \\ &\quad - J_0 e^{V_2}\left[2A_2 - R_{\rm L}^{\rm b}A_2^2\left(1-A_1\right)^2\right] + J_0 e^{V_1}\left(2A_1 - R_{\rm L}^{\rm b}A_1^2\right)A_2, \end{aligned} \tag{6.6.1b}$$

where A is the angle-averaged one-pass absorbance:

$$A = \frac{\int_0^{\pi/2} \left(1 - e^{-\frac{\alpha L}{\cos\theta}}\right) \cos\theta \sin\theta \mathrm{d}\theta}{\int_0^{\pi/2} \cos\theta \sin\theta \mathrm{d}\theta} \tag{6.6.2}$$

and J_0 is short-circuit radiative recombination current in one of the up or down direction:

$$J_0 = \frac{2\pi}{h^3 c^2} \int_{E_\mathrm{g}}^{\infty} \mathrm{d}E E^2 e^{-E/kT}. \tag{6.6.3}$$

The top layer absorbs the incident radiation, $A_2 J^{\mathrm{in}}$, in one-pass, and $R_\mathrm{L}^\mathrm{b} \left(1 - A_2\right) \left(1 - A_1\right)^2 A_2 J^{\mathrm{in}}$, in the second pass, where R_L^b is the back reflectivity. The top layer radiates both out the top surface and to the bottom layer ($J_0 e^{V_2} A_2$). The top layer has luminescent coupling from the bottom layer (proportional to $J_0 e^{V_1} A_1$) as well as photon recycling due to the back reflector. The bottom layer receives the filtered incident radiation $(1 - A_2) A_1 J^{\mathrm{in}}$ in one pass, $R_\mathrm{L}^\mathrm{b}(1 - A_2)(1 - A_1) A_1 J^{\mathrm{in}}$ in the second pass, luminescent coupling in two passes from the top layer (proportional to $J_0 e^{V_2} A_2$), and also has radiative emission to the top layer and the substrate. We can recover a 1-layer detailed balance model by setting either A_1 or A_2 to be zero. For simplicity of notation, we delete the subscript when referring to the 1-layer quantities. Using Eq. 6.6.1, we study the cases of $R_\mathrm{L}^\mathrm{b} = 0$, absorbing substrate, and $R_\mathrm{L}^\mathrm{b} = 1$, ideal back reflector.

Starting with a 1-layer device, we solve for V_oc and J_sc in Eq. 6.6.1 in each of the two cases:

$$\frac{V_\mathrm{oc}^{(1)}}{kT} = \begin{cases} \ln\tilde{J} + \ln\frac{1}{2} & \text{substrate} \\ \ln\tilde{J} & \text{back reflector} \end{cases} \tag{6.6.4}$$

$$\tilde{J}_\mathrm{sc}^{(1)} = \begin{cases} A\left(\tilde{J} - 2\right) & \text{substrate} \\ \left(2A - A^2\right)\left(\tilde{J} - 1\right) & \text{back reflector} \end{cases} \tag{6.6.5}$$

where $\tilde{J} = \frac{J^{\mathrm{in}}}{J_0}$ and $\tilde{J}_\mathrm{sc} = \frac{J_\mathrm{sc}}{J_0}$.

In 2-layer devices, the voltage of each layer at open circuit is:

$$\frac{V_{\mathrm{oc},1}^{(2)}}{kT} = \begin{cases} \ln\tilde{J} + \ln\frac{(2 - A_2)}{4 - A_1 A_2} & \text{substrate} \\ \ln\tilde{J} & \text{back reflector} \end{cases} \tag{6.6.6}$$

$$\frac{V_{\mathrm{oc},2}^{(2)}}{kT} = \begin{cases} \ln\tilde{J} + \ln\frac{(2 + A_1 - A_1 A_2)}{4 - A_1 A_2} & \text{substrate} \\ \ln\tilde{J} & \text{back reflector} \end{cases} \tag{6.6.7}$$

For a two-layer device at short-circuit: (1) $J_\mathrm{sc} = J_1 = J_2$, and (2) $V_1 + V_2 = 0$. Solving Eq. 6.6.1 with

these constraints, we obtain the short-circuit current. Due to the length of the general solution, here we present only the solution evaluated at $A_1 = 1$ and $A_2 = 1/2$, which we consider further below:

$$\tilde{J}_{\rm sc}^{(2)} = \begin{cases} \frac{\tilde{J}}{2} - \frac{7}{2\sqrt{15}} & \text{substrate} \\ \frac{\tilde{J}}{2} - \frac{1}{2} & \text{back reflector} \end{cases} \tag{6.6.8}$$

To understand the origin of the efficiency improvement with m, we compare the value of $V_{\rm oc}^{(m)}/m$ and $J_{\rm sc}^{(m)}m$, as well as the product of the two quantities. Since, $0 \leq A_i \leq 1$, with a substrate we always have $V_{\rm oc,1}^{(2)} \leq V_{\rm oc}^{(1)} \leq V_{\rm oc,2}^{(2)}$. The average $V_{\rm oc}^{(2)}$ with substrate can be larger or smaller than $V_{\rm oc}^{(1)}$, depending on the values of A_1 and A_2. We consider absorption-matched devices with infinite thickness for $m = 1, 2$. In this case, $A = 1$ for the 1-layer case, and $A_1 = 1$ and $A_2 = 1/2$ with 2 layers. Here, both the single- and 2-layer devices absorb all incident photons. In the case of an absorbing substrate, the per-layer $V_{\rm oc}$ of the 2-layer device is strictly larger than that of the 1-layer device. Specifically, for $\tilde{J} = 10$, the average 2-layer $V_{\rm oc}$ is 6.3% higher than the 1-layer $V_{\rm oc}$. At the same time, $mJ_{\rm sc}^{(m)}$ also increases by 2.4%. We thus see that the efficiency with $m = 2$ is larger than with $m = 1$, due to increases in both $J_{\rm sc}$ and $V_{\rm oc}$, though the $V_{\rm oc}$ increase is more significant. The product, $J_{\rm sc}^{(m)}V_{\rm oc}^{(m)}$, increases by 8.8%.

In the case of a substrate, the voltage difference between the top and bottom layers reduces radiative loss to the substrate. Radiative losses from the top surface are inevitable, as the device must be able to admit incident radiation. Radiative losses out the rear of the device, however, are pure losses. In a single-layer device, those losses are unavoidable at any voltage. The multi-layer device is able to reduce the impact of those losses by decreasing the internal voltage of the bottom layer, which reduces the radiation into the substrate, while allowing the upper layer to maintain a larger internal voltage. Reduced radiative loss out the bottom layer also increases the collected current $mJ_{\rm sc}$, but this effect is smaller.

Interestingly, at higher incident flux density, both $V_{\rm oc}$ and $J_{\rm sc}$ effects are weaker. The power density used in Section 6.5 corresponds to $\tilde{J} \approx 9 \times 10^{16}$. With this value, in the toy model $V_{\rm oc}^{(m)}/m$ increases by 0.26%, while $mJ_{\rm sc}^{(m)}$ stays the same within machine precision. In the full model of Section 6.3 with $n = 1$ and $\eta_{\rm int} = 1$, the improvement of maximum power on moving from $m = 1$ to $m = 2$ for Configuration B is 0.22%, in good agreement with the simpler model. With GaAs refractive index, $n = 3.64$, the improvement is 2.0%, similar to that shown in Fig. 6.5.2(a), showing that the increased top-surface light trapping increases the importance of this effect.

In contrast, for the case with a back reflector, the voltage of each layer in a 2-layer device is analytically equal to the voltage of the single-layer device in all A_1 and A_2 values. And $2J_{\rm sc}^{(2)}$, evaluated

at the absorption matched case of $A_1 = 1$ and $A_2 = 1/2$, is also analytically equal to $J_{sc}^{(1)}$ at $A = 1$. This matches our observation in the full model that efficiency does not increase with number of layers in Configuration F.

The highly nonradiative case, $\eta_{int} \ll 1$, is also amenable to analytic treatment and shows a similar increase of efficiency with m.

We have generalized monochromatic detailed balance models [19, 50] to multi-layer devices, including: (1) bi-directional luminescent coupling, (2) nonradiative recombination parametrized by η_{int}, (3) mixed specular and Lambertian surface reflection. We observe an intrinsic increase of efficiency with number of layers, independent of series resistance, for PPC's on absorbing substrates. This intrinsic increase is not present when the device has a back reflector. Other than the well-known benefits of multi-layer PPC's, such as high voltage and low series resistance, we have discovered another mechanism for efficiency increase with number of layers, which further encourages future multi-layer designs of PPCs.

Acknowledgement

We acknowledge helpful conversations with Matthew M. Wilkins. This work was supported by NSERC grant number STPGP 494090 and Ontario Early Researcher Award ER17-13-019.

Chapter 7

Detailed Balance Efficiency for Multi-Layer PPC at 1310 nm

Daixi Xia, Meghan N. Beattie, Man Chun Tam, Matthew M. Wilkins, Christopher E. Valdivia, Zbigniew R. Wasilewski, Karin Hinzer, and Jacob J. Krich

This article was presented at 46th IEEE Photovoltaic Specialists Conference, June 2019, Chicago, Illinois [57]. The original title is "Opportunities for High Efficiency Monochromatic Photovoltaic Power Conversion at 1310 nm". This chapter uses the multi-layer detailed balance model, discussed in Chapter 6, to predict the efficiency of multi-layer PPC's, which are under development and are designed to operate at 1310 nm. The efficiency of PPC's from 1 to 20 layers at two different internal radiative efficiencies (radiative limit, and conservative material quality estimate) is predicted.

7.1 Introduction

A power-over-fiber system is an energy transmission system in which power is transmitted in the form of laser light through an optical fiber. Such a system is immune to electromagnetic noise and can find many uses in telecommunication, utilities and powering electric circuits in sensitive environments [58]. A crucial part of this system is a photovoltaic device, a photonic power converter (PPC), that converts the narrow-band laser or LED light to electricity. Current high efficiency PPCs are made of GaAs and operate in the 830 nm band with efficiency up to 70% [9, 11]. However, the attenuation of 830 nm light in a silica fiber is 37% over 1 km [18], hence the current devices target applications only requiring short-distance transmission. Long distance transmission can be achieved in the telecommunication regime, where attenuation is much slower. For example, at 1310 nm, there is only a 6.7% loss over 1 km [18]. Hence a high-efficiency PPC operating in the telecommunication regime is needed.

We develop an $In_xAl_yGa_{(1-x-y)}As$ device to operate at 1310 nm. We propose a series-connected multijunction design to provide high-voltage and low-current operation, which reduces series resistance loss and can be designed to directly power electronics requiring 3, 5 or 12 V. Green showed that monochromatic light conversion can reach 100% efficiency at infinite input light intensity, when the input wavelength is aligned with the bandgap [19]. In this work, we use a multijunction extension of Green's theory to make predictions of efficiency and voltage of our future multijunction $In_xAl_yGa_{(1-x-y)}As$ device. Our model includes the effects of luminescent coupling (LC), where light emitted in one junction is re-absorbed in another [59]. We also include the important effects of non-radiative recombination losses and imperfect alignment of cell band gap and input wavelength, studied in Chapter 5, in addition to the radiative losses at finite light intensity studied by Green. The full model will be described elsewhere. Using this model, we report power conversion efficiency of our proposed multijunction InAlGaAs device in the radiative limit and with a low internal radiative efficiency. We perform our calculations at 1319 nm input, which is the center wavelength of our test laser.

7.2 InAlGaAs Test Structure

We present a single-junction device and a multi-junction design both using $In_xAl_yGa_{(1-x-y)}As$. We begin by describing the existing device. The quaternary alloy, $In_xAl_yGa_{(1-x-y)}As$, is a promising material for 1310 nm (0.95 eV) photovoltaic (PV) conversion, due to its composition-dependent bandgap in the range of 0.75-1.45 eV [60]. By varying the compositions of $In_{0.53}Ga_{0.47}As$ and $In_{0.52}Al_{0.48}As$, ternary alloys lattice-matched to InP, we are able to achieve a bandgap suitable for a 1310 nm laser source. We have grown a test device by molecular beam epitaxy with a single pn-junction $In_{0.532}Al_{0.097}Ga_{0.371}As$ on an InP substrate. A schematic of this structure is shown in Figure 7.2.1(a). We use spectroscopic ellipsometry with data fitted using the Adachi-New Forouhi model [22] to measure the bandgap and absorption coefficient of the test structure, giving a bandgap of 0.864 eV and an absorption coefficient of 8×10^3 cm^{-1} at the target wavelength.

Figure 7.2.2 shows the external quantum efficiency (EQE), adjusted by measured reflectivity R and estimated absorbance of the cap layer A_{cap}:

$$\text{QE}_{\text{adj}} = \frac{\text{EQE}}{(1-R)(1-A_{\text{cap}})} \tag{7.2.1}$$

The cap layer is 25 nm thick lattice matched InGaAs, and was not etched in this test device. In fully fabricated devices, the absorbing cap layer will be removed everywhere except beneath the contacts, removing this parasitic absorption. The active region of the test structure is 2.8 μm thick, and we estimate a transmittance of the active region of 11%. Including the effect of this transmittance, we

estimate an internal quantum efficiency of 92% at 1310 nm. The QE measurement indicates the device's promising potential for future PV operation.

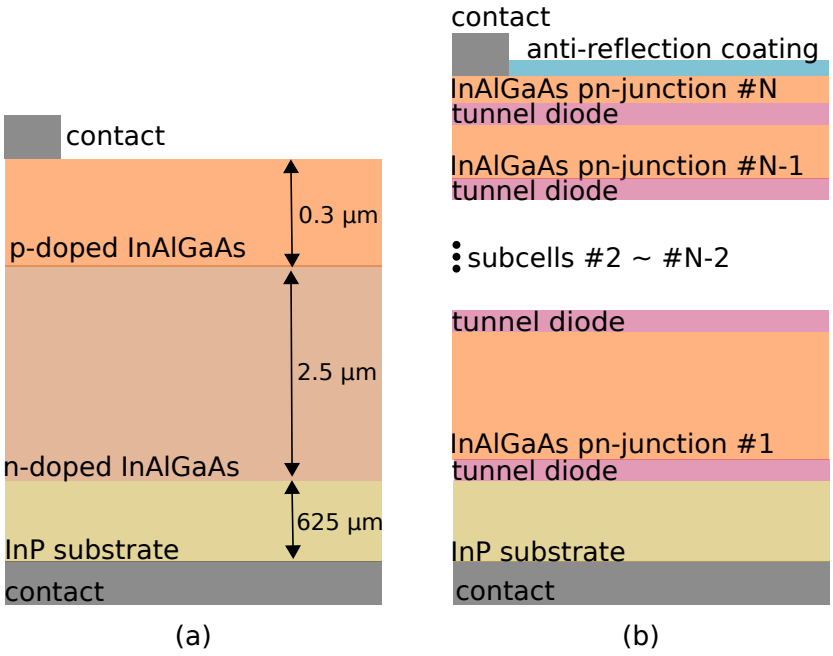

Figure 7.2.1: Schematics (not to scale) of the InAlGaAs single-junction (a) and multi-junction (b) devices.

Based on this newly developed system, we propose a multijunction structure consisting entirely of $In_{0.532}Al_{0.097}Ga_{0.371}As$ pn-junctions, series-connected by tunnel diodes, shown in Figure 7.2.1(b). To limit cell thickness, the cell is designed to absorb 98% of the incoming light, giving an active region of thickness 4.9 μm. Our test laser, a DILAS 1310 nm fiber-coupled module, outputs 14 W centered at 1319 nm with a linewidth of 8.9 nm. With a cell size of 25 mm^2, the average intensity is 5.6×10^5 W/m^2. We use these values for all the calculations. In the following sections, we use a multijunction detailed balance model to predict the maximum achievable efficiency of this proposed multijunction device operating with this laser.

7.3 Multijunction Detailed Balance Model

The detailed balance formalism allows for benchmarking a PV device, because it provides the limiting efficiency. We first briefly describe the multijunction model based on the detailed balance formalism. The full description of the model will be provided elsewhere. In the second part of this section, we use this model to predict the behaviour of the cell's efficiency and output voltage as a function of number of junctions.

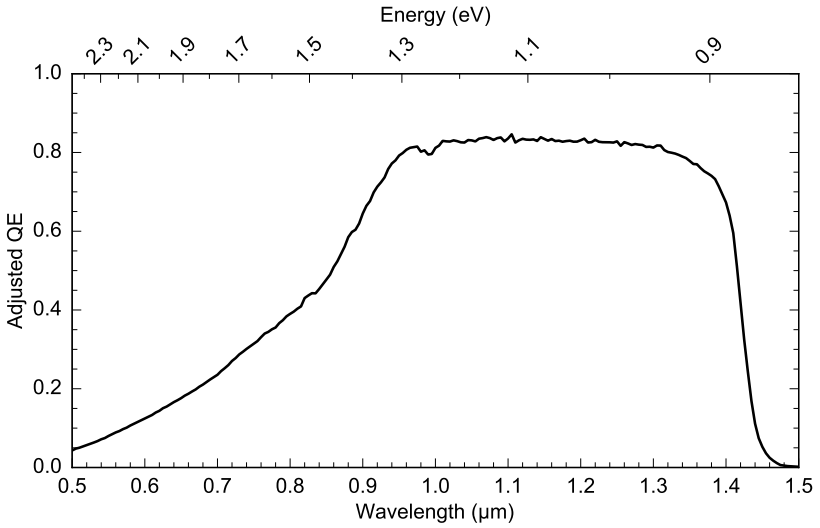

Figure 7.2.2: Adjusted quantum efficiency measurement of single-junction InAlGaAs test structure, as described in the text.

7.3.1 Laser spectrum and cell absorption

Knowledge of laser spectrum and cell absorption coefficient allows calculation of the number of photons absorbed in a device with a certain thickness. We have incorporated the laser spectrum into our detailed balance model. Our laser has a center wavelength of 1319 nm, corresponding to photon energy of 0.940 eV. Ellipsometry gave a bandgap of 0.864 eV. For convenience, we approximate the absorption coefficient to be a step function, with 0 below the bandgap and 8×10^3 cm^{-1} above, which is the measured value at 1310 nm. Thermalization loss from the laser photon energy, 0.940 eV, to the bandgap, 0.864 eV, is 8%. This loss is larger than the 5% thermalization loss of a GaAs-based 830 nm PPC [61] and can be possibly reduced with a different alloy.

7.3.2 A multijunction model based on ray tracing

We extend Green's formalism to a multijunction detailed balance model. In this model, we make the standard detailed balance assumptions that each photon absorbed creates one electron-hole pair and that carriers have infinite mobility so the quasi-fermi level splitting, μ, in each subcell is uniform in space. In the detailed balance formalism, the current extracted from each subcell is equal to the rate of photons absorbed minus the rate of photons emitted [29]. The rate of photons emitted depends on μ in each subcell, following the modified Planck spectrum [27]. Thus, for each junction, we can write down the following expression:

$$J_i = \dot{N}_i^{\mathrm{abs}} + \sum_j \dot{N}_{ij}^{\mathrm{lc}}\left(\mu_j\right) - \frac{1}{\eta_{\mathrm{int}}}\dot{N}_i^{\mathrm{rad}}\left(\mu_i\right) \tag{7.3.1}$$

where $\dot{N}_i^{\text{abs}}$ is the rate of carriers created in subcell i from absorbing photons from the external source, i.e., the laser, $\dot{N}_{ij}^{\text{lc}}(\mu_j)$ is the rate of carriers created in the ith subcell by absorbing photons that are emitted from the jth subcell, $\dot{N}_i^{\text{rad}}(\mu_i)$, is the rate of photons emitted at subcell i. We use η_{int}, internal radiative efficiency, to account for non-radiative recombination loss. $\dot{N}_{ij}^{\text{lc}}(\mu_j)$ captures the luminescent coupling. To compute the three terms in Eq. (7.3.1), we use a ray-tracing method to track photons emitted at an angle θ and energy E from a specific depth in the cell, as shown in Figure 7.3.1. This model is a 1-D model, but accounts for all angles of photon propagation. We then integrate the rates of photon absorption and emission over volume and photon energy to obtain the total rates of photon absorption and emission in each junction. Since they are all series-connected, all junctions share one current density, J. We assume perfect tunnel diodes, i.e., completely transparent and no series resistance. Eq. (7.3.1) is a system of coupled equations with unknown μ_i's. For some value of J, we can solve the system for the set of μ_i's, which in turn gives the internal voltages of each subcell, $V_i = \mu_i/q$, where q is the electric charge. The power conversion efficiency of the entire cell is then $\eta = J\sum V_i/P_s$, where P_s is the laser intensity. The total voltage is $\sum V_i$, and the maximum efficiency can be found by optimizing J. For simplicity, we modeled no reflection loss of incident photons in all directions of incidence, but the modeled laser light is collimated and normal incident. In future fabrications, an anti-reflection coating will be used to reduce reflection loss to a negligible amount [62]. In the next section, we present results on this current-optimized efficiency as well as the corresponding voltage.

7.4 Predicting Efficiency and Voltage for the Proposed Multi-junction Device

We predict efficiency possible at 5.6×10^5 W/m^2 with our proposed InAlGaAs multijunction structure with 1319 nm input. Figure 7.4.1 shows results in the radiative limit, i.e., $\eta_{\text{int}} = 1$, to study the maximum possible efficiency of the proposed device if all non-radiative processes are removed. It also shows predictions with a low value of $\eta_{\text{int}} = 0.1$, which is likely lower than the actual η_{int} of the material. This choice allows us to make a conservative estimate of the device performance. We predict that the proposed multijunction device attains an efficiency of 67% in the radiative limit with a single-junction design. In the conservative case of $\eta_{\text{int}} = 0.1$, the efficiency still reaches over 54% at single junction. In both cases, the detailed balance efficiency increases by 2% absolute when increasing the number of junctions from 1 to 20, reaching 69% in the radiative limit and 56% for $\eta_{\text{int}} = 0.1$. In the radiative limit, a 20-junction device is able to achieve a V_{mp} of 13.8 V. Even in the conservative case, V_{mp} still reaches 11.2 V at 20 junctions. Figure 7.4.1 shows that the multijunction devices not

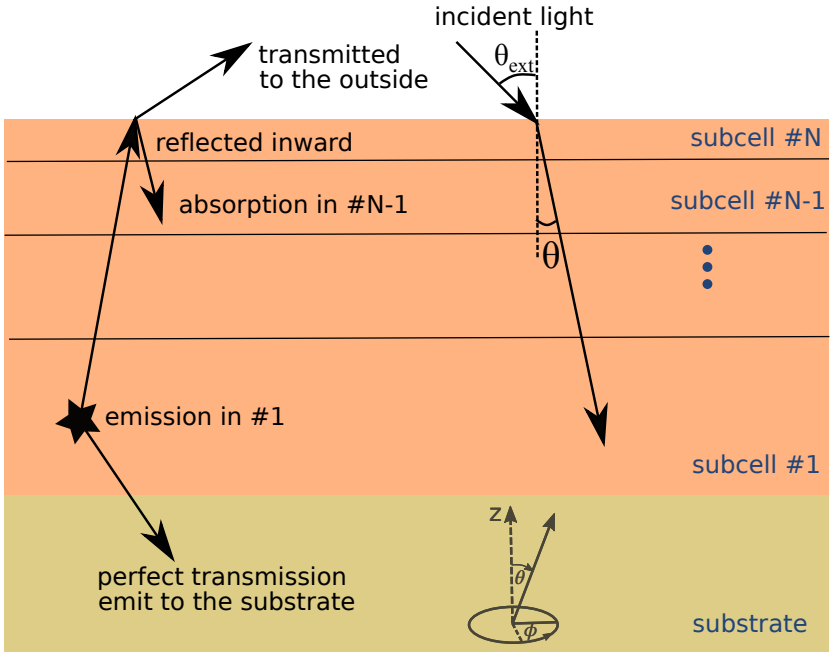

Figure 7.3.1: Diagram of ray tracing. Photons are emitted isotropically at each point in the cell at modified Planck spectrum rate. Photons reaching the cell-substrate interface all experience perfect transmission. Photons reaching the cell-air interface with an angle larger than the critical angle experience total internal reflection. The model assumes isotropy in the azimuthal angle. In our idealized reflectivity model, photons reaching the air-cell interface with an angle smaller than the critical angle experience perfect transmission. A more optimistic reflectivity model for photon recycling is a surface with internal reflectivity equal to 1 for all angles except for the acceptance cone of the external photons.

only give higher voltage but also give higher efficiency than single-junction equivalents, even when neglecting series resistance losses. All of the devices have the same total thickness, to absorb 98% of the incident light.

We analyze the internal voltage of each subcell calculated in a multijunction stack for devices with 1-4 subcells. Figure 7.4.2 shows the voltage of each subcell in a multijunction device with $\eta_{\text{int}} = 1$ and $\eta_{\text{int}} = 0.1$. The voltage of the bottom subcell (adjacent to the substrate) decreases as the total number of junctions increases, while subcells closer to the top have higher voltages. We can understand these results by considering reflectivity and luminescent coupling (LC). According to our reflectivity model described in Section 7.3, a portion of the photons reaching the top surface of the cell is reflected back into the cell and can be reabsorbed, while all photons reaching the bottom surface are lost into the substrate. Hence, if the voltages of the top and bottom subcells are equal, the bottom subcell loses more photons than the top subcell due to less photon recycling at the bottom surface. Under this asymmetric top and bottom surface reflectivity, in order to maintain current matching among the subcells, we require an internal variation of voltages. However, this effect of asymmetric top and bottom reflectivities alone does not explain the increase of efficiency with increasing number of subcells. The combination of LC, which is the reabsorption in one subcell of photons that are emitted in another

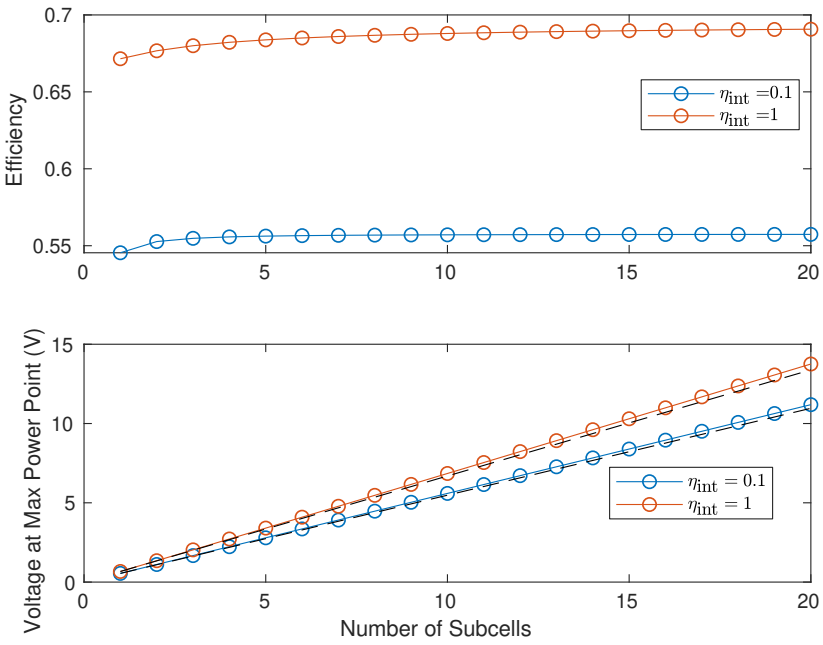

Figure 7.4.1: Detailed balance efficiency and corresponding V_{mp} as a function of number of junctions in the cell. Dashed lines show $V_1 N$, where V_1 is V_{mp} in a single junction device. The actual V_{mp} lines lie above these reference lines, indicating that the average voltage per subcell increases with number of subcells.

subcell, and the effect of the asymmetric top and bottom surfaces, gives a complete explanation. The LC leads to a new optimal current-voltage combination, which occurs when only the bottom subcell has lower than single-junction voltage and all other subcells obtain a higher than single-junction voltage. This new optimum reduces loss into the substrate when the number of total subcells increases. The resulting average voltage increases with the total number of subcells. This effect is shown in both Figures 7.4.1 and 7.4.2.

7.5 Conclusion

We show increasing efficiency as the number of subcells increases in monochromatic PV conversion. This effect is in addition to the well-known benefits of multijunction devices: high voltage and low series-resistance loss. This effect is independent of the operating wavelength of the device. The power conversion efficiency in the radiative limit does depend on the wavelength, and we report a modeled efficiency up to 69% at the center wavelength of our laser, 1319 nm, and at 5.6×10^5 W/m^2 in a 20-junction InAlGaAs device without a back reflector.

Acknowledgments

This work was supported by grant NSERC STPGP 494090.

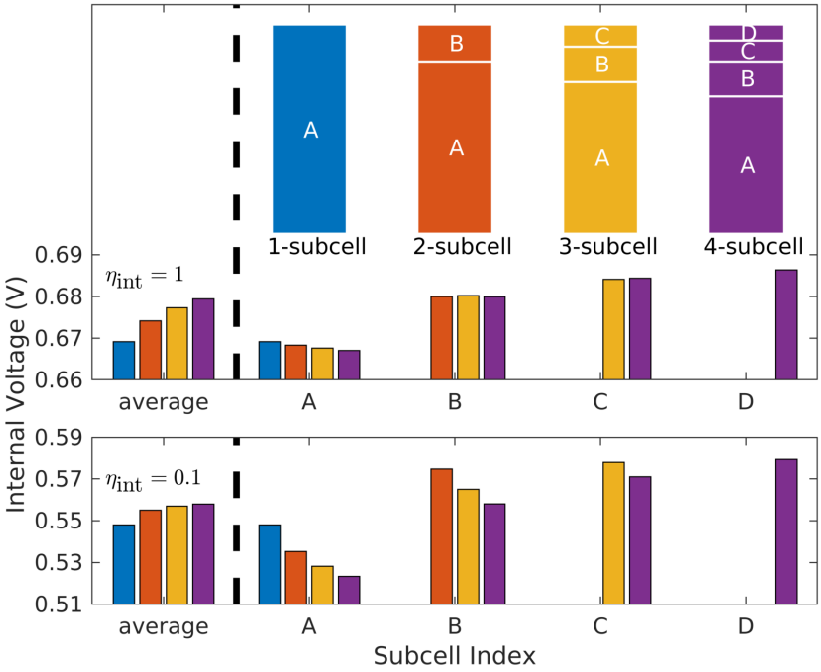

Figure 7.4.2: Internal voltages at maximum power point of 1-, 2-, 3- and 4-subcell devices. (top) Internal voltages with $\eta_{\text{int}} = 1$. Inset at top shows schematics of the three devices, with subcells labelled A to D. As indicated in the schematics, all four devices have the same total thickness, with white lines showing actual sizes of the various subcells. (bottom) Internal voltages with $\eta_{\text{int}} = 0.1$. In both panels, the average of the subcells' internal voltages is shown at left, indicating that the average voltage per subcell increases with the number of subcells.

Bibliography

[1] M. Roeger, G. Böttger, M. Dreschmann, C. Klamouris, M. Huebner, A. Bett, J. Becker, W. Freude, and J. Leuthold, "Optically powered fiber networks," *Optics express*, vol. 16, pp. 21 821–34, Jan. 2009.

[2] M. M. Wilkins, M. Ishigaki, P. Provost, D. Masson, S. Fafard, C. E. Valdivia, E. M. Dede, and K. Hinzer, "Ripple-Free Boost-Mode Power Supply Using Photonic Power Conversion," *IEEE Transactions on Power Electronics*, vol. 34, no. 2, pp. 1054–1064, Feb. 2019.

[3] A. Basanskaya, "Electricity over glass [fiber optic to transfer electric power]," *IEEE Spectrum*, vol. 42, no. 10, pp. 18–, Oct. 2005.

[4] A. Andersson, D. Destefan, J. D. Ramboz, S. Weiss, and J. M. DeHaan, "Unique EHV current probe for calibration and monitoring," in *2001 IEEE/PES Transmission and Distribution Conference and Exposition. Developing New Perspectives (Cat. No.01CH37294)*, vol. 1, Nov. 2001, pp. 379–384 vol.1.

[5] F. V. B. d. Nazaré and M. M. Werneck, "Development of a monitoring system to improve ampacity in 138kv transmission lines using photonic technology," in *IEEE PES T D 2010*, Apr. 2010, pp. 1–6.

[6] K. Murakawa, M. Kobayashi, O. Nakamura, and S. Kawata, "A wireless near-infrared energy system for medical implants," *IEEE Engineering in Medicine and Biology Magazine*, vol. 18, no. 6, pp. 70–72, Nov. 1999.

[7] C. Algora and R. Peña, "Recharging the battery of implantable biomedical devices by light," *Artificial Organs*, vol. 33, no. 10, pp. 855–860, Oct. 2009.

[8] A. Datas and P. Linares, "Monolithic interconnected modules (MIM) for high irradiance photovoltaic energy conversion: A comprehensive review," *Renewable and Sustainable Energy Reviews*, vol. 73, pp. 477–495, Jun. 2017. [Online]. Available: https://linkinghub.elsevier.com/retrieve/pii/S1364032117300734

[9] S. Fafard, M. C. A. York, F. Proulx, C. E. Valdivia, M. M. Wilkins, R. Arès, V. Aimez, K. Hinzer, and D. P. Masson, "Ultrahigh efficiencies in vertical epitaxial heterostructure architectures," *Applied Physics Letters*, vol. 108, no. 7, p. 071101, Feb. 2016. [Online]. Available: http://aip.scitation.org/doi/10.1063/1.4941240

[10] J. Schubert, E. Oliva, F. Dimroth, W. Guter, R. Loeckenhoff, and A. W. Bett, "High-Voltage GaAs Photovoltaic Laser Power Converters," *IEEE Transactions on Electron Devices*, vol. 56, no. 2, pp. 170–175, Feb. 2009.

[11] A. L. Fahrenbruch, L. Lopez-Otero, J. G. Werthern, and Ta-Chung Wu, "GaAs- and InAlGaAs-based concentrator-type cells for conversion of power transmitted by optical fibers," in *Conference Record of the Twenty Fifth IEEE Photovoltaic Specialists Conference - 1996*, May 1996, pp. 117–120.

[12] S. Fafard, F. Proulx, M. C. A. York, L. S. Richard, P. O. Provost, R. Arès, V. Aimez, and D. P. Masson, "High-photovoltage GaAs vertical epitaxial monolithic heterostructures with 20 thin p/n junctions and a conversion efficiency of 60%," *Applied Physics Letters*, vol. 109, no. 13, p. 131107, Sep. 2016. [Online]. Available: http://aip.scitation.org/doi/10.1063/1.4964120

[13] V. P. Khvostikov, N. A. Kalyuzhnyy, S. A. Mintairov, S. V. Sorokina, N. S. Potapovich, V. M. Emelyanov, N. K. Timoshina, and V. M. Andreev, "Photovoltaic laser-power converter based on AlGaAs/GaAs heterostructures," *Semiconductors*, vol. 50, no. 9, pp. 1220–1224, Sep. 2016. [Online]. Available: http://link.springer.com/10.1134/S1063782616090128

[14] V. P. Khvostikov, S. V. Sorokina, O. A. Khvostikova, R. V. Levin, B. V. Pushnyi, N. K. Timoshina, and V. M. Andreev, "GaSb laser-power (= 1550 nm) converters: Fabrication method and characteristics," *Semiconductors*, vol. 50, no. 10, pp. 1338–1343, Oct. 2016. [Online]. Available: http://link.springer.com/10.1134/S1063782616100146

[15] V. P. Khvostikov, P. V. Pokrovskii, O. A. Khvostikova, A. N. Pan'chak, and V. M. Andreev, "High-Efficiency AlGaAs/GaAs Photovoltaic Converters with Edge Input of Laser Light," *Technical Physics Letters*, vol. 44, no. 9, pp. 776–778, Sep. 2018. [Online]. Available: http://link.springer.com/10.1134/S1063785018090079

[16] N. Kalyuzhnyy, S. Mintairov, A. Nadtochiy, V. Nevedomskiy, D. Rybalchenko, and M. Shvarts, "InGaAs metamorphic laser (1064 nm) power converters with over 40% efficiency," *Electronics Letters*, vol. 53, no. 3, pp. 173–175, Feb. 2017. [Online]. Available: https://digital-library.theiet.org/content/journals/10.1049/el.2016.4308

[17] N. Singh, C. Kin Fai Ho, Y. Nelvin Leong, K. E. K. Lee, and H. Wang, "InAlGaAs/InP-Based Laser Photovoltaic Converter at ∼ 1070 nm," *IEEE Electron Device Letters*, vol. 37, no. 9, pp. 1154–1157, Sep. 2016. [Online]. Available: http://ieeexplore.ieee.org/document/7511682/

[18] B. E. A. Saleh and M. C. Teich, *Fundamentals of photonics*, 2nd ed. Hoboken, N.J: Wiley Interscience, 2007.

[19] M. A. Green, "Limiting photovoltaic monochromatic light conversion efficiency," *Progress in Photovoltaics: Research and Applications*, vol. 9, no. 4, pp. 257–261, 2001.

[20] J. Nelson, *The physics of solar cells.* London : River Edge, NJ: Imperial College Press ; Distributed by World Scientific Pub. Co, 2003, oCLC: ocm52689712.

[21] D. J. Griffiths, *Introduction to electrodynamics*, fourth edition ed. Boston: Pearson, 2013.

[22] J. W. Ryu, "Dependence of Optical Anisotropy of ZnO Thin Filmson the Structural Properties," *Journal of the Korean Physical Society*, vol. 57, no. 2(1), pp. 389–394, Aug. 2010.

[23] S. Adachi, *Optical constants of crystalline and amorphous semiconductors: numerical data and graphical information.* Boston: Kluwer Academic Publishers, 1999.

[24] H. Folliot, M. Lynch, A. L. Bradley, L. A. Dunbar, J. Hegarty, J. F. Donegan, L. P. Barry, J. S. Roberts, and G. Hill, "Two-photon absorption photocurrent enhancement in bulk AlGaAs semiconductor microcavities," *Applied Physics Letters*, vol. 80, no. 8, pp. 1328–1330, Feb. 2002, publisher: American Institute of Physics. [Online]. Available: http://aip.scitation.org/doi/10.1063/1.1455694

[25] F. Kadlec, H. Němec, and P. Kužel, "Optical two-photon absorption in GaAs measured by optical-pump terahertz-probe spectroscopy," *Physical Review B*, vol. 70, no. 12, p. 125205, Sep. 2004, publisher: American Physical Society. [Online]. Available: https://link.aps.org/doi/10.1103/PhysRevB.70.125205

[26] S. Krishnamurthy, Z. G. Yu, L. P. Gonzalez, and S. Guha, "Temperature- and wavelength-dependent two-photon and free-carrier absorption in GaAs, InP, GaInAs, and InAsP," *Journal of Applied Physics*, vol. 109, no. 3, p. 033102, Feb. 2011, publisher: American Institute of Physics. [Online]. Available: https://aip.scitation.org/doi/abs/10.1063/1.3533775

[27] P. Wurfel, "The chemical potential of radiation," *Journal of Physics C: Solid State Physics*, vol. 15, no. 18, pp. 3967–3985, 1982.

[28] M. A. Steiner, J. F. Geisz, I. García, D. J. Friedman, A. Duda, and S. R. Kurtz, "Optical enhancement of the open-circuit voltage in high quality GaAs solar cells," *Journal of Applied Physics*, vol. 113, no. 12, p. 123109, Mar. 2013. [Online]. Available: http://aip.scitation.org/doi/10.1063/1.4798267

[29] W. Shockley and H. J. Queisser, "Detailed Balance Limit of Efficiency of p-n Junction Solar Cells," *Journal of Applied Physics*, vol. 32, no. 3, pp. 510–519, 1961.

[30] M. A. Green, *Third generation photovoltaics: advanced solar energy conversion.* Berlin: Springer, 2003.

[31] ——, "Radiative efficiency of state-of-the-art photovoltaic cells: Radiative efficiency of photovoltaic cells," *Progress in Photovoltaics: Research and Applications*, vol. 20, no. 4, pp. 472–476, 2012.

[32] C. Baur, M. Hermle, F. Dimroth, and A. W. Bett, "Effects of optical coupling in III-V multilayer systems," *Applied Physics Letters*, vol. 90, no. 19, p. 192109, May 2007. [Online]. Available: https://aip.scitation.org/doi/10.1063/1.2737927

[33] M. A. Steiner, J. F. Geisz, T. E. Moriarty, R. M. France, W. E. McMahon, J. M. Olson, S. R. Kurtz, and D. J. Friedman, "Measuring IV curves and subcell photocurrents in the presence of luminescent coupling," in *2012 IEEE 38th Photovoltaic Specialists Conference (PVSC) PART 2*, Jun. 2012, pp. 1–11.

[34] M. A. Steiner and J. F. Geisz, "Non-linear luminescent coupling in series-connected multijunction solar cells," *Applied Physics Letters*, vol. 100, no. 25, p. 251106, Jun. 2012. [Online]. Available: http://aip.scitation.org/doi/10.1063/1.4729827

[35] M. A. Steiner, S. R. Kurtz, J. F. Geisz, W. E. McMahon, and J. M. Olson, "Using Phase Effects to Understand Measurements of the Quantum Efficiency and Related Luminescent Coupling in a Multijunction Solar Cell," *IEEE Journal of Photovoltaics*, vol. 2, no. 4, pp. 424–433, Oct. 2012.

[36] D. J. Friedman, J. F. Geisz, and M. A. Steiner, "Effect of Luminescent Coupling on the Optimal Design of Multijunction Solar Cells," *IEEE Journal of Photovoltaics*, vol. 4, no. 3, pp. 986–990, May 2014. [Online]. Available: http://ieeexplore.ieee.org/document/6767034/

[37] N. L. A. Chan, T. Thomas, M. Führer, and N. J. Ekins-Daukes, "Practical Limits of Multijunction Solar Cell Performance Enhancement From Radiative Coupling Considering Realistic Spectral Conditions," *IEEE Journal of Photovoltaics*, vol. 4, no. 5, pp. 1306–1313, Sep. 2014.

[38] M. Wilkins, C. E. Valdivia, A. M. Gabr, D. Masson, S. Fafard, and K. Hinzer, "Luminescent coupling in planar opto-electronic devices," *Journal of Applied Physics*, vol. 118, no. 14, p. 143102, Oct. 2015.

[39] J. Nelson, J. Barnes, N. Ekins-Daukes, B. Kluftinger, E. Tsui, K. Barnham, C. T. Foxon, T. Cheng, and J. S. Roberts, "Observation of suppressed radiative recombination in single quantum well p-i-n photodiodes," *Journal of Applied Physics*, vol. 82, no. 12, pp. 6240–6246, Dec. 1997. [Online]. Available: https://aip.scitation.org/doi/10.1063/1.366510

[40] M. A. Steiner, J. F. Geisz, I. García, D. J. Friedman, A. Duda, W. J. Olavarria, M. Young, D. Kuciauskas, and S. R. Kurtz, "Effects of Internal Luminescence and Internal Optics on V_{oc} and J_{sc} of III–V Solar Cells," *IEEE Journal of Photovoltaics*, vol. 3, no. 4, pp. 1437–1442, Oct. 2013.

[41] J. F. Geisz, M. A. Steiner, I. García, R. M. France, W. E. McMahon, C. R. Osterwald, and D. J. Friedman, "Generalized Optoelectronic Model of Series-Connected Multijunction Solar Cells," *IEEE Journal of Photovoltaics*, vol. 5, no. 6, pp. 1827–1839, Nov. 2015.

[42] E. Yablonovitch, "Statistical ray optics," *Journal of the Optical Society of America*, vol. 72, no. 7, p. 899, Jul. 1982. [Online]. Available: https://www.osapublishing.org/abstract.cfm?URI=josa-72-7-899

[43] D. M. Callahan, J. N. Munday, and H. A. Atwater, "Solar Cell Light Trapping beyond the Ray Optic Limit," *Nano Letters*, vol. 12, no. 1, pp. 214–218, Jan. 2012. [Online]. Available: https://doi.org/10.1021/nl203351k

[44] P. Campbell and M. A. Green, "Light trapping properties of pyramidally textured surfaces," *Journal of Applied Physics*, vol. 62, no. 1, pp. 243–249, Jul. 1987. [Online]. Available: https://aip.scitation.org/doi/10.1063/1.339189

[45] J. Balenzategui and A. Martí, "Detailed modelling of photon recycling: application to GaAs solar cells," *Solar Energy Materials and Solar Cells*, vol. 90, no. 7-8, pp. 1068–1088, May 2006. [Online]. Available: http://linkinghub.elsevier.com/retrieve/pii/S092702480500200X

[46] M. A. Green, "Lambertian light trapping in textured solar cells and light-emitting diodes: analytical solutions," *Progress in Photovoltaics: Research and Applications*, vol. 10, no. 4, pp. 235–241, 2002. [Online]. Available: https://onlinelibrary.wiley.com/doi/abs/10.1002/pip.404

[47] J. Eisenlohr, N. Tucher, O. Höhn, H. Hauser, M. Peters, P. Kiefel, J. C. Goldschmidt, and B. Bläsi, "Matrix formalism for light propagation and absorption in thick textured

optical sheets," *Optics Express*, vol. 23, no. 11, p. A502, Jun. 2015. [Online]. Available: https://www.osapublishing.org/abstract.cfm?URI=oe-23-11-A502

[48] T. Saga, "Advances in crystalline silicon solar cell technology for industrial mass production," *NPG Asia Materials*, vol. 2, no. 3, pp. 96–102, Jul. 2010. [Online]. Available: https://www.nature.com/articles/am201082

[49] B. M. Kayes, H. Nie, R. Twist, S. G. Spruytte, F. Reinhardt, I. C. Kizilyalli, and G. S. Higashi, "27.6% Conversion efficiency, a new record for single-junction solar cells under 1 sun illumination," *2011 37th IEEE Photovoltaic Specialists Conference*, pp. 000 004–000 008, 2011.

[50] D. Xia, M. M. Wilkins, S. S. Chahal, C. E. Valdivia, K. Hinzer, and J. J. Krich, "Opportunities for Increased Efficiency in Monochromatic Photovoltaic Light Conversion," in *2018 IEEE 7th World Conference on Photovoltaic Energy Conversion (WCPEC) (A Joint Conference of 45th IEEE PVSC, 28th PVSEC 34th EU PVSEC)*, Jun. 2018, pp. 3688–3692.

[51] P. Sharma, A. W. Walker, J. F. Wheeldon, K. Hinzer, and H. Schriemer, "Enhanced Efficiencies for High-Concentration, Multijunction PV Systems by Optimizing Grid Spacing under Nonuniform Illumination," *International Journal of Photoenergy*, vol. 2014, 2014, Art. ID 582083.

[52] C. E. Valdivia, M. M. Wilkins, S. S. Chahal, F. Proulx, P.-O. Provost, D. P. Masson, S. Fafard, and K. Hinzer, "Many-junction photovoltaic device performance under non-uniform high-concentration illumination," *AIP Conference Proceedings*, vol. 1881, p. 070005, Sep. 2017.

[53] S. Chahal, M. M. Wilkins, D. P. Masson, S. Fafard, C. E. Valdivia, and K. Hinzer, "20-junction photonic power converter performance under non-uniform illumination calculated by 3d distributed circuit model (Conference Presentation)," in *Physics, Simulation, and Photonic Engineering of Photovoltaic Devices VI*, vol. 10099. International Society for Optics and Photonics, Apr. 2017, p. 1009908.

[54] A. W. Setiawan Putra, M. Tanizawa, and T. Maruyama, "Optical Wireless Power Transmission Using Si Photovoltaic Through Air, Water, and Skin," *IEEE Photonics Technology Letters*, vol. 31, no. 2, pp. 157–160, Jan. 2019. [Online]. Available: https://ieeexplore.ieee.org/document/8579163/

[55] R. Strandberg, "The jv-Characteristic of Intermediate Band Solar Cells With Overlapping Absorption Coefficients," *IEEE Transactions on Electron Devices*, vol. 64, no. 12, pp. 5027–5033, Dec. 2017.

[56] D. Masson, F. Proulx, and S. Fafard, "Pushing the limits of concentrated photovoltaic solar cell tunnel junctions in novel high-efficiency GaAs phototransducers based on a vertical epitaxial het-

erostructure architecture," *Progress in Photovoltaics: Research and Applications*, vol. 23, no. 12, pp. 1687–1696, 2015.

[57] D. Xia, M. N. Beattie, M. Chun Tam, M. M. Wilkins, C. E. Valdivia, Z. R. Wasilewski, K. Hinzer, and J. J. Krich, "Opportunities for High Efficiency Monochromatic Photovoltaic Power Conversion at 1310 nm," in *2019 IEEE 46th Photovoltaic Specialists Conference (PVSC)*, Jun. 2019, pp. 2303–2306.

[58] J. B. Rosolem, "Power-Over-Fiber Applications for Telecommunications and for Electric Utilities," *Optical Fiber and Wireless Communications*, Jun. 2017.

[59] M. Wilkins, "Multi-Junction Solar Cells and Photovoltaic Power Converters: High-Efficiency Designs and Effects of Luminescent Coupling," Thesis, Université d'Ottawa / University of Ottawa, 2017.

[60] Y. S. Yong, H. Y. Wong, H. K. Yow, and M. Sorel, "A convenient band-gap interpolation technique and an improved band line-up model for InGaAlAs on InP," *Applied Physics B*, vol. 99, no. 3, pp. 477–486, May 2010.

[61] S. Fafard, M. C. A. York, F. Proulx, M. Wilkins, C. E. Valdivia, M. Bajcsy, D. Ban, R. Ares, V. Aimez, K. Hinzer, M. Ishigaki, and D. P. Masson, "Ultra-efficient N-junction photovoltaic cells with VOC $>$ 14v at high optical input powers," in *2016 IEEE 43rd Photovoltaic Specialists Conference (PVSC)*, Jun. 2016, pp. 2374–2378.

[62] D. M. Braun and R. L. Jungerman, "Broadband multilayer antireflection coating for semiconductor laser facets," *Optics Letters*, vol. 20, no. 10, pp. 1154–1156, May 1995.